

A NOVEL RESISTIVE PULSE SENSOR
FOR BIOLOGICAL MEASUREMENTS

Omar A. Saleh

A DISSERTATION
PRESENTED TO THE FACULTY
OF PRINCETON UNIVERSITY
IN CANDIDACY FOR THE DEGREE
OF DOCTOR OF PHILOSOPHY

RECOMMENDED FOR ACCEPTANCE
BY THE DEPARTMENT OF PHYSICS

January, 2003

© Copyright by Omar A. Saleh, 2002. All rights reserved.

Abstract

Resistive pulse analysis is an experimental technique that allows measurements of the sizes of solution-bound particles. It functions by measuring the electrical resistance of a pore that connects two solution-filled reservoirs: a particle entering the pore displaces conducting fluid, which leads to a transient change (or pulse) in the measured resistance. The magnitude and duration of the pulse are related to the size and position of the particle that caused it.

We have developed a novel platform for performing resistive pulse analysis on a microfabricated device containing a pore that is between 0.2 and 1 μm in diameter. We use the device to measure latex colloids with diameters between 100 and 600 nm, and to measure single macromolecules of DNA. We quantify the relation between the particle geometry and the pulse shape, and we find that particles traveling off of the pore axis significantly affect the measured pulses in a manner dependent on the force used to drive the particles through the pore (electrophoresis or fluid flow). We have developed a novel algorithm that increases the precision of measurements using fluid flow by removing these off-axis effects. This algorithm is not specific to our device, and should be useful for all future applications of the resistive pulse technique.

With this improved precision, we are able to measure nanometer-scale changes in the diameters of protein-coated colloids when they specifically bind to free protein in the solution— thus demonstrating the first successful strategy to add analyte specificity to a solid-state resistive pulse sensor. We find the measured diameter to be a useful probe of free protein concentration in the range 0.5 to 5 $\mu\text{g}/\text{mL}$; future versions of the device should make it sensitive to concentrations as low as 1 ng/mL . We also

demonstrate the applicability of this technique to performing common immunological assays, where small antigens in the solution are detected by the binding (or lack thereof) of antibody to the colloids.

Acknowledgments

Nothing in this thesis could have been accomplished but for a number of people who have offered me valuable advice, assistance, and friendship over the last few years. My thanks in this regard go to Olgica Bakajin, Nick Darnton, Geoff Facer, Larue Dunkleberger, Mingshaw Wu, Jim Knight, Jonas Tegenfeldt, and Christelle Prinze. Most of all, I must thank my advisor Lydia Sohn: her unflagging energy and dedication to the task at hand are standards I will strive to match for the rest of my professional life.

Finally, and most importantly, I am indebted to my wife Indi— without her strength and support, I'll never make it very far.

Contents

Abstract	iii
Acknowledgments	v
1 Introduction	1
2 Theoretical Considerations	6
2.1 The Increase in Electrical Resistance	6
2.1.1 Small Spheres	8
2.1.2 Large Spheres	10
2.1.3 Intermediate Sphere Sizes	11
2.1.4 Off-axis Spheres	13
2.2 The Particle Transit Time	14
2.2.1 The Drag Coefficients	16
2.2.2 On-axis Spheres	16
2.2.3 Off-axis Spheres	17
2.2.4 Electrophoresis vs. Hydrodynamic Drag	20
2.3 Summary	21
3 Experimental Protocols	23
3.1 Device Fabrication	23
3.1.1 Etched Quartz Devices	24
3.1.2 Molded PDMS Devices	27

3.2	Solution Preparation	30
3.2.1	Colloids	32
3.2.2	DNA solutions	33
3.3	Measurement	33
3.3.1	Inducing Particle Flow	33
3.3.2	Circuit Design	35
3.3.3	Data Acquisition	39
3.4	Summary	40
4	Quantitative Measurements of Polydisperse Colloidal Solutions	41
4.1	Introduction	41
4.2	Experimental details	41
4.3	Results	42
4.4	Discussion	44
4.5	Summary	47
5	Effects of Off-axis Particles	48
5.1	Introduction	48
5.2	Experimental details	48
5.3	Discussion	49
5.4	Summary	55
6	Immunological Sensing	58
6.1	Introduction	58
6.2	Experimental details	60
6.3	Data Analysis	64
6.3.1	Off-axis Effects	64
6.3.2	Calibrating the Pore	65
6.3.3	Extracting Colloid Diameters	66
6.4	Results	67

6.4.1	Simple Binding	67
6.4.2	Inhibition Assay	71
6.4.3	Sandwich Assay	71
6.5	Discussion	74
6.6	Summary	75
7	Sensing Single DNA Molecules	76
7.1	Introduction	76
7.2	Experimental details	77
7.3	Results	77
7.4	Discussion	79
7.5	Summary	84
8	Conclusion and Future Directions	85
8.1	Multi-analyte Detection	86
8.2	A Time-dependent Binding Probe	89
8.3	Summary	90
A	Recipes	91
A.1	Solutions	91
A.1.1	RCA SC1	91
A.1.2	Piranha Etch	92
A.1.3	Aqua Regia	93
A.2	Etched Quartz Devices	93
A.2.1	The Pore	94
A.2.2	The Reservoirs	96
A.2.3	The Electrodes	97
A.2.4	PDMS-coated Coverslips	98
A.2.5	Reusing Devices	99
A.3	Embedded PDMS Devices	99

A.3.1	The Master: Etched Pores	100
A.3.2	The Master: Pores Made of Resist	101
A.3.3	The Master: Reservoirs	103
A.3.4	Casting the Master	103
A.3.5	The Electrodes	104
A.3.6	Glass-PDMS bonding	105

Bibliography		111
---------------------	--	------------

Introduction

In this thesis, I describe the work we have undertaken in applying modern microfabrication and microfluidics technologies to resistive pulse analysis, which is a method for analyzing the size and concentration of particles dispersed in a solution. All devices used to perform this type of analysis consist of a measurement of the electrical resistance of an aperture (or pore) that connects two fluid-filled reservoirs; see Fig. 1.1. Particles in the solution pass from one reservoir to another through the aperture due to either an applied force (typically an electric field or a hydrodynamic drag) or simply by diffusion. When a particle inhabits the aperture, it displaces conducting fluid, and thus causes a transient increase, or pulse, in the aperture's electrical resistance. The magnitude of this resistance change is indicative of the size of the particle, and the frequency at which pulses occur is related to the particle concentration. The method of resistive pulse sensing was invented in 1953 by W. H. Coulter[1]. His 'Coulter Counter' contained an aperture typically tens of microns in diameter; it is still widely used to measure the size distributions of biological cells[2, 3].

Successful resistive pulse sensing requires the size of the analyzed particle to be of the same order as the size of the pore. Because of this constraint, inventing new methods to make smaller pores (and thus measure smaller particles) has been a major trend in the field. The first step in this direction was taken in the 1970s, when R. W. DeBlois and C. P. Bean invented the so-called 'Nanopar' device[4], a device consisting of a plastic sheet separating the reservoirs, and containing a single pore $0.5\text{-}3\ \mu\text{m}$ in

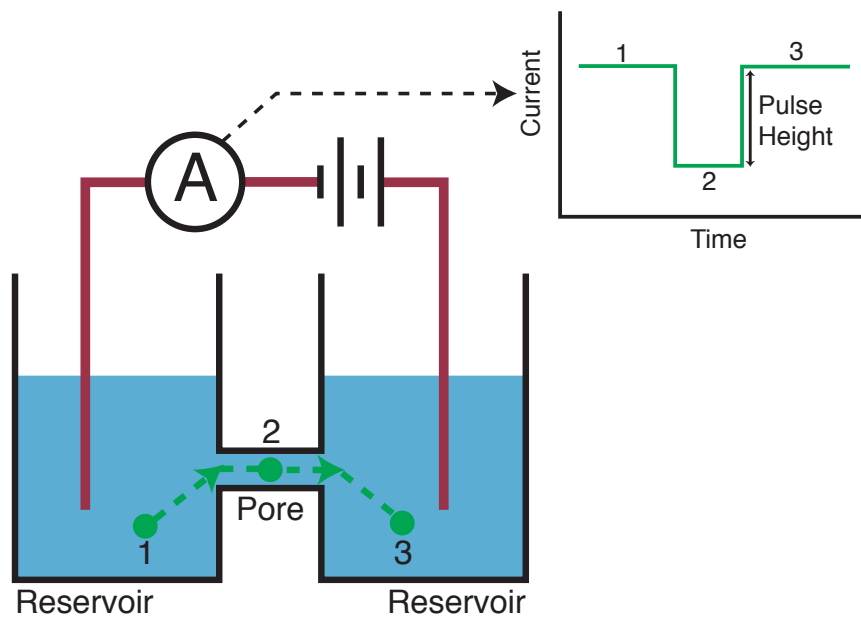


Figure 1.1: Schematic of the basic components of a resistive pulse sensor. A particle passing through the pore causes a pulse in the measured electrical current; the height of the pulse is proportional to the size of the particle.

diameter and several microns in length. The pores were realized using the ‘Nucleopore’ process, which involved irradiating the plastic sheet with high energy nuclear particles, then using a basic solution to etch pores along the damage tracks left by the particles. DeBlois and Bean further recognized that the homogenous electric field in a long, thin pore (as compared to the field in the relatively short and wide pore used by Coulter) allows greater analytical precision in relating resistive pulse height to particle size. They used their device to measure precisely colloidal particles with diameters ≥ 100 nm[4], analyze sperm cells[5] and characterize viral particles as small as 60 nm in diameter based on differences of both size and charge[6, 7, 8]. Later, von Schulthess and Benedek collaborated with DeBlois to use the Nanopar device to investigate the agglutination (crosslinking) of antigen-coated particles by antibody[9, 10, 11].

In 1994, the applicable length scale of resistive pulse sensing was drastically decreased when Bezrukov *et al.* successfully utilized an ion channel as a molecular Coulter counter[12, 13]. In their device, the reservoirs were separated by a lipid bilayer into which an ion channel, extracted from a cell wall, inserted itself. Measurements of the current through the nanometer-scale opening in the ion channel revealed the passage of single molecules contained in the solution. Perhaps the most important facet of this work was the introduction of analyte specificity to resistive pulse sensing. Previously, the resistive pulse method only revealed geometric attributes, such as size and shape, of the particles passing through the aperture. Ion channels, on the other hand, have functional chemical groups on their interiors, thus providing opportunities for chemical interaction between the particles and the pore. Such interactions are typically revealed by changes in the width of the resistive pulses. At the time of this writing, many groups are exploiting the capabilities of ion channels in an attempt to use them as biosensors that can be engineered to have sensitivities to many different molecules[13, 14, 15, 16, 17, 18].

Despite the success of several groups in utilizing ion channels as resistive pulse sensors of small molecules, the creation of a robust ion-channel-based device has been hampered by problems with the stability of the lipid bilayer. These concerns have led

several groups to work on new methods to fabricate stable ‘artificial’ pores (compared to the ‘natural’ protein ion channels) that are based in solid materials. To compare to the natural pores, the artificial pores must share at least one of their attributes: chemical functionality or nanometer-scale openings. To create chemically functional devices, groups have worked on using techniques of surface chemistry to covalently attach interacting molecules to the inside of a metal- or silica-based pore[19, 20]. Two strategies have recently been used to create nanometer-scale devices. Sun and Crooks used multiwalled carbon nanotubes as templates for pores in metallic films. They successfully created ~ 150 nm diameter devices and claimed that 10 nm diameter pores are attainable with their method[21]. More impressively, while using an ion beam to open a ~ 100 nm diameter hole in a thin silicon nitride membrane, Li et al. discovered a redeposition method that allowed creation of 1.8 nm diameter pores[22]. While apparently quite fragile, these pores were used to detect DNA molecules 500 base pairs in length.

Here, I describe the work we have undertaken in devising new technologies and strategies for resistive pulse sensing. We have invented a rapid and simple microfabrication process for creating stable pores of diameters 200 nm to 1 μm . Our process also permits a large amount of flexibility in design, and is thus ideally suited for future integration with other microfluidics technologies. In our studies, we have gained a complete understanding of the electrical and hydrodynamic effects of spherical particles in pores. Consequently, we have been able to implement a novel strategy for increasing the precision of resistive pulse measurements. This strategy is not specific to our device, and thus should be applicable to all future measurements using the resistive pulse technique. Using this increased precision, we demonstrate a novel method to add analyte specificity to the device through measurements of the diameter of protein-coated colloids. Finally, we show initial results indicating the sensitivity of our device to single molecules of DNA.

In Chapter 2, I review theoretical work on the electrical resistance of a fluid-filled pore containing an insulating sphere, and on the transit time of particles through a

pore. In Chapter 3, I describe the experimental protocols we use to fabricate and measure with our device. Chapter 4 focuses on applications of the device to simple polydisperse colloidal solutions. Chapter 5 describes the effects that off-axis particles have on our data, and a method to improve the resolution of the device by removing those effects. Chapter 6 describes our ability to add analyte sensitivity to the measurements, and the application of this technique to the detection of immunological binding reactions. In Chapter 7, I describe our efforts to detect single molecules of DNA. Finally, I conclude in Chapter 8 with a summary and suggestions for future research.

Theoretical Considerations

The majority of the experimental work we have accomplished has been on the passage of spherical latex colloidal particles through a long thin pore. Since the pores we use have uniform cross-sections with length, the resistance pulses resulting from the passage of colloids are fairly symmetric (square). Thus, the pulses can be well described by only two variables: their height, which depends on the electrostatic conditions, and their width, which reflects the particle transit time and thus the hydrodynamic conditions. In this chapter, I show that these two variables can be independently predicted with knowledge of the dimensions of the particle and pore, and the characteristics (conductivity, viscosity) of the fluid.

2.1 The Increase in Electrical Resistance

In our experiments, we use electrically insulating latex colloidal particles dispersed in a conductive electrolytic solution. Thus a colloid entering the pore will displace conducting fluid and increase the pore's electrical resistance. In this section, I quantify the relation between the diameter of the spherical colloid and the increase in electrical resistance of the pore. For reference, Fig. 2.1 defines the variables used throughout this chapter.

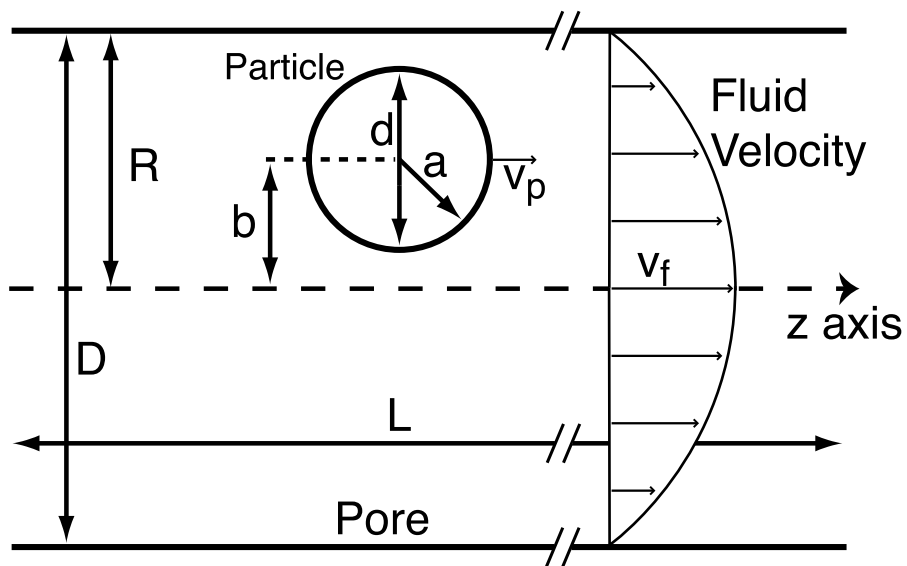


Figure 2.1: Definition of variables. A spherical particle of radius a , diameter d and velocity v_p is located a distance b off of the axis of a cylindrical pore of radius R , diameter D and length L . Far from the particle, the fluid has a parabolic velocity distribution with maximum v_f . The pore is centered on the z -axis.

2.1.1 Small Spheres

The first solution to the problem of the electrical resistance change caused by the presence of insulating spheres in a conducting fluid was proposed by Maxwell[23], and later repeated by Lord Rayleigh[24]. They considered the effective resistivity ρ_{eff} of an infinitely dilute solution of (many) insulating spheres dispersed in a fluid of resistivity ρ , and found that

$$\rho_{eff} = \rho(1 + 3f/2 + \dots), \quad (2.1)$$

where f is the fractional volume of solution occupied by the spheres. Eq. 2.1 is relevant to the problem of a single sphere occupying a pore in the dilute limit in which the sphere is much smaller than the pore diameter. The resistance of a cylindrical pore of diameter D and length L filled with fluid with a conductivity ρ is

$$R = 4\rho L/\pi D^2. \quad (2.2)$$

When the pore contains a sphere of radius $d \ll D$, the fractional volume occupied is

$$f = 2d^3/3D^2L. \quad (2.3)$$

Substituting Eqs. 2.3 and 2.1 into Eq. 2.2, we find the expected resistance R' of the pore when it contains a sphere of diameter d :

$$R' = (4\rho L/\pi D^2)(1 + d^3/D^2L + \dots). \quad (2.4)$$

It is quite useful to work with the relative increase in resistance $\Delta R/R = (R' - R)/R$, since this variable does not depend on the solution's conductivity. For the Maxwell formulation, $\Delta R/R$ is found to first order from Eqs. 2.2 and 2.4 to be

$$\Delta R/R = d^3/D^2L. \quad (2.5)$$

Eq. 2.5 applies only in the limit of an infinitely small sphere. Deblois and Bean[4] calculated a solution that is applicable to a wider range of sphere sizes, and that

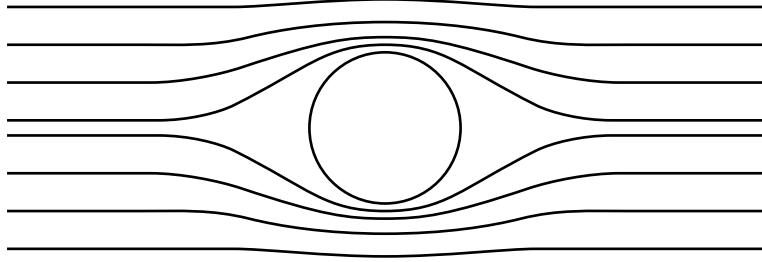


Figure 2.2: Qualitative sketch of the current streamlines around a sphere according to Eq. 2.6

agrees with the Maxwell solution in the small sphere limit. Consider an insulating sphere of diameter d placed at the origin in an infinite conducting fluid, with a constant electric field far from the sphere. The boundary condition at the sphere requires no electric field \vec{E} normal to the surface; in spherical coordinates (r, θ, ϕ) this is expressed as: $\vec{E}_r|_{d/2} = -\partial V/\partial r|_{d/2} = 0$, where V is the electric potential. The potential everywhere outside of the sphere is found by solving the Laplace equation subject to the two boundary conditions (at the sphere wall, and infinitely far from it):

$$V(r, \theta) = A(r + d^3/16r^2) \cos \theta, \quad (2.6)$$

where A is a constant determined by the strength of \vec{E} far from the sphere. The streamlines of electric current caused by this potential will be generally parallel to the \hat{z} direction, but will bulge out around the sphere, as sketched in Fig. 2.2.

Next, we must introduce the pore. The boundary condition at the pore wall will be the same as at the sphere surface: no normal fields are allowed. Thus, if the pore wall exactly parallels the current streamlines, *including* the bulge, Eq. 2.6 will be an exact solution of the potential. Deblois and Bean used Eq. 2.6 to find the exact resistance $R_{bulge,sphere}$ of a bulged pore when it contains a sphere. In order to find the change in resistance ΔR , they needed to find the resistance $R_{bulge,empty}$ of the empty

bulged pore. Deblois and Bean calculated that resistance through the relation

$$R = \int dR = \rho \int_{-L/2}^{L/2} \frac{dz}{A(z)}. \quad (2.7)$$

where $A(z)$ is the cross sectional area of the empty bulged pore.

In terms of the relative resistance change, their result for the increase in resistance upon addition of a sphere to a bulged pore is

$$\frac{\Delta R}{R} = \frac{d^3}{D^2 L} \left[\frac{D^2}{2L^2} + \frac{1}{\sqrt{1 + (D/L)^2}} \right] F\left(\frac{d^3}{D^3}\right), \quad (2.8)$$

where $F((d/D)^3)$ is a numerical correction factor, given as a table of values by Deblois and Bean; see Fig. 2.3 for a plot of Eq. 2.8. We found that those values are well fit by

$$F(x) = 1 + 1.264x + 1.347x^2 + 0.648x^3 + 4.167x^4. \quad (2.9)$$

Eq. 2.9 was used to find the value of F in all our comparisons with experiment.

Since the bulge decreases in magnitude with distance from the sphere, the bulged pore becomes more closely cylindrical when its diameter is much larger than the spheres; conversely, when the pore is close in size to the sphere, the bulge is quite large and the pore is not very cylindrical. Because the pore used in experiments is actually cylindrical, Deblois and Bean's calculation is valid only in the limit $d \ll D$ where the bulge is small.

Eq. 2.7 implicitly assumes that the current density is uniform across each cross section of the pore; any deviations from uniformity will cause the resistance to increase[23]. Because of this, Deblois and Bean's calculation of $R_{bulge,empty}$ represents a lower bound; therefore, their calculation of the resistance change $\Delta R = R_{bulge,sphere} - R_{bulge,empty}$ is an upper limit to the actual resistance change.

2.1.2 Large Spheres

When the sphere diameter approaches the pore diameter, Eq. 2.8 no longer applies. In 1965, Gregg and Steidley derived an expression[3] that was later shown to hold in

the limit of $d \lesssim D$. Their expression was found by considering Eq. 2.7, but assuming a cylindrical pore when substituting for $A(z)$. Thus, the resistance of the empty pore will simply be $4\rho L/\pi D^2$. For a pore containing a sphere, the value of $A(z)$ varies: in the section of the pore not containing the sphere, $A(z) = \pi D^2/4$; in the section containing the sphere,

$$A(z) = \frac{\pi}{4}(D^2 - d^2 + 4z^2). \quad (2.10)$$

After substituting this into Eq. 2.7 and performing the integral, the relative change in resistance is

$$\frac{\Delta R}{R} = \frac{D}{L} \left[\frac{\arcsin(d/D)}{(1 - (d/D)^2)^{1/2}} - \frac{d}{D} \right]. \quad (2.11)$$

See Fig. 2.3 for a plot of Eq. 2.11.

As mentioned above, Eq. 2.7 implicitly assumes that the current density is uniform across each slice. This will only be true in situations where the cross section of the pore varies very slowly with length, such as when a sphere of relatively large diameter (and thus large radius of curvature) inhabits the pore. For this reason, we expect Eq. 2.11 to apply only for spheres with diameters approaching that of the pore. Furthermore, any deviations from a uniform current density across each slice will cause the resistance to increase. Thus, Eq. 2.11 represents a lower bound on the estimated increase in resistance.

2.1.3 Intermediate Sphere Sizes

While Eqs. 2.8 and 2.11 describe the electrical resistance change in the small and large sphere limits, it is not clear how the resistance varies with sphere diameter in the regime between these limits. This intermediate regime was addressed by Anderson and Quinn[25] through the results of two papers by W. R. Smythe [26, 27]. Smythe performed numerical studies of the ideal fluid flow through a cylindrical pore containing a spheroid. One major conclusion of his work (whose details are beyond the scope of this presentation) is a calculation of the increased flow resistance in the pore due to the insertion of a spheroid. This result was presented as a table of the effective

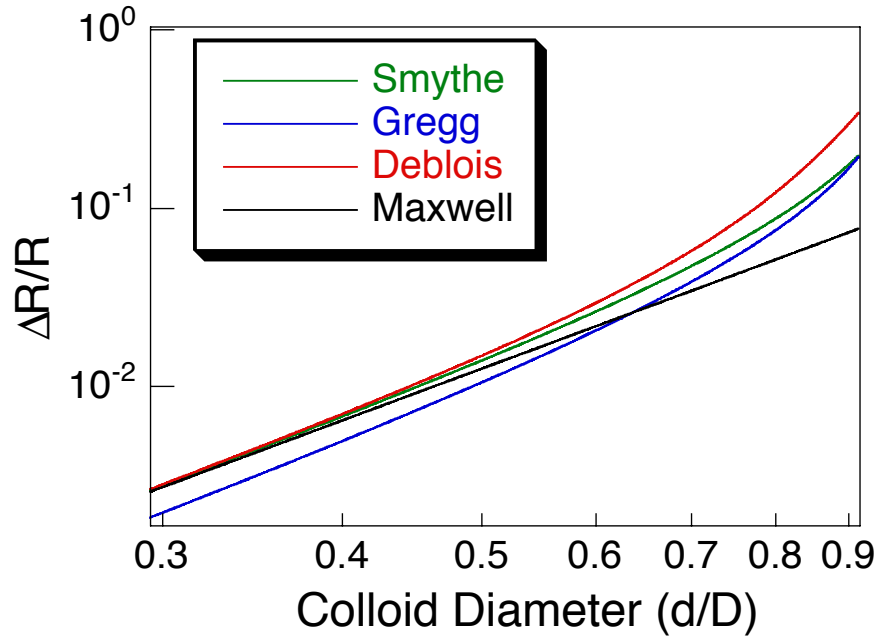


Figure 2.3: Plot of the analytical predictions of $\Delta R/R$ vs. the colloid diameter d/D . The black line represents the infinitely small sphere limit of Eq. 2.5, the red line represents the small sphere limit of Eq. 2.8, the green line represents the large sphere limit of Eq. 2.11, and the blue line represents the interpolation of Eq. 2.12

increase in the pore's hydrodynamic length caused by the insertion of spheres of various sizes. Anderson and Quinn compared these numerical results with the equations I have already presented (Eqs. 2.5, 2.8 and 2.11) by simply finding the increase in electrical resistance due to the Smythe's calculated effective increase in pore length. They found good agreement between Smythe's calculations and Eq. 2.8 in the limit of a small sphere, and with Eq. 2.11 in the limit of a large sphere. Importantly, this method allowed predictions of the regime between the small and large sphere limits.

By fitting to Smythe's results, Deblois *et al.* [6] found a single equation to predict the resistance change for all regimes of sphere diameter. The equation is essentially

the Maxwell result (Eq. 2.5) with a multiplicative correction factor:

$$\frac{\Delta R}{R} = \frac{d^3}{D^2 L} \left[\frac{1}{1 - 0.8(d/D)^3} \right]. \quad (2.12)$$

According to this equation, the electrical resistance change should closely (< 10%) follow the analytical result of Eq. 2.8 below diameter ratios of $(d/D) \approx 0.4$, and the analytical result of Eq. 2.11 above diameter ratios of $(d/D) \approx 0.9$, as plotted in Fig. 2.3.

2.1.4 Off-axis Spheres

In all the treatments presented, the sphere has been assumed to lie on the central axis of the pore. In reality, the sphere can lie at any position radially displaced from the central axis up until the sphere surface contacts the pore wall. This displacement affects the change in electrical resistance of the pore, and thus complicates attempts to relate the resistance change to the sphere diameter. We expect a sphere displaced from the pore axis to cause a larger resistance change than if it had traveled on the axis. This is due to the aforementioned argument concerning the distribution of current density on pore cross-sections: anything that increases the nonuniformity in current density on a cross-section will increase the resistance of the pore. A sphere travelling off-axis will clearly increase the non-uniformity, as it pinches the pore off on one side, and opens it up on the other,

To my knowledge, there are no analytical treatments of this problem. The only theoretical treatment I am aware of is a short paper by W. R. Smythe in which he extended his numerical work to find the effective length increase of a pore due to an off-axis sphere[28]. He found a significant off-axis effect on the electrical resistance. For example, his calculations predicted a 16% increase in resistance (compared to the on-axis resistance) for a particle of size $d/D = 0.4$ that travels off the pore axis by a fractional radial distance $x = b/R = 0.5$, where b is the radial distance between the pore axis and the sphere center (again, see Fig. 2.1 for variable definitions).

Berge *et al.* performed measurements to test Smythe's off-axis predictions[29], and found that the numerical results significantly overestimated the resistance change. The measurements on the geometry of $d/D = 0.4$ and $x = 0.5$ indicated a resistance change four times smaller than predicted. Berge *et al.* formulated a phenomenological equation that fit their results quite well:

$$\frac{\Delta R}{\Delta R_o} = 1 + \alpha \left(x \frac{d}{D}\right)^3, \quad (2.13)$$

where ΔR represents the change in resistance upon insertion of a sphere of diameter d into a pore of diameter D at a fractional off-axis coordinate x , ΔR_o represents the change in resistance for the same sphere located on the pore axis, and $4.2 < \alpha < 7.5$ is a numerical constant found to vary with the pore geometry. While Eq. 2.13 predicts a much smaller off-axis effect than Smythe's results, the effect is still quite large. Berge *et al.* measured typical maximum increases due to the off-axis effect of 8-10%. It is thus very important to take these effects into account when trying to measure precisely sphere sizes using the resistive pulse technique.

2.2 The Particle Transit Time

In addition to the change in electrical resistance, the second important measurable parameter in our experiment is the width of each resistive pulse, which indicates the transit time of a particle through the pore. Predicting this parameter is a hydrodynamic problem that is simplified by knowledge of the Reynolds number $Re = \eta U S / \mu$, where η is the fluid density, U is a typical fluid velocity, S is a typical length scale of the problem, and μ is the fluid viscosity. For the length scale ($S \sim 1 \mu\text{m}$) and fluid velocities ($U < 100 \mu\text{m/ms}$) we use, $Re < 0.1$, so we need only consider laminar flow. This allows two simplifications to the problem. First, the distance X for a fluid flow entering a pipe to settle to its stable parabolic profile depends on the pipe diameter D and Re : $X/D = Re/30$ [30]. Thus, in our system, the flow will attain the Poiseuille parabolic velocity distribution almost immediately upon entering the

pore. This allows us to ignore variations of the particle velocity at the entrance, and assume an infinitely long pore in attempting to find the particle velocity.

The second simplification is in the Navier-Stokes equation, which at low Reynolds number reduces to

$$\mu \nabla^2 u = \nabla p, \quad (2.14)$$

where μ is the fluid viscosity, u is the fluid velocity field, and p is the pressure. The problem is completely specified by Eq. 2.14, along with the boundary conditions and the continuity equation:

$$\nabla \cdot u = 0. \quad (2.15)$$

In our experiments, either electrophoretic force or a fluid flow can be used to drive the particle through the pore. Whichever is used, we expect the particle to attain a steady velocity in which the force applied to the particle is balanced by the retarding drag force on the motion of the particle through the fluid. The particle's (constant) velocity is thus completely determined by the drag force; consequently, most of the theoretical treatments of the problem solve the equations of motion (Eqs. 2.14 and 2.15) to find the drag.

Finally, note that the presentation that follows is not focused on the absolute value of the particle velocity, but rather its variation with off-axis coordinate. I do this because, in our experiment, we do not have a precise knowledge of the magnitude of the external forces that drive the particle through the pore. Since the theoretical predictions of the particle velocities presuppose knowledge of these forces, it is difficult to compare the absolute values of the measured transit times with the theory. We do not know the values of the applied forces because of the unknown charge on the particles when using electrophoresis, and the imprecise (although stable) pressure applied when flowing fluid. However, we have found the theoretical descriptions to be quite useful in comparing the experimental results on the variations in transit time with particle size and off-axis coordinate.

2.2.1 The Drag Coefficients

Since the drag force determines the particle velocity, the parameters that describe the drag must be defined. In an unbounded fluid, a sphere will experience a drag force according to Stokes law: $F_d = -6\pi\mu av_p$, where a is the particle radius and v_p is the particle velocity. Within the pore, the presence of the pore walls will change the drag force on the particle, which can be expressed as a multiplicative adjustment to Stokes law¹:

$$F_d = 6\pi\mu a\gamma_1(-v_p + \gamma_2 v_f), \quad (2.16)$$

where v_f is the maximum fluid velocity in the pore far from the particle, and $\gamma_{1,2}$ are coefficients accounting for the drag due to both the motion of the particle and the motion of the fluid. These coefficients will depend on the particle radius a , the off-axis displacement b , and the pore radius R . In the case of an applied electrophoretic force F_e and no fluid flow ($v_f = 0$), the steady state condition requires $F_e = -F_d$, and Eq. 2.16 becomes

$$v_p = \frac{F_e}{6\pi\mu a\gamma_1}. \quad (2.17)$$

When fluid is flowing through the pore, but no other force is applied, the steady state condition requires that the total drag $F_d = 0$, and Eq. 2.16 becomes

$$v_p = v_f\gamma_2. \quad (2.18)$$

Thus, γ_1 will determine the particle's velocity when an electrophoretic driving force is used, and γ_2 will determine the particle's velocity when a fluid flow is used. The theoretical results will thus be presented in terms of the coefficients $\gamma_{1,2}$.

2.2.2 On-axis Spheres

The only analytical solution for the drag coefficients $\gamma_{1,2}$ relevant to spheres of all sizes applies only to on-axis spheres. In order to present a complete description of the

¹I assume all forces and velocities in the pore are parallel to the z-axis; I will ignore transverse motion

problem of the velocity of a sphere in a fluid-filled pore, I show the analytical solution here. However, because of the aforementioned concerns about the absolute values of the transit time, this result is not useful for direct comparison with experiment, and so I will present it without comment. For a sphere on the pore axis, Bohlin[31] has calculated $\gamma_{1,2}$ using a method of reflections described in Ref. [32]². Expressed as a polynomial in the sphere to pore radius ratio a/R , he finds

$$\begin{aligned} \frac{1}{\gamma_1} = & 1 - 2.10443\left(\frac{a}{R}\right) + 2.08877\left(\frac{a}{R}\right)^3 - 0.94813\left(\frac{a}{R}\right)^5 \\ & - 1.372\left(\frac{a}{R}\right)^6 + 3.87\left(\frac{a}{R}\right)^8 - 4.19\left(\frac{a}{R}\right)^{10} + \dots \end{aligned} \quad (2.19)$$

$$\begin{aligned} \gamma_2 = & 1 - \frac{2}{3}\left(\frac{a}{R}\right)^2 - 0.1628\left(\frac{a}{R}\right)^5 - 0.4059\left(\frac{a}{R}\right)^7 \\ & + 0.5326\left(\frac{a}{R}\right)^9 + 1.51\left(\frac{a}{R}\right)^{10} + \dots \end{aligned} \quad (2.20)$$

2.2.3 Off-axis Spheres

Happel and Brenner[32] present a solution to Eqs. 2.14 and 2.15 for the case of an off-axis sphere that is much smaller than the pore $a \ll R$. In that case, γ_2 simply reflects the parabolic profile of the flow velocity (if present) within the pore:

$$\gamma_2 = 1 - \left(\frac{b}{R}\right)^2. \quad (2.21)$$

The situation for γ_1 is more complicated. For spheres near the cylinder axis, $b/R \sim 0$, they find the first two terms to be

$$\gamma_1 = 1 + \frac{a}{R} \left[2.10444 - 0.6977\left(\frac{b}{R}\right)^2 + \dots \right]. \quad (2.22)$$

In the opposite limit of spheres closely approaching the pore wall, $b/R \sim 1$, an exact calculation is possible:

$$\gamma_1 = 1 + \frac{a}{R} \left(\frac{9}{16} \right) \left(\frac{1}{1 - b/R} \right). \quad (2.23)$$

²For the same geometry, Paine and Scherr[33] present a highly accurate table of the values of $\gamma_{1,2}$ for a variety of values of a/R .

Note that, with increasing b , Eq. 2.22 predicts a decrease in γ_1 , while Eq. 2.23 predicts an increase; thus, γ_1 must attain a minimum at some intermediate value of b . In a numerical extension of the approach taken by Happel and Brenner, Famularo (see Ref. [32]) found this minimum to occur at $b/R \sim 0.4$. Recall that a sphere under constant applied force, in a pore with no net fluid flow, travels with a velocity inversely proportional to γ_1 (Eq. 2.17) We are then led to the surprising result that this small sphere will travel at a maximum velocity if located at $b/R \sim 0.4$, and not on the pore axis. This result has not been clearly verified experimentally, probably because of the relatively shallow ($\lesssim 1\%$) nature of the minimum of γ_1 (see Fig. 2.4).

Higdon and Muldowney[34] have performed extensive numerical computations to find the behavior of $\gamma_{1,2}$ as a function of both particle size and off-axis coordinate. In their paper, they state that their results agree well with those of Bohlin (Eqs. 2.19 and 2.20) for on-axis particles; however, the behavior of the drag coefficients with off-axis coordinate is most relevant for us. In Fig. 2.4 I plot the dependence of γ_1 with relative off-axis coordinate b/R for a variety of particle sizes as found by Higdon and Muldowney. Also plotted is Famularo's predicted dependence for γ_1 for small particles, which is qualitatively similar to Higdon and Muldowney's results. From these plots, it is clear that the minimum of γ_1 does not vary significantly from $b/R \sim 0.4$ for particle sizes $a/R \lesssim 0.5$.

As already mentioned, γ_2 is the relevant drag parameter for a sphere under the influence of a net fluid flow, but no other force. Higdon and Muldowney's results[34] for the off-axis behavior of γ_2 are not relevant to our experiment due to a difference in boundary condition. Eq. 2.16, which forms the basis of their results, defines the value v_f as the maximum velocity of the fluid in the pore that *contains* a sphere. This amounts to a condition of constant mass flow through the pore, and is analogous to a constant-current condition in electrostatics. In our experiment, the pressure across the pore is kept constant (analogous to a constant-voltage condition). The mass flow through the pore will depend on the pore's hydrodynamic impedance (a hydrodynamic Ohm's law); this impedance will change when the pore is occupied

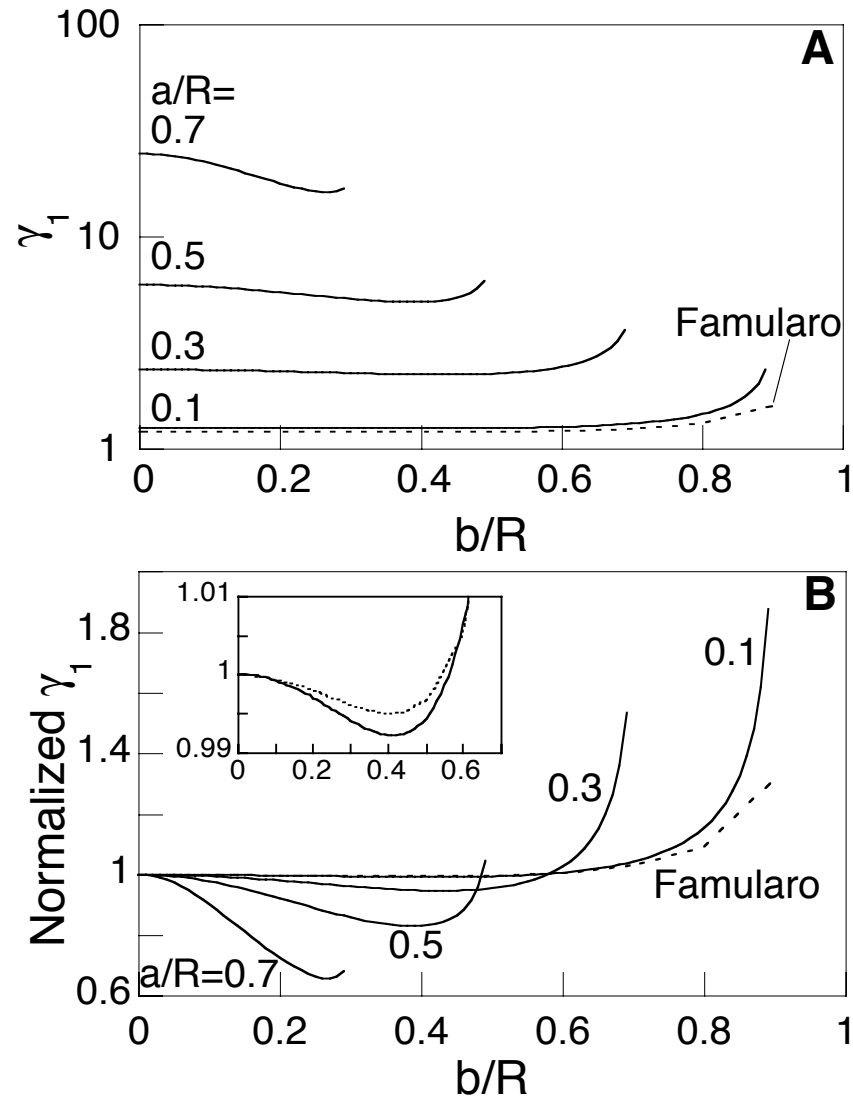


Figure 2.4: Higdon and Muldowney's[34] results for the drag coefficient γ_1 vs. off-axis coordinate b/R for spheres of relative diameter $a/R = 0.1, 0.3, 0.5, 0.7$. Also plotted as the dotted line is Famularo's[32] result for very small spheres. In **A** the absolute value of γ_1 is shown, while in **B**, each curve is normalized by the on-axis value in order to emphasize the minimum. The inset in **B** shows the behavior of the $a/R = 0.1$ and Famularo curves near the minimum.

by particles of different sizes. Thus v_f is not a constant within a single experiment using particles of different sizes, and Higdon and Muldowney's results for γ_2 are not applicable. However, note that Eq. 2.21 is still applicable since in the limit of very small spheres the constant-flow and constant-pressure conditions are equivalent (essentially because the hydrodynamic impedance of the pore hardly changes when a very small sphere enters).

To find an expression for the velocity of particles in a pore that is carrying a fluid flow, we turn (again) to the work of Berge[35]. Based on a polynomial fit to the data of Goldsmith and Mason[36], Berge proposed a phenomenological expression for the velocity of a particle v_p in a pore subject to a fluid flow:

$$v_p = v'_f \left(1 - \left(\frac{b}{R}\right)^2\right) \left(1 - \frac{2}{3}\left(\frac{a}{R}\right)^2 - 15.57\left(\frac{a}{R}\right)^2\left(\frac{b}{R}\right)^5\right) \quad (2.24)$$

where $v'_f = R^2\Delta P/4\mu L$ is the maximum Poiseuille fluid flow velocity for the pore of length L *without* a sphere, subject to an applied pressure ΔP . The form of this relation for a variety of sphere sizes is shown in Fig. 2.5. This equation is applicable to our experiment, since it relates the particle velocity to a constant pressure difference rather than a constant fluid flow. In the limit of a very small sphere, $v'_f \approx v_f$, and Eq. 2.24 reduces to the simple parabolic dependence of Eq. 2.21 for off-axis spheres, and also agrees with the first terms of Eq. 2.20 for on-axis spheres.

2.2.4 Electrophoresis vs. Hydrodynamic Drag

The off-axis effect on particle velocity v_p is markedly different for the two types of driving forces considered here. When there is no fluid flow through the pore and the particles are subject to a constant external electrophoretic force, $v_p \propto 1/\gamma_1$, and Higdon and Muldowney's results for γ_1 (shown in Fig. 2.4) are relevant. When the particles are driven by hydrodynamic drag, the particle velocity is determined by Eq. 2.24, and is plotted in Fig. 2.5. Comparing the two plots, it is clear that the off-axis effect on transit time is simpler and stronger when fluid flow is used. The behavior is simpler because v_p monotonically decreases with off-axis coordinate b/R

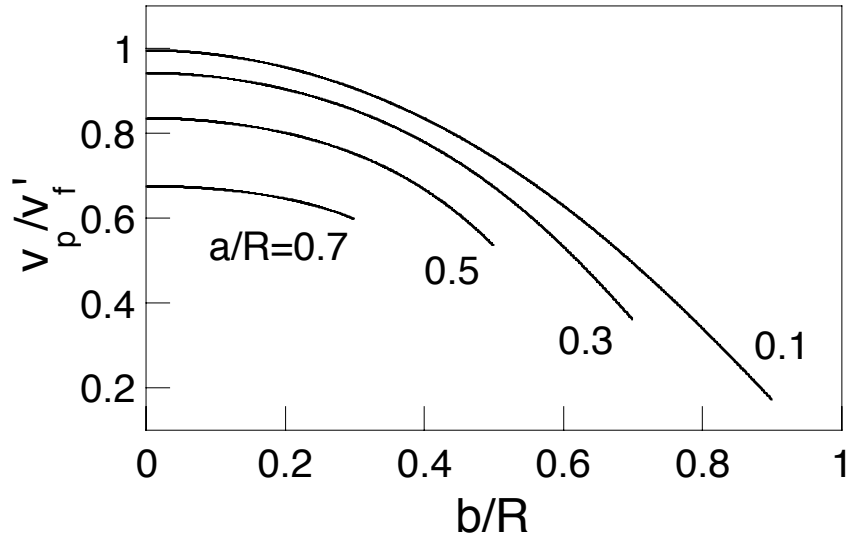


Figure 2.5: Relation of normalized particle velocity v_p/v_f' to off-axis coordinate b/R when using fluid flow to drive particles through the pore. The curves are plotted for various values of the relative sphere size $a/R = 0.1, 0.3, 0.5, 0.7$ according to Eq. 2.24.

when using fluid flow, as compared to the change in slope seen in γ_1 when using electrophoresis. The behavior is stronger because, for all but the largest sphere sizes, the maximum variation in velocity between on and off axis spheres is much larger when using fluid flow; for example, at $a/R = 0.1$, the velocity of the fluid-borne particle varies by about a factor of five, while the velocity of electrophoretically-driven particles varies by less than a factor of two. The differences between the two types of forces should thus be clear in the experimental data, which will be discussed in Chapter 5.

2.3 Summary

In this chapter, I have presented equations that describe the effect of spheres (of various sizes and off-axis positions) on the height and width of the resistive pulses

they cause. The pulse height (electrical resistance change) is very sensitive to the sphere size, as described for on-axis spheres by three equations (shown in Fig. 2.3): Eq. 2.8 in the limit of small spheres, Eq. 2.11 in the limit of large spheres, and Eq. 2.12 in between. The variation of the resistance change with off-axis position can be expressed as a multiplicative correction that is proportional to the cube of the off-axis coordinate (Eq. 2.13). The pulse width (particle transit time) can be found by finding the particle velocity, which is entirely dependent on the effects of drag forces. The variation of the width with off-axis coordinate differs significantly according to the type of force used to drive the particle: when electrophoresis is used, a complex behavior including a maximum in the particle velocity at $b/R \sim 0.4$ is expected (see Fig. 2.4); when fluid flow is used, a relatively simple and strong effect is expected (see Eq. 2.24 and Fig. 2.5).

In the next chapter, I will discuss our measurements of the electrical resistance change and their comparison with the theoretical predictions. In Chapter 5, the experimental evidence for the various off-axis effects will be discussed, and I will present our method for removing the effects so as to increase the resolution of the device.

Experimental Protocols

In our work, performing a resistive pulse measurement involves three separate steps: fabricating the device (the electrodes, reservoirs and pore), preparing the solution to be analyzed, and acquiring the data. In this chapter, I describe in general terms the procedures we have used to accomplish each step. Specific recipes for the preparation and use of cleaning solutions and for performing photolithography (PL) and electron-beam lithography (EBL) are listed in Appendix A.

3.1 Device Fabrication

Utilizing modern microfabrication techniques allows us to fabricate devices rapidly, reproducibly, and with significant flexibility in design. We use both optical and electron-beam lithographies to create patterns that are either transferred to a substrate through metal deposition or reactive ion-etching (RIE), or used as molds for polydimethylsiloxane (PDMS), a curable rubber. These transferred patterns form the pore, reservoirs and electrodes of the finished device.

We have fabricated two basic types of devices: one in which the pore and reservoirs are etched into a quartz substrate, and one in which the the pore and reservoirs are embedded into a slab of PDMS. The former is used to in the experiments described in Chapter 4, and the latter in the experiments described in Chapters 6 and 7 (Chapter 5 discusses experiments that use both types of devices). In this section, I will describe

the basic steps in the construction of each type of device; some specialized features of particular devices will be described in later chapters.

3.1.1 Etched Quartz Devices

The first stage of fabrication is the patterning of the pore. A line is patterned in resist on a clean quartz substrate using either PL for line widths $\geq 1 \mu\text{m}$, or EBL for line widths between 100 and 500 nm. This line is then etched into the quartz using a CHF_3 RIE, forming a long channel with a depth comparable to its width. The substrate is then cleaned thoroughly.

After the pore is patterned, the substrate subsequently undergoes a second stage of PL and RIE to define two reservoirs that are $100 \mu\text{m}$ wide and $3.5 \mu\text{m}$ deep. The reservoirs are connected to each other by the previously-defined channel. The length of the pore is defined in this second stage by the separation between the two reservoirs; typically pores that are $1 \mu\text{m}$ wide will be $\sim 10 \mu\text{m}$ long, and pores with smaller EBL-defined widths will be 3-5 μm long. The length is chosen so that the pores will be much longer than wide. After this stage, the substrate is again cleaned thoroughly.

The final stage of fabrication consists of using PL to pattern four electrodes transverse to the reservoirs. Four electrodes are needed because, as will be described later, we utilize a four-point technique to measure the current through the pore. The inner electrodes are placed quite close to the pore ($\sim 50 \mu\text{m}$ away), while the outer electrodes are a few millimeters away. After creating the electrode pattern, we perform two depositions of 50/250 \AA Ti/Pt in an electron-beam evaporator with the sample positioned $\pm 45^\circ$ from normal to the flux of metal; this is done to ensure that the electrodes are continuous down both walls of the reservoirs. At this point, the fabrication of the substrate is complete; a typical device is shown in Fig. 3.1.

The device must be sealed on top with a PDMS-coated glass coverslip before each measurement. PDMS is a clear siloxane elastomer that, when cured, seals hermetically

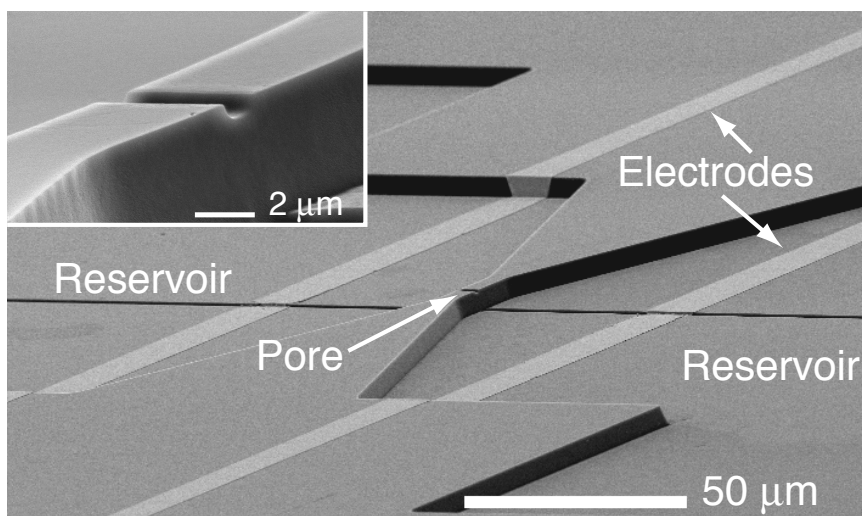


Figure 3.1: Scanning electron micrograph of an etched quartz device. The $3.5\ \mu\text{m}$ deep reservoirs and the inner Ti/Pt electrodes are only partially shown. The outer two electrodes are not visible in this image. The inset shows a magnified view of this device's pore, which has dimensions $5.1 \times 1.5 \times 1.0\ \mu\text{m}^3$.

to flat substrates. Here, we increase the stiffness of the PDMS by backing it with a coverslip; this keeps the PDMS from collapsing into the reservoirs. Clean coverslips are coated in PDMS by spinning on a layer of uncured PDMS (mixed at a 10:1 ratio or resin to catalyst), then baking at $80\ ^\circ\text{C}$ for several hours. The PDMS layer is generally very flat at the center of the coverslip, but forms a bead around the edge which must be removed for proper sealing to the substrate. This is done by sealing the coated coverslip (PDMS side down) to a clean glass slide, then scribing and cracking the coverslip so as to remove the beaded region.

Prior to sealing, both the PDMS and the substrate are oxidized in a dc air plasma to insure the hydrophilicity[37] of the reservoir and pore and to strengthen the seal[38] to the quartz substrate. On PDMS, the effect of the plasma is to change the hydrophobic methyl groups on the surface into polar, hydrophilic silanol groups[37], as diagrammed in the first step of Fig. 3.3. With time, the silanol groups diffuse back

into the bulk of the PDMS, decreasing the hydrophilicity of the surface[39]; thus it is important to seal and wet the device soon after the plasma treatment. Also, it is important not to apply the plasma for too long¹, otherwise the plasma will create a thick silica layer on the PDMS, which will buckle due to thermal expansion differences with the bulk PDMS[40]. On quartz, the plasma's effect is similar in that it creates silanol groups. However, the effect does not decay with time.

The device is sealed by simply placing the PDMS side of the coverslip onto the substrate; typically the PDMS will conform immediately to the surface with at most a light tap. Upon sealing of the PDMS to the coverslip, the silanol groups on each surface most likely utilize intervening water molecules (adsorbed from the air) to create a network of hydrogen bonds that links the two surfaces very strongly² (see the diagram in the last step of Fig. 3.3). In this way, we can be sure that no leaks will occur around the pore or out of the reservoirs. Solution added to the edge of the coverslip wets the hydrophilic reservoirs and pore by capillary action. In some cases, it is helpful to use vacuum grease to keep the solution from traveling around the entire chip. Measurements are done in a closed, humidified box so as to reduce the evaporation of the solution.

After each measurement, the coverslip is removed by soaking the device in a solution of Amtex CCR, which slowly dissolves the PDMS. The substrate is then gently cleaned, and can be reused. In some cases, the electrodes will be damaged during the measurement or the cleaning process; if this occurs, the damaged electrodes are stripped off of the substrate and remade. In this manner, each device can be used several times.

¹As described in Appendix A, 10 s is a typical oxidation time; buckling problems can occur for treatments longer than 60 s.

²While we have no direct evidence of the formation of a hydrogen-bonded network, we believe it occurs based on other analogous wafer-bonding techniques[41].

3.1.2 Molded PDMS Devices

Fabrication of a molded PDMS device begins with creating a master, from which a slab of PDMS will eventually be cast (a method known as micromolding[42]). The master is created by fabricating raised ‘negative’ structures in resist that subsequently become embedded ‘positives’ in the PDMS. First, the raised line that will become the pore is created. This can be done in a number of ways. PL is used to create in photoresist a long raised line, $\sim 1\mu\text{m}$ by $1\mu\text{m}$ in cross section, on a quartz or SiO_2/Si substrate. This line is then transferred to the substrate using an RIE process. Alternatively, it is possible to use a very durable photoresist that will become part of the final master— we have used the resist SU8-2002 to achieve this. Using a photoresist is faster, since the RIE step can be skipped.

To create smaller (~ 300 nm wide and high) pores, an EBL process must be used. Just as with the PL process, this can be done in two ways,: either a RIE process can be used to create the final raised line, or a durable negative resist can be used (we have used polystyrene). Here, we have found it preferable to use the RIE process, as it appears to create more uniform devices. In either case, it is difficult to create pores with diameters less than 200 nm using PDMS micromolding and EBL structures, as the PDMS is not able to hold well-defined structures at shorter length scales[43].

The next step in fabrication of a master is to create the raised features that will become the reservoirs. This is done by using PL to pattern an SU8-type resist. As mentioned, crosslinked SU-8 photoresists are exceptionally strong and can be used as part of the final master. The resist thickness can be tuned over a wide range to match the desired final reservoir depth; typically we use 5-15 μm thick layers. Two reservoirs are patterned into the SU-8, and spaced at a distance equal to the final desired pore length. Once this step is accomplished, the master is complete; a typical master containing an EBL defined pore is pictured in Fig. 3.2.

The completed master must now be cast. PDMS is mixed at a 10:1 resin:catalyst

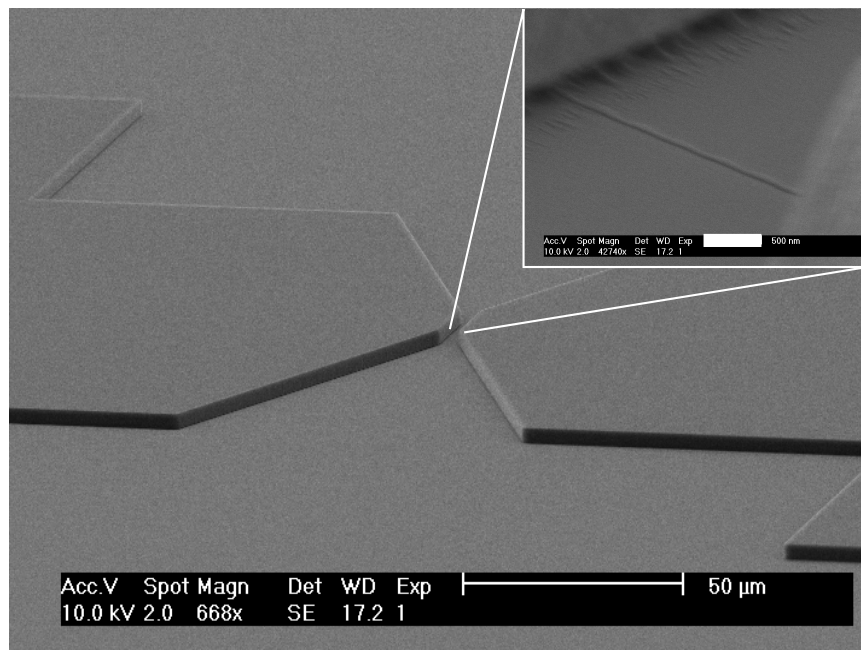


Figure 3.2: Electron micrograph of a master containing an EBL defined pore. The larger image shows the raised SU-8 structures that will be cast as the reservoirs, while the inset shows an EBL-defined polystyrene line that will be cast as the pore. The scale bar in the inset is 500 nm.

ratio and degassed in a vacuum chamber. The masters are treated with hexamethyldisilazane (HMDS, a common PL primer) to prevent PDMS-substrate bonding, and the degassed PDMS is poured onto each master to create a ~ 3 mm thick layer. The assembly is then cured for at least 24 hours at 80 °C to insure stable mechanical properties. Immediately prior to measurement, PDMS slabs with the embedded pore and reservoirs are cut from each master. Access holes are cut into each slab by coring with a needle. Each slab is cleaned by either a 5 minute wash in a solution of 1% Tween 20 (Sigma) followed by extensive rinsing in deionized water, or by sequentially rinsing in acetone, isopropanol and water. After removal of the PDMS, each master is cleaned by rinsing in isopropanol; it can then be treated with HMDS, and recast. Masters can be reused indefinitely.

The electrodes for the measurement of electrical current are patterned on glass coverslips by PL in AZ 3318D resist, and are formed by depositing 5 nm of Titanium and 25 nm of Platinum in an electron-beam evaporator. Immediately prior to sealing to the PDMS, the coverslips are cleaned in a dilute RCA SC1 cleaning solution, and rinsed in copious amounts of deionized water. This process creates a clean, hydrophilic, silanol-terminated surface.

The procedure for bonding the PDMS slabs to the electrode-bearing coverslips is diagrammed in Fig. 3.3. The cleaned PDMS slabs are first treated in an air plasma. A 5-10 μL drop of a deionized water/methanol mixture is placed on top of a clean electrode-bearing coverslip, and then the plasma-treated PDMS slab is placed on the coverslip feature side down. The water allows the slab to slide on top of the coverslip for alignment of the pore between the electrodes. Once aligned, the PDMS/coverslip assembly is placed on a hot plate and subjected to a 10 minute bake ramped from 50 °C to 150 °C. This bake serves to drive off the water and induce a strong bond (probably a network of hydrogen bonds) between the PDMS and coverslip. As before, the bond formed between hydrophilic PDMS and silica surfaces is essentially permanent. The device is now ready for addition of solution and measurement. Fig. 3.4 shows a schematic of a completed device.

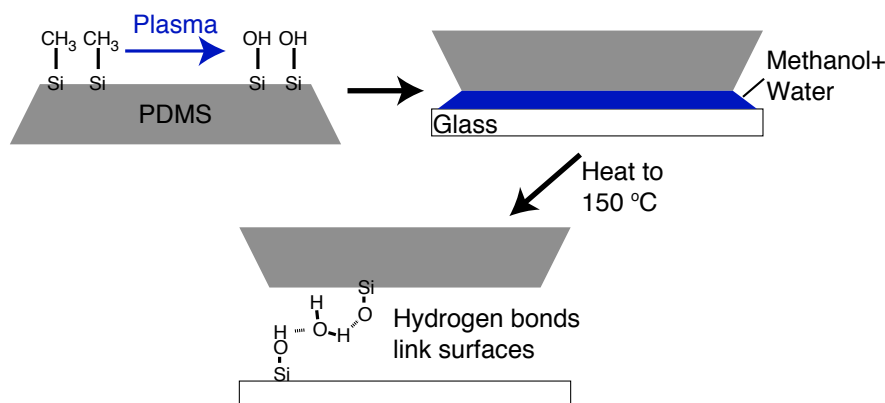


Figure 3.3: Diagram of the procedure used to permanently bond PDMS slabs to glass coverslips, as described in the text. In reality, the network of hydrogen bonds connecting the surfaces at the end of the procedure most likely involves many water molecules. These water molecules originate from the added solution when sealing embedded PDMS devices, and are adsorbed from the air when sealing etched quartz devices.

After measurement, devices are discarded. Since the masters can be reused indefinitely, it is much easier to recast the PDMS slab than it is to clean and reuse an already sealed device. Measurements can be performed more quickly when using PDMS embedded devices than when using the etched devices described in the previous section.

3.2 Solution Preparation

Once a device is completed, it must be filled with the solution to be measured. The solution's composition (content, concentration, pH) is chosen to fulfill several criteria. First, the particles (colloids or biological macromolecules) must be soluble and retain any desirable biological activity. Second, it must prevent the particles from aggregating or adhering to the walls of the reservoirs or pore. Finally, the solution must be sufficiently conductive so as to allow the passage of a measurable electrical

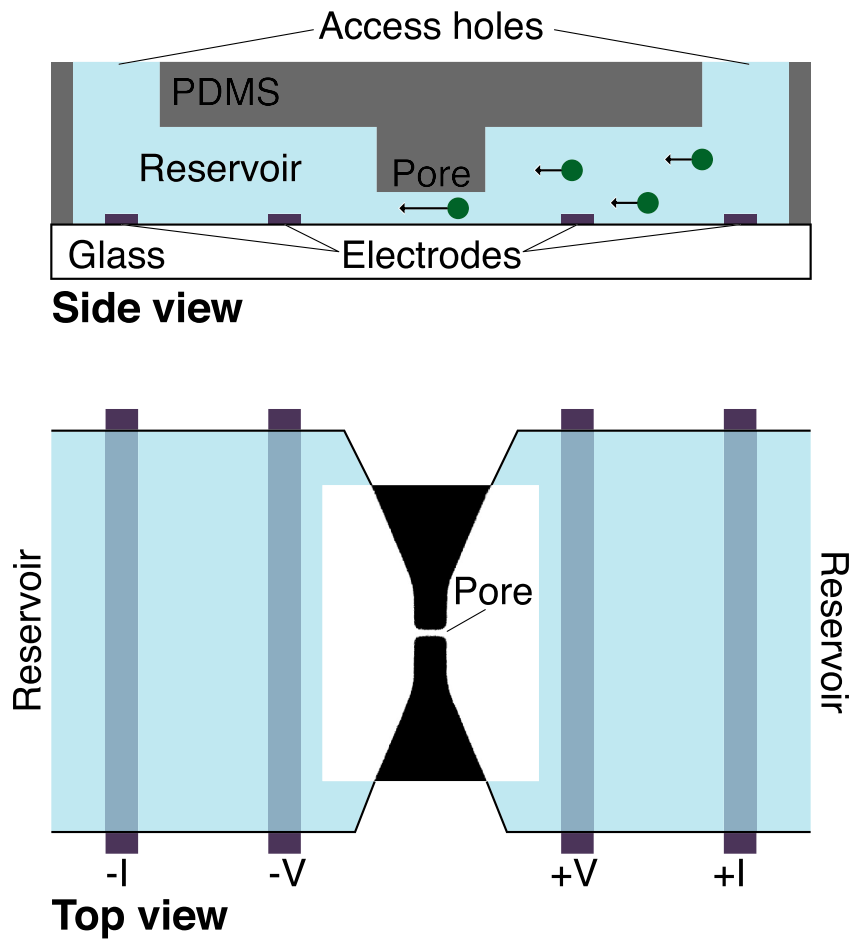


Figure 3.4: Schematic top and side views of an embedded PDMS device. Incorporated into the top view is an optical image of an actual sealed device containing a $7 \mu\text{m}$ long, $1 \mu\text{m}$ wide pore.

current.

3.2.1 Colloids

In Chapter 4, I present our measurements on carboxyl- and sulfate-coated latex colloids. When the colloids are dispersed in deionized water and added to a device, their high negative charge prevent them from sticking to the device's walls or to each other. However, deionized water will not efficiently conduct current, so salt must be added to the solution. As the salt concentration is increased, the charge on the colloids is shielded, and they can adhere to the device's walls. At high enough salt concentrations (typically ≥ 20 mM NaCl), all of the colloids in the device will adhere to the walls. This is circumvented by adding a surfactant to the solution, which acts as a detergent to keep the colloids soluble. For the actual measurements of these colloids, we use a 5x Tris-Borate-EDTA buffer at pH 8.2. This concentration of electrolyte would cause adhesion, so 0.05% volume to volume (v/v) of the surfactant Tween 20 is added. In general, colloidal solutions are diluted significantly (typically by factors of 100-1000) from their stock levels to avoid jamming in the pore.

In the work presented in Chapter 6, protein-coated colloids are used extensively. These colloids are more difficult to work with than the simple carboxyl or sulfate coated types due to their smaller charge. Here, we use a solution of 0.5x phosphate-buffered saline at pH 7.3, which is necessary for the proteins to bind in each experiment. Because the electrolyte concentration is fairly high, surfactant must be added to keep colloids from adhering to the device walls. We have found a combination of 0.2 mg/mL bovine serum albumen (BSA) and 0.05% Pluronic F127 surfactant to be quite effective.

A second concern when working with the protein-coated colloids is aggregation. Aggregates that contain four or more colloids have the potential of clogging the pore. While the surfactant helps prevent aggregation, we have not found a solution that completely removes it; rather, we generally try to break up aggregates by employing

a combination of mechanical methods: vortex mixing, ultrasonication, and especially repetitive aspiration with a micropipette. A solution treated in this manner will, with time, re-aggregate; thus, it is necessary to treat each solution immediately prior to a measurement.

3.2.2 DNA solutions

In Chapter 7, I present our measurements of DNA molecules passing through embedded PDMS pores. DNA molecules carry a very high charge that makes adhesion to the device walls unlikely in solutions with salt concentration ≤ 50 mM NaCl. Because of this, it is generally unnecessary to work with surfactant in any solution of DNA. However, we have frequently visually observed the clogging of fluorescently stained DNA molecules in the pore, and have electrically measured the clogging of unstained molecules. Presumably this occurs because, when the DNA is forced into close contact with the PDMS, there is the chance that it will become threaded between the polymers of PDMS, and thus get caught[44]. As of this writing, we have not found a solution that prevents this from occurring.

3.3 Measurement

Once a completed device is wet with a solution of particles, the particles must be made to flow through the pore, and the electrical current through the pore must be measured. In this section I describe how these are accomplished.

3.3.1 Inducing Particle Flow

There are two basic methods for inducing the particles in the solution to pass through the pore: electrophoresis, in which an applied electric field causes particle motion, and fluid flow, in which pressure applied to one reservoir causes a fluid flow which carries particles through the pore. The main difference between the two is that the

former only moves the particles (assuming they are charged), while the latter causes the fluid, along with everything in it, to move through the pore. In practice, this means that electrophoresis is a cleaner method: any foreign objects in the solution that might clog the pore will generally not have a very high charge, thus only the (charged) particles of interest will move. However, not all particles of interest are charged, and fluid flow must be used in those cases.

Electrophoresis is easy to achieve, since electrodes are already fabricated on the devices for the purpose of measuring the current. The same voltage used to measure the current is used to manipulate the particles; typically application of 0.5 V will cause DNA molecules to transit an EBL-defined pore 4 μm long in a few milliseconds, or 500 nm diameter carboxyl-coated colloids to transit a PL-defined pore 10 μm long in 50-100 ms. A byproduct of the application of voltage in microfluidic channels is electro-osmosis, the movement of the fluid in response to an applied field. Electro-osmosis occurs when the walls in contact with the fluid are charged. Charge neutrality requires the fluid to carry an equal and opposite charge; thus the fluid will flow when an electric field is applied. In our devices, the walls of the channels tend to carry a negative charge (due to the silanol groups), so the fluid will carry a positive charge—this allows us to distinguish the electrophoretic motion of negatively-charged particles from the oppositely-directed electro-osmotic flow of a positively-charged solution. While electro-osmotic effects have been seen in our devices when utilizing very high voltages (> 10 V), they do not appear to be significant at the voltages used in a typical measurement.

Pressure-induced fluid flow is used only with the embedded PDMS devices. Once the device is wet with solution, pressure can be applied to either reservoir using a commercial microfluidic pump. The pump is connected to the device through 0.020" ID/ 0.060" OD Tygon tubing that is inserted into the access holes in the PDMS slab (see Fig. 3.5). 7-14 kPa (1-2 psi) is typically applied during measurements, and will induce a 500 nm diameter colloid to transit the pore in a few hundred microseconds. Clogs in the pore occur occasionally due to either colloidal aggregates or unwanted

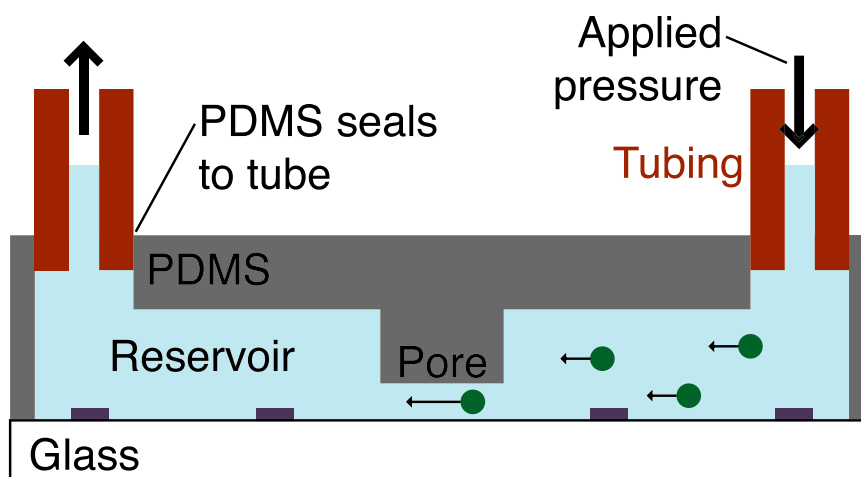


Figure 3.5: Method for pumping fluid through an embedded PDMS device

objects, but they can usually be cleared by application of higher pressures (up to 20 psi), without any effect on the PDMS/coverlip seal.

3.3.2 Circuit Design

As mentioned in Chapter 2, one of the two relevant experimental parameters is the change in the electrical resistance of the pore caused by an entering particle. Measuring this change requires either control of a constant voltage across the pore while measuring the current, or control of a constant current through the pore while measuring voltage. Circuits using both strategies have been used in previous resistive pulse measurements; here, we utilize the constant-voltage setup.

Whenever two electrodes are placed in solution, and a voltage is applied across them, a phenomenon known as electrode polarization occurs. Ions in the solution are drawn to the oppositely-charged electrode, creating a double layer of charge: the layer of electronic charge on the electrode itself, and the layer of ions in the solution just outside the electrode. If there is little charge transfer across the fluid/electrode interface, then most of the voltage applied to the electrodes will be dropped across

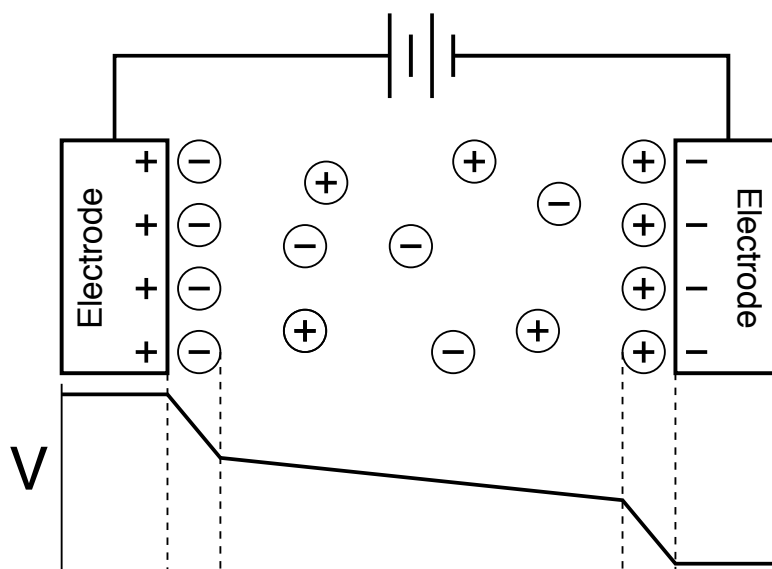


Figure 3.6: Schematic of the potential drop caused by double layer formation on electrodes in solution. In reality, the layer of counterions surrounding each electrode will be both adsorbed on the electrode, and dispersed nearby in a diffuse cloud (with an ion density greater than that in the bulk solution).

the two double layers (one on each electrode), and there will be very little current or electric field within the bulk solution, as diagrammed in Fig. 3.6. Typically, of course, there is charge transfer across the interface due to either adsorption and desorption of ions on the electrode, or electrochemical processes. Any electrochemical process will only occur once the threshold potential for the reaction has been reached. Thus for efficient conduction through the bulk solution, the electrodes in the reservoirs should be designed to have a low potential electrochemical reaction with the solution so that the potential applied across the electrodes is not lost to the double layers.

In most resistive pulse measurements, this is accomplished by using AgCl electrodes. By using an AgCl electrode with a large surface area, the electrode/fluid interfacial resistance will be minimized. In our experiment, this cannot be done—our reservoirs have been miniaturized, so only small electrodes can be used, and all

of our attempts to create an AgCl electrode (by plating Cl onto a deposited Ag film) have resulted in an inability to seal the PDMS to the substrate due to the thickness of the AgCl layer. Thus, we are forced to use electrodes that will have a significant potential drop across the electrode/fluid interface due to the electrode polarization effect.

However, by utilizing a four-point measurement of the electrical properties of the pore, we insure that the potential drop across the double layers does not affect our control of the voltage across the pore. This technique separates the electrodes that carry the current (the outer electrodes) from those that control the voltage (the inner electrodes). Since there is no current flowing through the voltage-controlling electrodes, there can be no potential drop between the electrode and the solution. The electrode polarization will still occur at the current carrying electrodes, but this is unimportant, as the potential drop of those electrodes has been removed from the critical part of the circuit by the four-point technique. The resistance of the fluid in the reservoirs is similarly removed.

Fig. 3.7 shows a diagram of the circuit we use to apply a constant voltage across the pore while measuring current. The design of the circuit is original, but was based on ideas presented in Ref. [45]. R_p and C_p represent the resistance and (parasitic) capacitance of the pore, while R_H and R_L represent the resistance of the fluid in the reservoirs on each side of the pore (along with any electrode/fluid interfacial resistance on the current-carrying electrodes I_H and I_L). The first amplifier (model INA110) outputs the sum of the voltage difference across the pore $V_H - V_L$ and the input voltage V_{in} . This becomes the inverting input of the second amplifier (model OP27), whose non-inverting input is connected to ground. In this feedback arrangement, the OP27 will output whatever current is necessary to make both input potentials equal (to zero, since one input is grounded). Thus, the circuit acts to set $V_H - V_L = -V_{in}$. All of the current through the pore runs from I_H to I_L to I_{out} , which is held at a virtual ground by an external current preamplifier (see Section 3.3.3 below).

The circuit elements R_f and C_f are critical to the frequency response of the circuit.

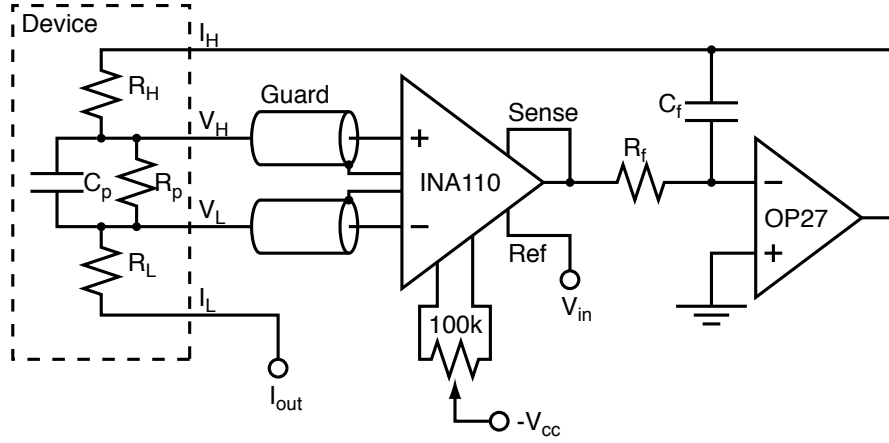


Figure 3.7: The electrical circuit used to perform the constant-voltage 4-point measurement. All circuit elements within the dashed box represent the impedances of the electrodes and fluid of the device.

Without those elements, the parasitic capacitance across the pore C_p will cause a 90° phase shift and an increased gain in the circuit for frequencies $\omega_p \geq 1/R_p C_p$. At those frequencies, this will change the negative feedback loop around the OP27 into a positive feedback loop, and the circuit will oscillate. This can occur at relatively low frequencies because the resistance R_p can be very large (nearly $1 \text{ G}\Omega$ in some cases). In order to maximize ω_p , driven guards are used on the connections between the device and the INA110 so as to minimize the value of C_p .

Addition of the elements R_f and C_f removes the oscillations by damping the frequency response of the circuit at frequencies above $\omega_f = 1/R_f C_f$. By tuning R_f it is possible to make $\omega_f = \omega_p$, in which case the limiting effect of R_f and C_f will exactly cancel the amplification caused by R_p and C_p . The circuit will then have a perfectly flat frequency response beyond ω_p . The high frequency response of the circuit is then limited by the low-pass filter formed by C_p and $R_H + R_L$. In practice, this is acceptable because $R_H + R_L \ll R_p$, and the frequency response will be relatively fast (typically tens of kilohertz).

The choice of the first amplifier is very important, since the electrodes V_H and

V_L are directly connected to its inputs. The design requires an amplifier with very low bias current (so as to not pass current through those electrodes), high input impedance, and low input capacitance. We have found the JFET input instrumentation amplifier INA110 to fit these criteria quite well. Any offsets caused by the input bias current, or voltage differences due to fluid flow on the device ('streaming potential') can be nulled using the offset circuit shown. We chose the OP27 as the second amplifier because of its precision and low noise.

3.3.3 Data Acquisition

The current through each device's pore is passed through an Ithaco current preamplifier that converts the input current into a voltage signal. The preamplifier has a built in adjustable low-pass filter, which can be used to limit the bandwidth of the measurement and thus reduce the noise. In some cases, this filter is used to correct for overshoot in the control circuitry that is not corrected by the choice of R_f and C_f . The preamplifier is usually used at a sensitivity of 10^{-8} or 10^{-9} A/V.

The output of the preamplifier is read in one of two ways: by connecting the voltage signal to a HP voltmeter or by sending it to a data acquisition board within a computer. The voltmeter reads data points at a maximum rate of 1 kHz into a GPIB bus, while the data acquisition board can digitize the data at a maximum rate of 100 kHz; however the voltmeter generally measures the voltage with greater precision. The voltmeter was used at its maximum rate for the data shown in Chapter 4, while most of the rest of the data was taken at 50 kHz using the data acquisition board.

Once the data is stored in a buffer within the computer on either the GPIB or data acquisition board, it is read and stored to file by a Labview program. Each file contains either ten thousand or twenty thousand points. After a measurement is completed, the raw data files are analyzed with a another Labview program that is designed to measure the height ($\delta I/I$), and width of every square pulse. These values are saved to a new file, and we analyze them further as is necessary.

3.4 Summary

In this chapter, I have described the materials and methods we use to fabricate devices, prepare solutions, and perform measurements. We use two different types of devices: one in which the pore and reservoirs are etched into quartz, and one in which they are embedded in PDMS. The former allows greater precision in our knowledge of the pore dimensions, while the latter is significantly easier and faster to fabricate. The solutions that are added to either type of device must fulfill two main criteria: they must not disturb any desired biological activity of the particles, and they must keep the particles dispersed (rather than aggregated or adhered to the device walls). Generally, the latter criteria is more difficult, and fulfilling it requires trial and error to find proper surfactants and salt concentrations. Finally, measurement is achieved using a four-point technique that removes spurious voltage drops (due to electrode polarization) from the sensitive part of the circuit. In the rest of this thesis, I will relate the various experiments we have performed using the techniques described in this chapter.

Quantitative Measurements of Polydisperse Colloidal Solutions

4.1 Introduction

In this chapter, I show the ability of our device to perform basic size-based differentiation of latex colloidal particles; this work demonstrates the first successful realization of a chip-based resistive pulse sensor. I also indicate the quantitative nature of the measurements by comparing the experimental results with the theory on the expected change in electrical resistance presented in Section 2.1. The experiments and analysis shown in this chapter and the next lay the quantitative groundwork for the use of our device to detect the binding of biological molecules to colloidal particles.

4.2 Experimental details

Latex colloidal particles of diameters ranging from 87 nm to 640 nm are measured using etched quartz devices. The fabrication of these devices is described in Section 3.1.1, and an electron micrograph of a device is shown in Fig. 3.1. After a device is constructed, we measure the dimensions of the pore using optical and atomic force microscopies.

The measured colloids are dispersed in a 5x concentrated TBE solution containing 0.05% v/v Tween 20 to reduce adhesion. The typical concentration of the colloids is 10^8 particles/mL. The current through the pore is measured using a four-point technique, as described in Section 3.3.2, with applied voltages ranging from 0.1 V to 1 V. This same applied voltage is used to electrophoretically drive the colloids through the pore. The current measurement is performed using a HP voltmeter that acquires data at 1 kHz, then transfers it to a computer over a GPIB bus.

4.3 Results

Fig. 4.1 shows typical measurements of the normalized current $\delta I/I$ vs. time. As mentioned previously, the normalized current is the useful experimental variable because it depends on neither the solution's conductivity nor the total amount of current passing through the pore. Drifts in the baseline current I do not affect the value of $\delta I/I$.

Each downward pulse in Fig. 4.1 represents a single colloid transiting the pore. Events in which two colloids simultaneously inhabit the pore are seen, but are easily differentiated from single particle events by their anomalous pulse heights and widths, as shown in Fig. 4.2. As shown in Fig. 4.1A, the passage of 87 nm particles is easily detected in a 8.3 μm long pore of cross section 0.16 μm^2 . Measurements of a polydisperse solution of colloids are shown in Fig. 4.1B; there are clear differences in the pulse heights caused by particles of different diameters.

For the data shown, 0.4 V is applied to the pore. In other data runs, we vary the applied voltage between 0.1 and 1 V to test the electrophoretic response of the colloids. We found that the transit time for a given type of colloid varied approximately as the inverse of the applied voltage, as is expected for the simple electrophoretic motion described by Eq. 2.17. Further discussion of the behavior of the transit time will take place in the next chapter.

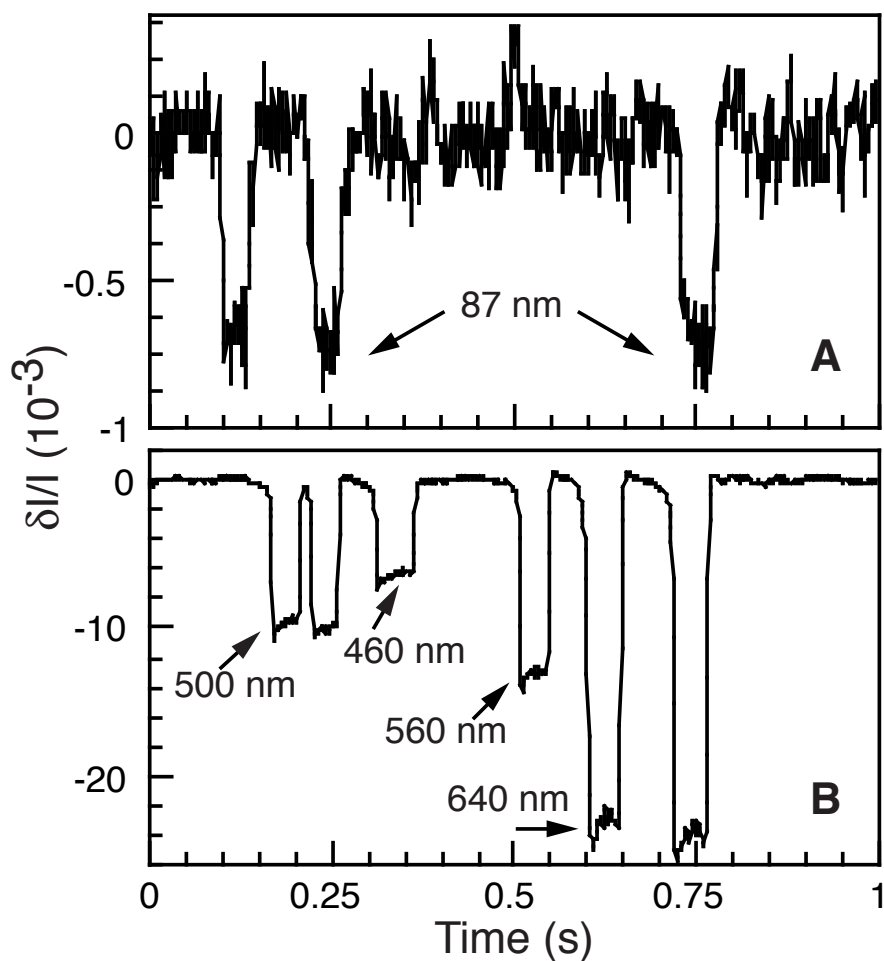


Figure 4.1: Measurements of the normalized current $\delta I/I$ vs. time on two different solutions of latex colloids. **A** shows measurements of 87 nm diameter colloids passing through a EBL-defined pore of length $8.3 \mu\text{m}$ and cross-section $0.16 \mu\text{m}^2$. **B** shows measurements of a polydisperse solution containing colloids of four different diameters (460 nm, 500 nm, 560 nm and 640 nm) passing through a PL-defined pore of length $9.5 \mu\text{m}$ and cross section $1.2 \mu\text{m}^2$.

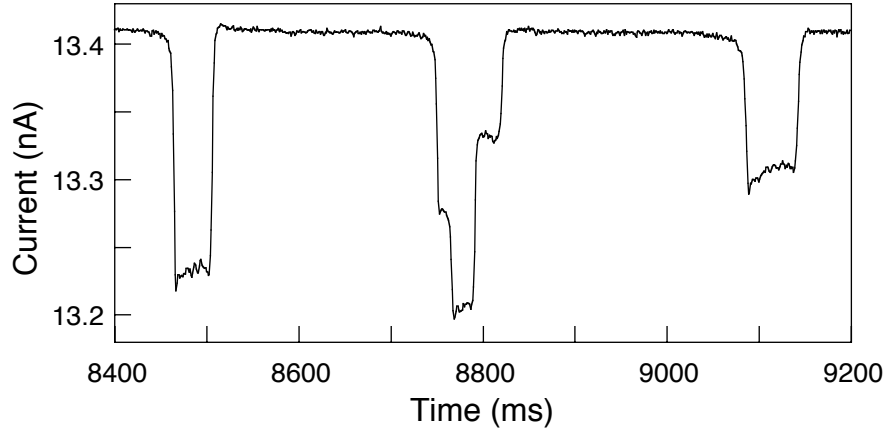


Figure 4.2: A current trace showing an event (center pulse) resulting from two colloids simultaneously inhabiting the pore; also shown are two single-colloid events (left and right pulses). Such two-colloid events are easily removed from the data analysis due to their anomalous shape. This data was taken on the same device used in Fig. 4.1B.

4.4 Discussion

Fig. 4.3 shows a histogram of ~ 3000 events measured for the same polydisperse solution shown in Fig. 4.1(b). The histogram emphasizes the ability of the device to separate colloids of different diameters. The widths of the peaks in the histogram represent the resolution of the device in sizing particles. We find that the response of the device for each type of colloid varies by 2-4%, which approaches the intrinsic variation of the diameter quoted by the colloid manufacturer. In the next chapter, I will discuss a strategy we have devised for further increasing the resolution of the device when utilizing fluid flow to drive particles through the pore.

We used a device with a pore of length $10.5 \mu\text{m}$ and cross-section $1.05 \mu\text{m}^2$ to measure, over several different runs, colloids ranging in diameter from 190 nm to 640 nm. The results of these measurements are shown in Fig. 4.4 as a plot of colloid diameter vs. pulse height. Also plotted are the theoretical predictions for the pulse height in the limit of large spheres (Eq. 2.11) and in the limit of small spheres (Eq. 2.8).

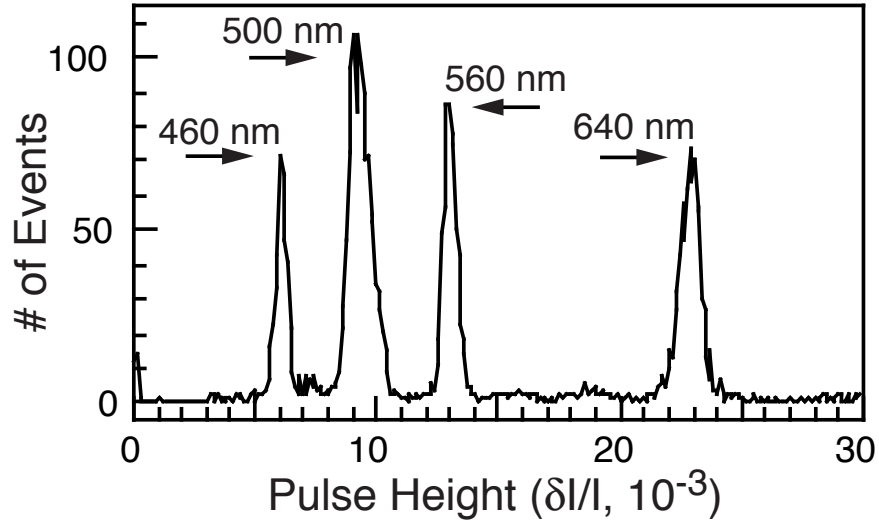


Figure 4.3: A histogram of ~ 3000 pulse heights resulting from measurements of the polydisperse solution shown in Fig. 4.1(b). Each peak in the histogram corresponds as labeled to a colloid population with a certain mean diameter.

As shown, there is excellent agreement between the measured pulse heights and those predicted by theory. As expected in the derivation of the equations (Section 2.1), the measured data more closely follow Eq. 2.8 in the limit of small spheres, and Eq. 2.11 in the limit of large spheres. I emphasize the fact that no curve fitting was performed in this plot; only the measured pore dimensions are used to generate the theoretical predictions.

The data show a transition from agreement with Eq. 2.8 to Eq. 2.11 at around 400 nm in diameter, equivalent to a ratio $d/D \sim 0.35$. Recall (Section 2.1.3) that Deblois et al.[6] used the work of Smythe[27] to find a prediction of the pulse height for all sphere sizes. This prediction, Eq. 2.12, indicates that the measured pulse heights should not closely agree with Eq. 2.11 below diameter ratios $d/D \sim 0.9$. As is clear in Fig. 4.4, this is not the case in our data. We speculate that the difference might be due to the shape of the cross-section of our pore. We use a nearly square pore, while the theory assumes a circular pore; this apparently does not affect the dependence of

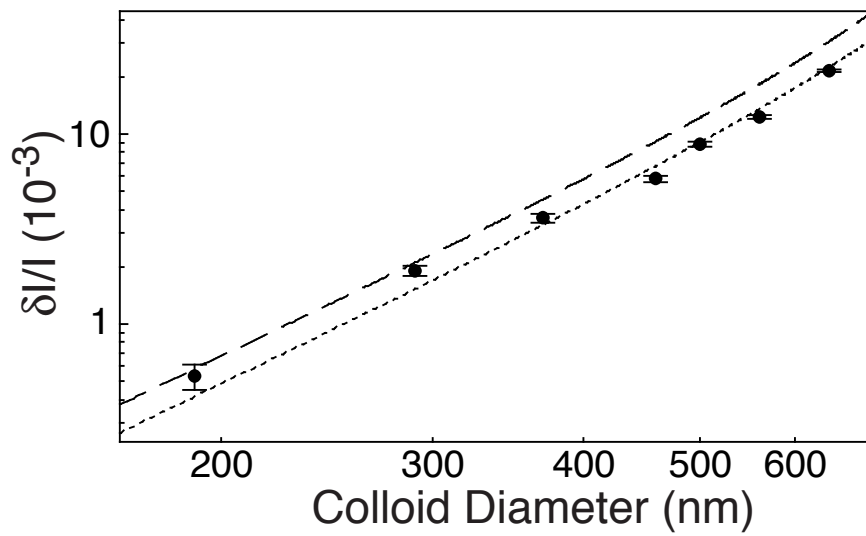


Figure 4.4: Comparison of measured $\delta I/I$ values (filled circles) to those predicted by Eq. 2.8 (dashed line) and Eq. 2.11 (dotted line). The measured data were taken over several runs on a single PL-defined pore of length $10.6 \mu\text{m}$ and cross-section $1.04 \mu\text{m}^2$.

pulse height on particle size in the large and small sphere limit.

4.5 Summary

In this chapter, I have shown our measurements on polydisperse colloidal solutions using etched quartz devices. These devices are easily able to distinguish colloids separated in diameter by only 40 nm. The measured resistance changes follow the large- and small-sphere limits predicted in Chapter 2. In the next chapter, I will discuss the effects of off-axis particles on the measured pulse heights and widths.

Effects of Off-axis Particles

5.1 Introduction

Spherical particles moving through the pore of a resistive pulse sensor can travel at any radial position relative to the pore axis up until the sphere contacts the pore wall. As described in Chapter 2, off-axis particles will cause a larger resistance change than identically sized on-axis particles. The transit times of off-axis particles are also modified in a manner dependent on the method (fluid flow or electrophoresis) used to drive the particles through the pore. We have found it possible to increase the resolution of our device by accounting for these off-axis effects, but only when using fluid flow (and not electrophoresis) as the force driving the particles. As we shall see, this is due to the differing effects on the transit times of the two types of forces.

5.2 Experimental details

Both types of devices (etched quartz and embedded PDMS) are used to acquire the data presented in this chapter. Polydisperse latex colloidal solutions are measured with etched quartz devices utilizing electrophoretic flow, and with embedded PDMS devices utilizing fluid flow. The colloids used for the electrophoretic experiments are carboxyl-modified, and thus carry a high electric charge; those used for the fluid flow experiments were of mixed surface chemistry.

5.3 Discussion

In Chapter 2, I presented equations illustrating the expected effect of off-axis particles on both the transit time and electrical resistance change as a function of the off-axis coordinate b (see Fig. 2.1 for variable definitions). However, in an experiment, it is impossible to use b as a free variable; the only measured variables are the height $\Delta R/R$ and width t (transit time) of a pulse. The signature of off-axis effects in the experimental data can only be seen in plots of $\Delta R/R$ vs. t , so the theoretical predictions must be presented in this manner as well.

Fig. 5.1 shows the theoretical predictions of Chapter 2 for the relation between the resistance change $\Delta R/R$ and transit time t of off-axis particles of several different diameters; each curve has been normalized by its on-axis values ΔR_o and t_o . These curves are found by first separately determining $\frac{\Delta R}{R}(b)$ and $t(b)$, then plotting the results against each other. Fig. 5.1A shows the predicted relation when using fluid flow; here Eq. 2.13 is used to find $\frac{\Delta R}{R}(b)$, and Eq. 2.24 is used to find $t(b) = L/v_p(b)$ (where L is the pore length, and v_p is the particle velocity). Fig. 5.1B shows the predicted relation when using electrophoresis; here Eq. 2.13 is again used to find $\frac{\Delta R}{R}(b)$, while the numerical results of Higdon and Muldowney [34] (see Fig. 2.4) are used to find $t(b)$. In both plots, each curve is drawn up to the maximum off-axis coordinate allowed by the radii of the pore R and sphere a : $b_{max} = R - a$. This finite size effect is why the curves for the larger spheres are significantly shorter than those for the smaller spheres.

We can immediately draw two important conclusions from Fig. 5.1. First, the effect of off-axis particles is much simpler in the case of fluid flow, where a positive correlation between $\Delta R/R$ and t is seen for all particle sizes, than it is for electrophoresis, where the nature of the drag on off-axis particles (see Fig. 2.4) leads to a significantly different correlation for different particle sizes. Second, the off-axis effect on the transit time is much stronger when utilizing fluid flow; for example, for $a/R = 0.1$ the transit time varies by over a factor of five for fluid flow, but by less

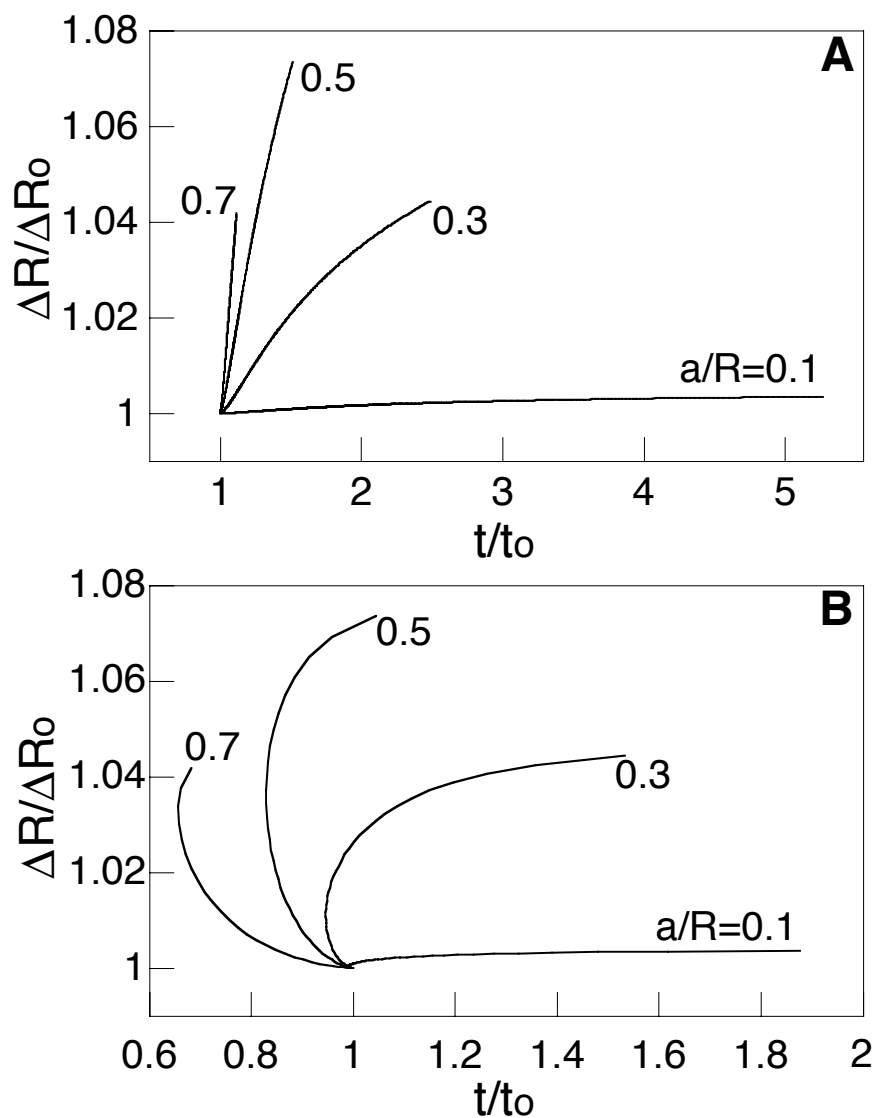


Figure 5.1: Theoretical predictions of $\Delta R/\Delta R_0$ vs. t/t_0 for off-axis particles driven by **A** fluid flow and **B** electrophoresis for particles of relative sizes $a/R = 0.1, 0.3, 0.5, 0.7$. ΔR_0 and t_0 represent the on-axis resistance change and transit time; thus the point $(1, 1)$ on each plot represents the height and width of a pulse caused by an on-axis particle, and the curve that radiates outward from that point represents the pulses caused by particles traveling successively further off of the pore axis.

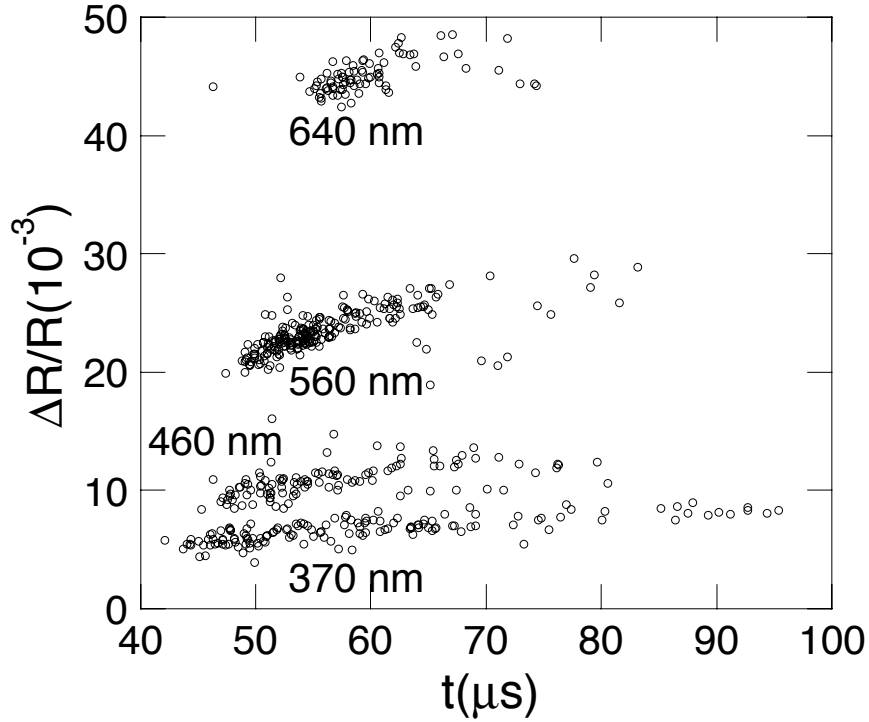


Figure 5.2: Measurements of $\Delta R/R$ vs. t taken with an embedded PDMS device utilizing fluid flow (5 psi applied) to drive colloids of four different sizes (diameters as labeled) through the pore. Each point represents the height and width of a single pulse; each cluster of points is due to a given population of colloids.

than a factor of two for electrophoresis. Based on these conclusions, we expect off-axis particles to have a relatively simple and strong effect on data taken when using fluid flow as compared to those taken using electrophoresis.

Fig. 5.2 shows measured values of the relation between $\Delta R/R$ and t for colloids of diameters 370 nm, 460 nm, 560 nm, and 640 nm. The colloids were driven by fluid flow through an embedded PDMS pore $7.0 \mu\text{m}$ in length and $0.9 \mu\text{m}$ in diameter. The relative size of each type of colloid is then, in ascending order, $a/R = 0.41, 0.51, 0.62, 0.71$. Several things are apparent in this plot. First, the data points for colloids of a given size cluster together since they cause similar resistance changes and transit times.

Second, the range of transit times for a given colloid population decreases as the particles get larger; this is simply due to the finite-size effect. Third, there is a clear positive correlation between the pulse heights and widths, as predicted by the theory for fluid flow. Fourth, the correlation between $\Delta R/R$ and t gets larger for larger particles; again, this is also clear in the predicted curves of Fig. 5.1(a). Finally, for each type of colloid, the minimum transit time is fairly well-defined, while the maximum is not. The minimum transit time corresponds to on-axis particles, while the maximum corresponds to particles traveling near the pore wall. We attribute the undefined nature of the maximum to adhesion events in which particles temporarily stick to the pore wall. The effect of adhesion events will be to spread out the cluster of events for a given population in the direction of increasing transit time.

Figure 5.3 compares the off-axis effects of particles driven by fluid flow with those driven by electrophoresis, and also compares each to the theory illustrated in Fig. 5.1. Part **A** of the figure shows data taken on colloids of diameters 470 nm and 514 nm using fluid flow with an embedded PDMS device, while part **B** shows data taken on colloids of diameters 500 nm and 560 nm using electrophoresis with an etched quartz device.

The predicted curves in each part of Fig. 5.3 are found by determining the minimum transit time and minimum resistance change, then adjusting the equations used to generate Fig. 5.1 so that they share those minima. This is rather straight forward for the case of fluid flow, since the minima are fairly well defined. The minima are not well defined for the electrophoresis data, so here the placement of the theory curve is somewhat arbitrary; however, it is still useful to plot the theory curve in order to compare qualitatively the predicted curve with the measurements. It is clear in Fig. 5.3 that the predicted relation between resistance change and transit time quantitatively fits the measurements for the fluid flow data, but does not appear even qualitatively similar for the case of electrophoresis. It is possible that the electrophoresis data follow the predicted curve, but the scatter in the measured points, along with the arc of the predicted curve, makes the comparison very difficult. These observations fit

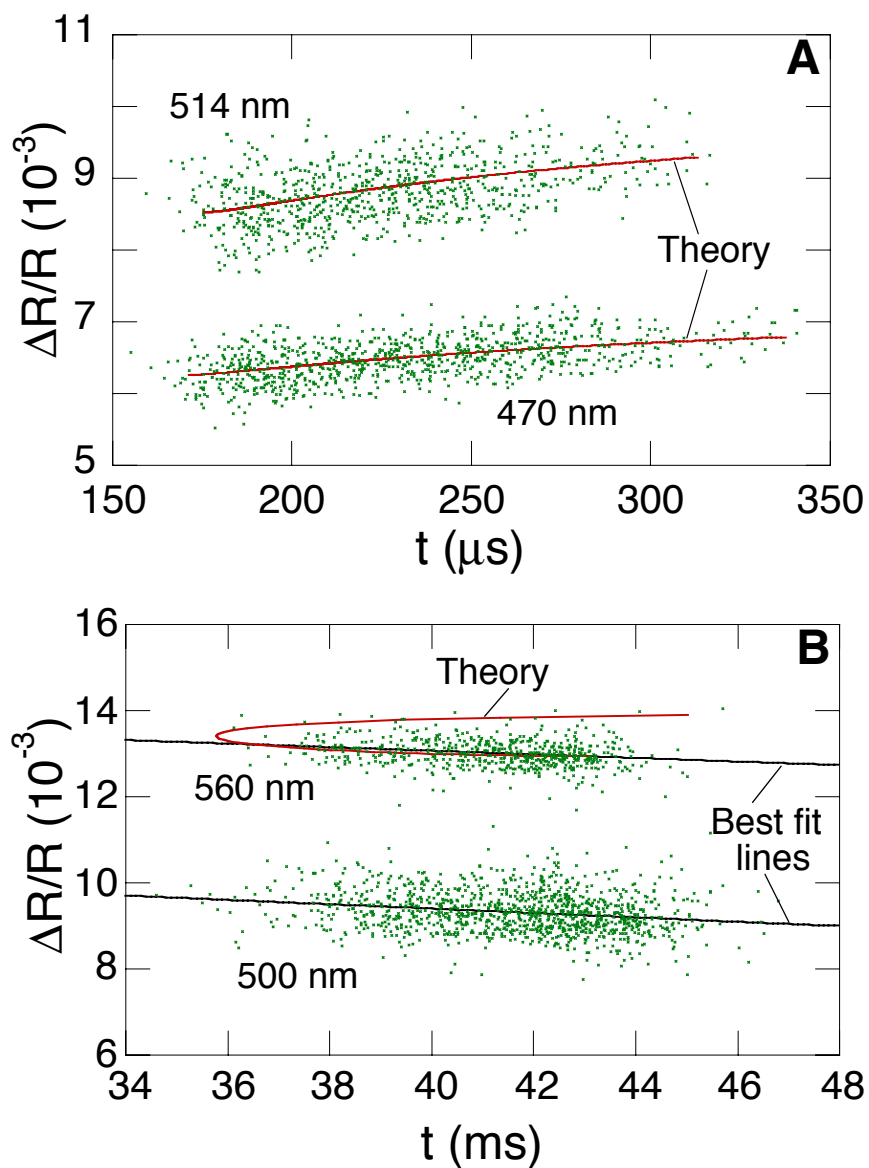


Figure 5.3: Comparison of off-axis effects measured for colloids of labeled diameters driven by **A** fluid flow and **B** electrophoresis. The curves predicted by theory are shown in **A** for both colloids ($a/R = 0.41, 0.45$), and in **B** for the larger colloid that approximates $a/R = 0.5$. Also shown in **B** are best fit lines for each colloid population that accentuate the negative correlation.

with what we expected: the fluid flow data has a strong, simple positive correlation, while the electrophoresis data is more complex.

In Fig. 5.3B, best fit lines are also plotted for each colloid population. The lines accentuate the one clear effect seen in the electrophoresis data: a negative correlation between the measured pulse height and width. This negative correlation is expected for larger particles (see Fig. 5.1), and is due to the fact that the hydrodynamic drag on the particles initially decreases with off-axis coordinate (as shown in Fig. 2.4). The drag on smaller particles greatly increases with larger off-axis coordinate, so the curve in Fig. 5.1 for $a/R = 0.1$ mainly indicates a positive correlation. Larger particles cannot access such large values of off-axis coordinate, so the curve for those particles in Fig. 5.1 reflects the initial decrease in drag followed by a smaller increase. This small increase in drag is not clear in our data. However, it is probable that the measured negative correlation is due to the initial decrease in drag.

An alternate interpretation of the positive correlation seen in Fig. 5.3(a) is that it is due to deviations in the size of individual colloids within each population, since it is clear that relatively larger colloids will both move slower and produce larger pulse amplitudes. The 470 nm diameter colloid population shown in the lower portion of the data plotted in Fig. 5.3(a) has a standard deviation of 12 nm as measured by the manufacturer. Eq. 2.24 predicts that the expected variation in t of on-axis particles, due solely to differences in particle size within the population, will be $\sim 2\%$. As seen in Fig. 5.3(a), the measured values for t vary by much more than that ($\sim 80\%$). We thus conclude that the measured variations in t can be attributed almost entirely to off-axis effects and not to differences in particle size.

The relatively simple nature of the off-axis effects seen when using fluid flow leads us to propose a method for removing them during analysis of the data. As shown in Fig. 5.3, the correlation between ΔR and t is nearly linear. We propose that the off-axis effects can be effectively removed from the data by fitting a line $f(t)$ to the plot of ΔR vs. t for each colloid population, and then calculating an adjusted value

ΔR_{adj} for each pulse of height ΔR and width t through

$$\Delta R_{adj} = \Delta R - [f(t) - f(t_{min})], \quad (5.1)$$

where t_{min} is the minimum transit time measured. We thus use Eq. 5.1 to calculate the pulse height each colloid would have caused had it traveled on the pore axis. It is impossible to develop such an algorithm for the electrophoretic case because of the complex nature of the drag on off-axis particles. The roughly parabolic nature of the drag on off-axis particles in fluid flow causes the transit times to have a one-to-one correspondence with the off-axis coordinates, which consequently allows us to use the measured transit time to remove the off-axis effects through Eq. 5.1. There is no such one-to-one correspondence for the electrophoretic case: it is clear in Fig. 5.1 that, when electrophoretically driven, intermediate sphere sizes will have equivalent transit times at two different off-axis coordinates.

To illustrate the increase in resolution that results from employing Eq. 5.1, we have applied the algorithm to the measurements of a polydisperse solution of colloids shown in Fig. 5.2. In Fig. 5.4, we plot the distribution of measured $\Delta R/R$ values both before and after applying Eq. 5.1. As shown, the correction clearly sharpens the distribution for each type of colloid. For example, the coefficient of variation (standard deviation divided by mean) for pulses produced by 560 nm diameter colloids is reduced from 7.1% to 3.5%. The adjustment has less of an effect on the largest colloid (640 nm) because of the finite size effects, which limits the severity of the off-axis effect.

5.4 Summary

In this chapter, I have described our results on the effects of off-axis particles on the measured pulse heights and widths, and I have introduced an algorithm to remove those effects when using fluid flow to drive the particles through the pore. Because we are unable to remove the off-axis effect when using electrophoresis, the measured distributions of pulse heights of a given colloid population are reduced in accuracy

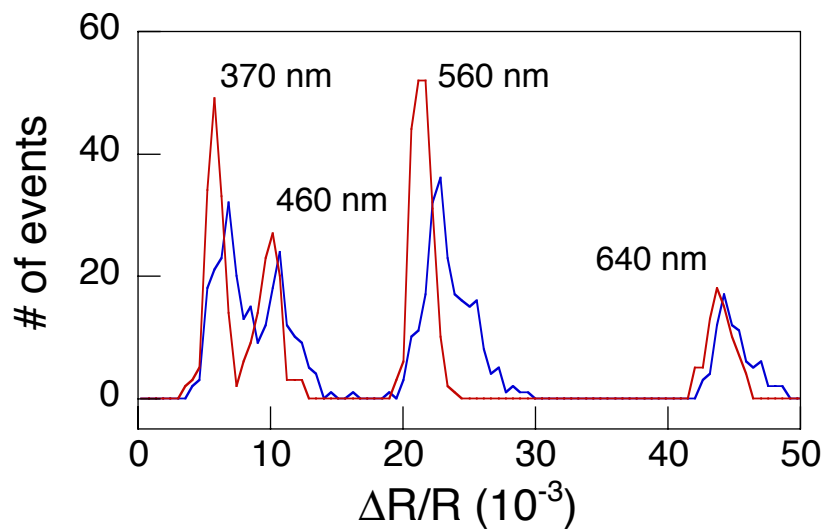


Figure 5.4: Histogram of the normalized pulse heights ($\Delta R/R$) measured for a solution containing four different sizes of latex colloids (of diameters 370 nm, 460 nm, 560 nm and 640 nm as labeled); each peak corresponds to the colloids of a given size. The blue line represents the raw data while the red line shows the same data after correcting for the effects of off-axis particles, as described by Eq. 5.1.

since they contain an intractable systematic source of error: the electrical off-axis effect. Devices using pressure driven flow, where we are able to remove the electrical off-axis effect by applying the correction described in Eq. 5.1, are thus more accurate than those that use electrophoretic flow. This is a general and important result, since it should be true for all resistive pulse sensors, and so should increase the accuracy of their use in the future.

Immunological Sensing

6.1 Introduction

Antibodies can be powerful and flexible tools because of their natural ability to bind to virtually any molecule and because of the modern ability to produce specific types in large quantities. These traits have led to the development of a number of important immunosensing techniques in which antibodies of a desired specificity are used to test for the presence of a given antigen[46, 47, 48, 49]. For example, radioimmunoassays (RIA) have been employed in clinical settings to screen for such viruses as hepatitis[50]. An integral part of all immunosensing technologies is the ability to detect the binding of antibody to antigen. To accomplish this, most common immunoassays require the labeling of the antibody using fluorescence, radioactivity, or enzyme activity. However, the need to bind chemically a label to the antibody adds to the time and cost of developing and employing these technologies.

In this chapter, I describe a novel method we have developed to perform immunoassays with our on-chip resistive pulse sensor. By improving the resolution of our device using the methods described in Chapter 5, we can detect the increase in diameter of a latex colloid upon binding to an unlabeled specific antibody (see Fig. 6.1). We employ this novel technique to perform two important types of immunoassays: an inhibition assay, in which we detect the presence of an antigen by its ability to disrupt the binding of antibody to the colloid; and a sandwich assay, in which we

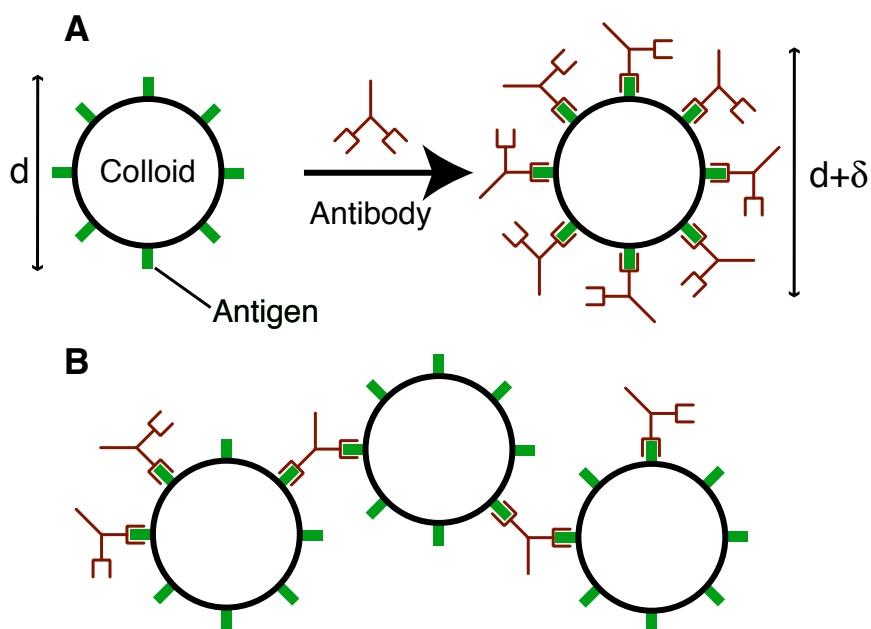


Figure 6.1: Schematic diagrams of the binding of antibody to colloids. **A** shows the strategy we employ to detect the binding of antibody to antigen-coated colloids: the measured colloid diameter increases from d to $d + \delta$ due to the volume added by the bound antibody. **B** illustrates the crosslinking of colloids by antibody to form aggregates, which are unwanted since they can clog the pore. See the text for details on our methods to remove aggregates from the solution.

successively detect the binding of each antibody in a two-site configuration.

Previous particle-counting based immunoassays have used optical scattering or resistive pulse methods to detect the aggregates formed when the antibody crosslinks antigen-coated colloids[51, 9, 10, 11] (see Fig. 6.1). However, relying on crosslinking as a general binding probe is limiting since it requires a free ligand with at least two binding sites. In contrast, our method is more general, since it relies only on the added volume of bound ligand and does not place any limitations on the ligand's functionality. While our device cannot as of yet perform the kinetic analyses that surface plasmon resonance (SPR) techniques[52] are capable of, it represents a rapid, inexpensive and compact alternative to SPR for end-point analysis of biological reactions.

6.2 Experimental details

Embedded PDMS devices are used to acquire all the data presented in this chapter. Typically, these devices have pores 7-9 μm in length, and 0.9-1.2 μm in diameter. Two types of colloids are used in these experiments: an experimental colloid, on which the binding reactions of interest occur, and a reference colloid, which is used to calibrate the device as described in the next section. The experimental particle is a streptavidin-coated latex colloid of mean diameter ~ 510 nm, while the reference particle is a sulfate-coated latex colloid of mean diameter 470 nm. The colloids are mixed in solutions of phosphate buffered saline (PBS; diluted to half the standard concentration) at pH 7.3 containing the surfactants bovine serum albumen (BSA, 0.2 mg/mL) and pluronics F127 (0.05% by volume).

The colloids are driven through the pore using the fluid flow technique described previously (see Fig. 3.5). When applying 1-2 psi, each colloid passes through the pore in a few hundred microseconds; this time is long enough to establish a stable square pulse. The electrical current values are acquired at 50 kHz using a DAQ board; each set of 20,000 data points (representing 0.4 s of data collection) is then saved to a

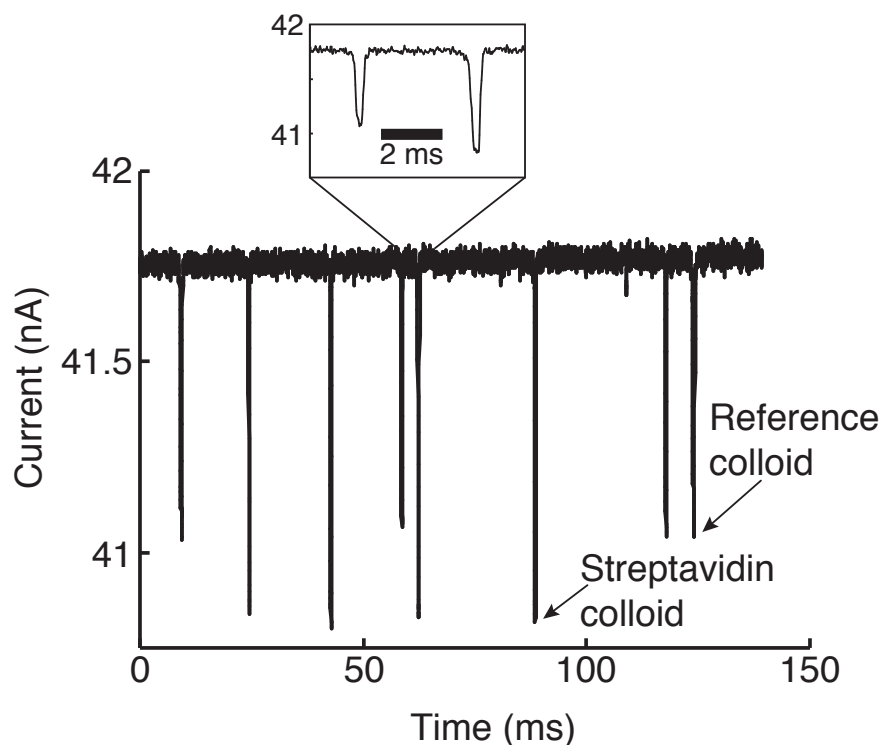


Figure 6.2: Typical current trace showing the passage of both experimental and reference colloids through a pore. The inset magnifies the trace to show the square shape of each pulse. There is a clear difference in the pulse height caused by the two different colloids; this allows us to separate the two populations during the data analysis.

separate file for later analysis. Fig. 6.2 shows a typical current trace that records several colloids passing through the pore; the inset magnifies two pulses to reveal their square shape.

A single experimental run consists of at least several hundred (and frequently over a thousand) of each type of colloid passing through the pore. We use the experimental results from 3-5 different devices to find the mean diameter of a population of colloids suspended in a particular solution. The dominant source of error in our measurements is the intrinsic distribution of the streptavidin colloids' diameter, with

smaller contributions from the spread in diameter of the reference colloids and the electrical noise in the current measurement (which stems mainly from the Johnson noise across the pore).

When we perform binding experiments, we add antibody to a solution containing both colloids and mix by vortexing and/or repetitive micropipette aspiration. This is done no more than 30 minutes prior to a measurement; if mixed too far in advance, the antibody can cause aggregation as illustrated in Fig. 6.1. Even when minimizing the incubation time between mixing and measurement, aggregation can still occur, so steps must be taken to keep aggregates from clogging the pore. Such steps include breaking the aggregates up through sonication and repetitive micropipette aspiration (as described in Section 3.2.1).

As a second safeguard against clogging of the pore, we fabricate filters in the reservoirs of the devices. These filters are a row of channels 100 μm from the pore; each channel has a diameter equal to that of the pore. In this way, any objects larger than the pore diameter (and thus able to clog the pore and end the measurement) will be removed from the solution. If a solution contains many large objects, the filter itself will become completely clogged, and further measurement will be impossible.

Fig. 6.3 shows images of the filter region of a device both before and after a measurement. The filter has 21 channels, each of which consists of two stages: a 5 μm wide, 1 μm deep entrance that narrows to a 1 μm wide, 1 μm deep line. The two-stage design of each filter channel is intended to increase the filter's lifetime by capturing large ($>1 \mu\text{m}$) objects at the entrance of a given channel while still allowing smaller particles to pass around those objects and through that channel.

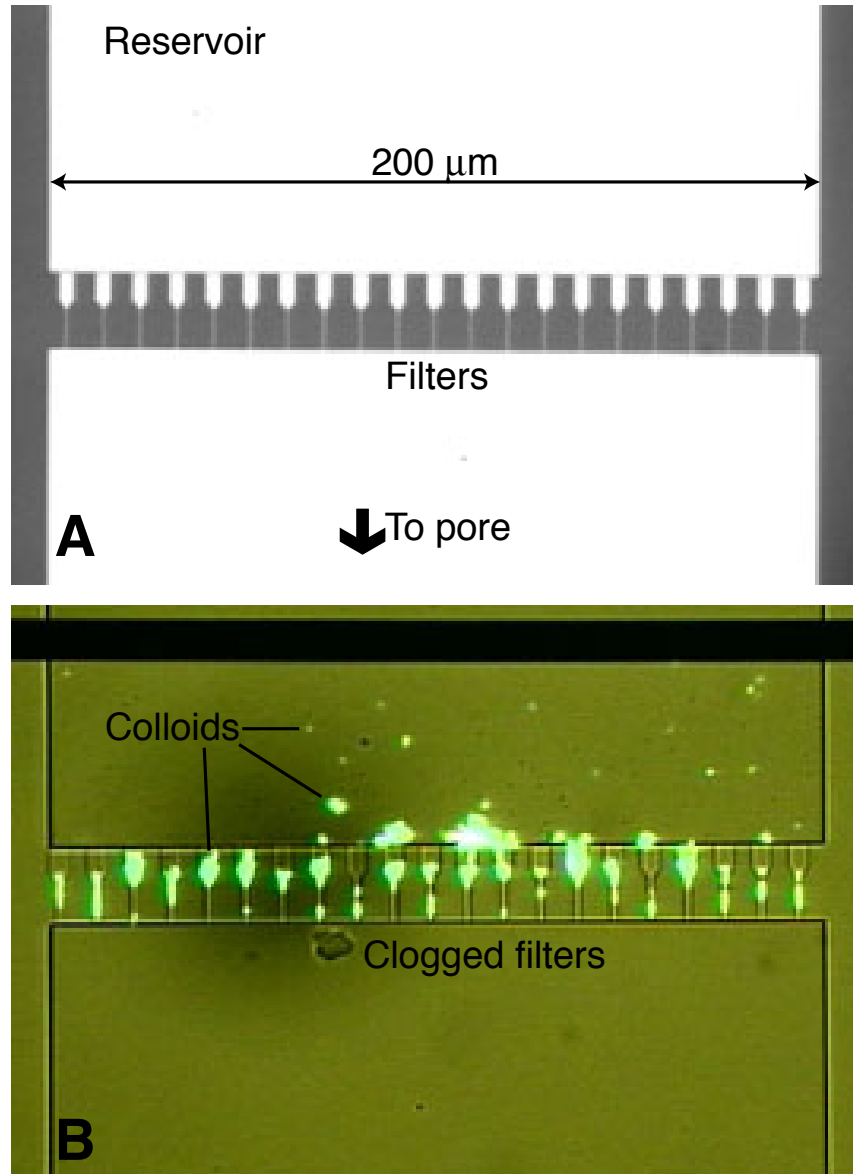


Figure 6.3: Images of the filter region of a device **A** while dry and **B** after clogging by colloids. During a measurement, colloids (the green particles in **B**) enter the $200\ \mu\text{m}$ wide, $7\ \mu\text{m}$ deep reservoir from the top of the image, and go off the bottom of the image towards the pore.

6.3 Data Analysis

6.3.1 Off-axis Effects

The ability of the device to resolve small changes in the diameter of a colloid is limited by the effects of off-axis particles on the change in electrical resistance. These effects are greatly diminished by utilizing the algorithm described in Chapter 5 to adjust the pulse height caused by an off-axis particle. As mentioned, it is necessary to determine the minimum (on-axis) transit time for a given colloid population in order to apply the algorithm. The on-axis transit time is determined by the pressure applied across the pore. However, it is possible for that pressure to vary due to the presence of the filter, thus causing the minimum transit time to fluctuate, and rendering the application of the algorithm impossible.

Pressure variation usually occurs near the end of a device's lifetime, when the filter becomes almost entirely clogged. At this point, the hydrodynamic impedance of the filter becomes comparable to that of the pore, and thus there is a significant increase in the fraction of applied pressure that is dropped across the filter. The corresponding decrease in the pressure dropped across the pore results in a measurable decrease in the transit time of the particles. A typical data run will then consist of a period of time during which the minimum particle transit time is constant, followed by a period during which the minimum transit time increases, and ending with complete clogging of the filter and a lack of events. Thus, the first step in the data analysis (after each pulse's height and width have been measured) is to remove the pulses with increased transit times. This is done rather easily by plotting the pulse width measured for each event against the file number (the 0.4 s interval) during which the event occurred; such a plot is shown in Fig. 6.4. There is a clear increase in the minimum transit time starting at file number 206; thus for this measurement all files beyond number 206 would be discarded. The remaining data represents colloids that traveled through the pore under constant applied pressure. The minimum transit time for each population can then be accurately determined, and the algorithm to remove off-axis effects can

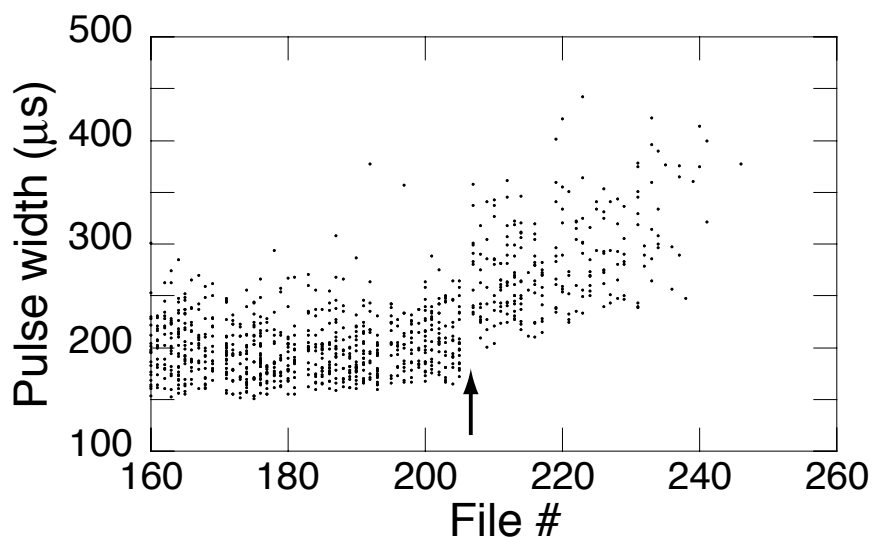


Figure 6.4: Effects of a clogged filter on the measured pulse width during the course of an experiment. Each plotted point represents the pulse width measured for a single colloid passing through the pore during a given data file. Around file number 206 (marked by the arrow), there is a clear increase in the width of the measured pulses. Thus, at that time, the filter became significantly clogged, decreasing the rate of fluid flow through the pore.

be applied.

6.3.2 Calibrating the Pore

As mentioned in Chapter 4, we have found that the equation first derived by Gregg and Steidley[3] (Eq. 2.11) accurately describes the expected resistance change caused by colloids with diameters $a/R \gtrsim 0.4$. Thus we use this equation when attempting to relate the measured pulse heights $\Delta R/R$ to the diameters of the colloids used here. Application of Eq. 2.11 requires knowledge of the pore dimensions. While we can measure the length of each pore under an optical microscope, we cannot do the same to find the diameter. Furthermore, we have found that the size of pores cast into PDMS from the same master can vary (by up to 6% in diameter) between

devices. Thus, we need to calibrate the size of each pore simultaneously with each measurement.

We perform the calibration by adding a reference colloid of known diameter (a 470 nm diameter sulfate-coated latex colloid) to each solution. The absolute difference in diameter (470 nm to 510 nm) between the reference colloid and the experimental colloid results in a clear difference in the pulse heights (see Fig. 6.2). Consequently, we can easily determine which size colloid produced each pulse, and can isolate the pulses caused by each population. We can then numerically invert Eq. 2.11 to find the pore diameter D by using the mean resistance change $\overline{\Delta R/R}_{ref}$ due to the reference colloids, along with the known values of L and d . Note that the mean resistance change for the reference colloids is calculated after performing the off-axis adjustment. The numerically inverted version of Eq. 2.11 is

$$D = 1.9630 - 21.720\alpha + 174.60\alpha^2 - 725.50\alpha^3 + 1216.0\alpha^4 \quad (6.1)$$

where $\alpha = L\overline{\Delta R/R}_{ref}$. The numerical coefficients in Eq. 6.1 are found by fitting a polynomial to a plot of D vs. α , assuming the pulses were due to colloids 470 nm in diameter

6.3.3 Extracting Colloid Diameters

Once we find the pore diameter, we again need to invert Eq. 2.11 in order to relate the pulse heights caused by each experimental colloid to that colloid's diameter. This is done using the equation

$$d = D(0.2636 + 3.579\beta - 17.37\beta^2 + 52.46\beta^3 - 67.45\beta^4) \quad (6.2)$$

where $\beta = L\delta_{exp}/D$, and δ_{exp} represents the normalized pulse height $\Delta R/R$ measured from an experimental colloid. Again, the normalized pulse heights δ_{exp} used in Eq. 6.2 already have been adjusted to remove off-axis effects.

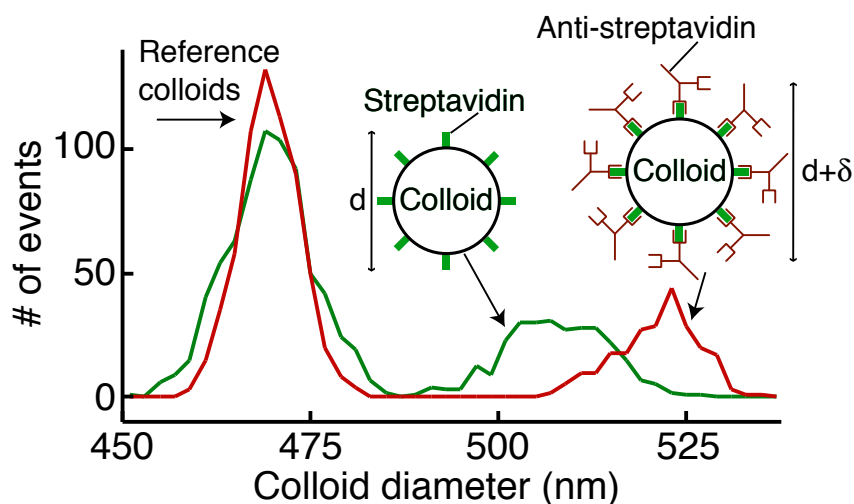


Figure 6.5: A histogram showing the distribution of colloid diameters measured from a solution that contains only the reference and streptavidin colloids (green line), and a solution that contains both types of colloids and 100 $\mu\text{g}/\text{mL}$ of monoclonal anti-streptavidin antibody (red line).

6.4 Results

6.4.1 Simple Binding

Figure 6.5 shows a histogram comparing the distribution of measured colloid diameters obtained from applying the analysis techniques to data from two different solutions: one containing only the streptavidin and the reference colloids, and one containing both types of colloids and 100 $\mu\text{g}/\text{mL}$ of monoclonal mouse anti-streptavidin antibody. As shown, there is a clear increase of 9 nm in the mean diameter of the streptavidin colloids in the solution containing the antibody. We attribute this increase to the volume added to the colloid upon the specific binding to the anti-streptavidin.

It is possible that the measured diameter increase occurs not due to specific chemical recognition of the antigen (the streptavidin immobilized on the colloid) by the antibody, but rather because of non-specific binding. For example, the antibody

might adsorb onto exposed portions of latex on the colloid's surface. To show that the diameter increase is due to specific binding, we perform a control measurement where an antibody from the same source (mouse), but with a different antigen specificity, is added to the solution. We find a much smaller increase in diameter (~ 2.5 nm) when mixing the colloids with $100 \mu\text{g}/\text{mL}$ of a monoclonal isotype matched irrelevant antibody (mouse anti-rabbit; see Fig. 6.6). This smaller increase is a result of non-specific binding of the irrelevant antibody to the streptavidin colloids.

Fig. 6.7 shows the measured change in colloid diameter as the concentration of the specific antibody (monoclonal anti-streptavidin) is varied from $0.1 \mu\text{g}/\text{mL}$ to $100 \mu\text{g}/\text{mL}$. As shown, the colloid diameter reaches its maximum value when the colloids are mixed with $\geq 5 \mu\text{g}/\text{mL}$ of antibody. Using a Bradford protein assay¹[53], we determine the minimum saturating concentration of antibody for the colloid concentration in our experiment (1.2×10^9 particles/mL) to be $3.5 \mu\text{g}/\text{mL}$, which is in good agreement with the results of our electronic pore-based immunoassay. Furthermore, the manufacturer-quoted binding capacity of the colloids indicates that each colloid has approximately 9800 streptavidin molecules on its surface. If each colloid binds to an equivalent number of antibodies, the minimum saturating concentration for a solution containing 1.2×10^9 colloids/mL will be $\sim 3.0 \mu\text{g}/\text{mL}$; again, this is in good agreement with our results. As shown in Fig. 6.7, the dynamic range of our assay corresponds to antibody concentrations from $0.5 \mu\text{g}/\text{mL}$ to the saturating concentration of $\sim 5 \mu\text{g}/\text{mL}$. By decreasing the colloid concentration, we can decrease the binding capacity of the solution, thus decreasing the saturating concentration of antibody. In this manner, we can expect the range of sensitivity of the device to decrease to antibody concentrations as low as 10-50 ng/mL.

¹The Bradford assay is based on the colorimetric reaction between proteins and the dye Coomassie Brilliant Blue G-250. The protein-dye complex strongly absorbs 595 nm light; thus the absorption at 595 nm of a solution of a protein and the dye will be sensitive to the concentration of protein. Measurement of the binding capacity of the colloids is done by mixing solutions of known antibody concentration and known colloid concentration, allowing binding to occur, then centrifuging to remove the colloids (along with all the antibody that was bound by the colloids). The difference between the known initial antibody concentration and the antibody concentration in the supernatant of the colloid mixture is equal to the amount of antibody bound by the colloids.

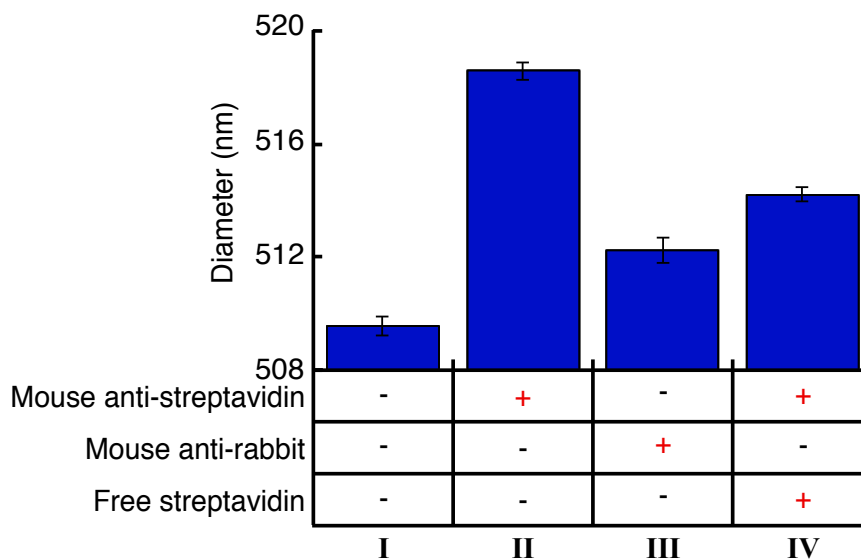


Figure 6.6: A summary of the measurements of the mean diameter of the streptavidin colloids when mixed in different solutions. The presence of additional components in each solution is indicated by a ‘+’ in the column beneath the plotted bar. Column I shows the mean diameter measured without any protein added to the solution. A 9 nm increase in colloid diameter is seen in the presence of the specific antibody to streptavidin (100 $\mu\text{g}/\text{mL}$ mouse anti-streptavidin, column II); we attribute this to the volume added to the colloid due to the specific binding of the antibody. The specificity of the probe is shown by the lack of a significant diameter increase in the presence of isotype matched irrelevant antibody (100 $\mu\text{g}/\text{mL}$ mouse anti-rabbit, column III); the small diameter increase in this solution can be attributed to non-specific adhesion. We also perform an inhibition assay, where the specific binding of the anti-streptavidin to the colloid is disrupted by the presence of 200 $\mu\text{g}/\text{mL}$ free streptavidin (column IV)— the presence of free antigen is shown by the decrease in diameter compared with the antigen-free solution (column II). All error bars represent one standard deviation of uncertainty in determining the colloids’ mean diameter.

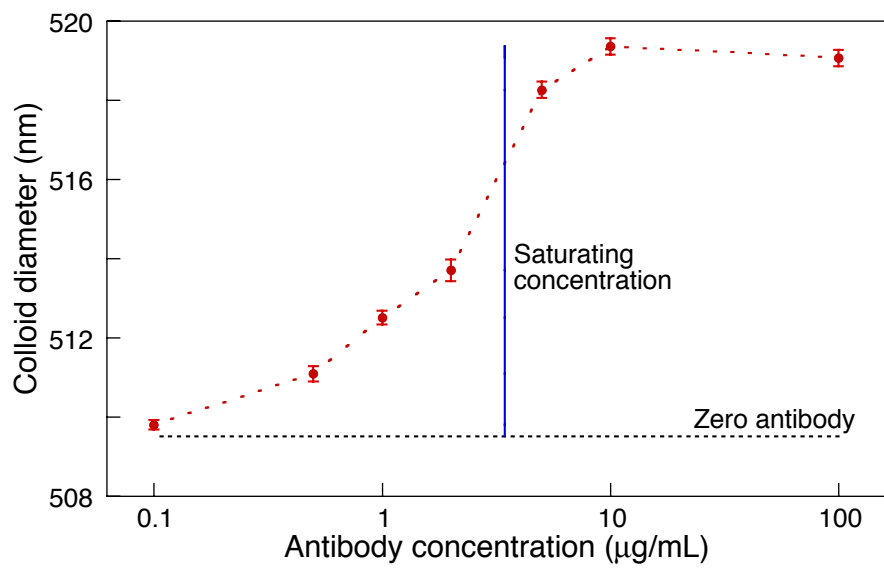


Figure 6.7: Measurements of the mean colloid diameter when mixed in solutions of varying monoclonal mouse anti-streptavidin concentrations. The vertical line marks the binding capacity of the colloids as determined by a Bradford protein assay. The diameter of the colloids in the absence of antibody is shown as the black dashed line.

6.4.2 Inhibition Assay

We use our technique's ability to detect successfully the specific binding of unlabeled antibodies to the colloids to perform an inhibition immunoassay. We measure a 4.5 nm increase (see Fig. 6.6) in the diameter of the streptavidin colloids when mixed with 100 $\mu\text{g}/\text{mL}$ anti-streptavidin that had been preincubated with 200 $\mu\text{g}/\text{mL}$ of free streptavidin. This smaller increase (relative to the solution containing only anti-streptavidin) indicates a decrease in the number of antibodies binding to each colloid. We attribute this to the blocking of the antibody binding sites by the free streptavidin. The measured diameter of the streptavidin-coated colloid therefore indicates the presence of free streptavidin in the solution. In general, this inhibition method can be extended to detect any antigen that can be immobilized on the colloid surface.

The 4.5 nm increase seen in column IV of Fig. 6.6 shows that some binding of antibody to the colloid does in fact occur. Based on the control measurement with an irrelevant antibody (column III of Fig. 6.6), we attribute this increase to a combination of non-specific binding of blocked antibodies, and incomplete inhibition of the antibody by the free streptavidin. The possibility of non-specific binding does decrease the dynamic range of the measurement. However, because of the very small uncertainty in the measured mean colloid diameter, the dynamic range necessary to determine the amount of ligand bound to the colloid is still quite substantial.

6.4.3 Sandwich Assay

As a second demonstration of our technique's sensitivity to the volume added by molecules bound to a streptavidin colloid, we perform an immunoassay using a sandwich configuration. Here, a primary antibody that is immobilized on the colloid surface binds to a free antigen, which in turn is bound to a secondary antibody; a schematic of the binding arrangement is shown in Fig. 6.8. We immobilize the primary antibody by mixing streptavidin colloids with a biotinylated antibody to thus create a colloid-antibody conjugate through the streptavidin-biotin bond. We use the

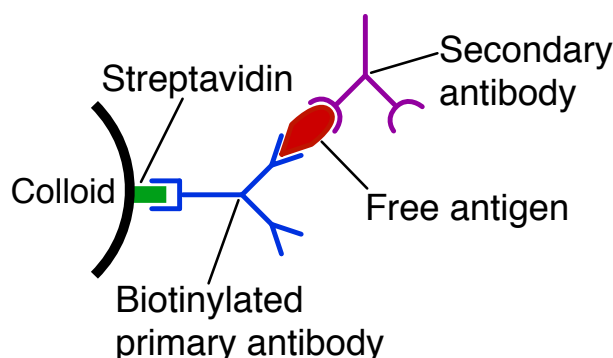


Figure 6.8: Schematic of the sandwich, or two-site, binding configuration, where the primary and secondary antibodies both bind to the free antigen. The primary antibody is attached to the colloid through a biotin-streptavidin bond.

sandwich assay to detect the presence of an antigen that is found in the cell wall of the bacteria *Streptococcus* Group A (Strep A), a very common infectious bacteria that causes, among other things, strep throat.

The results of the measurements utilizing the sandwich configuration are shown in Fig. 6.9, which shows the measured diameter of the streptavidin-coated colloids when mixed in different solutions. We find that the colloids, originally ~ 509 nm in diameter (column I of Fig. 6.9), increase in size by ~ 5 nm to 514 nm when conjugated with biotinylated rabbit anti-Strep A (column II). Next, we mix the colloid-antibody conjugates with both the specific antigen to the primary antibody (extract from a culture of Strep A), and $100 \mu\text{g}/\text{mL}$ of a secondary antibody (unlabeled rabbit anti-Strep A). Measurements of this solution show the colloids further increase in diameter by 1.6 nm (column III). This 1.6 nm increase is not seen when the colloids are mixed with the antigen alone (column V), indicating that the binding of the secondary antibody is the principal reason for the diameter increase.

The specificity of the configuration is shown by the lack of an increase in diameter when adding extract from a culture of *Streptococcus* Group B (Strep B, which is not

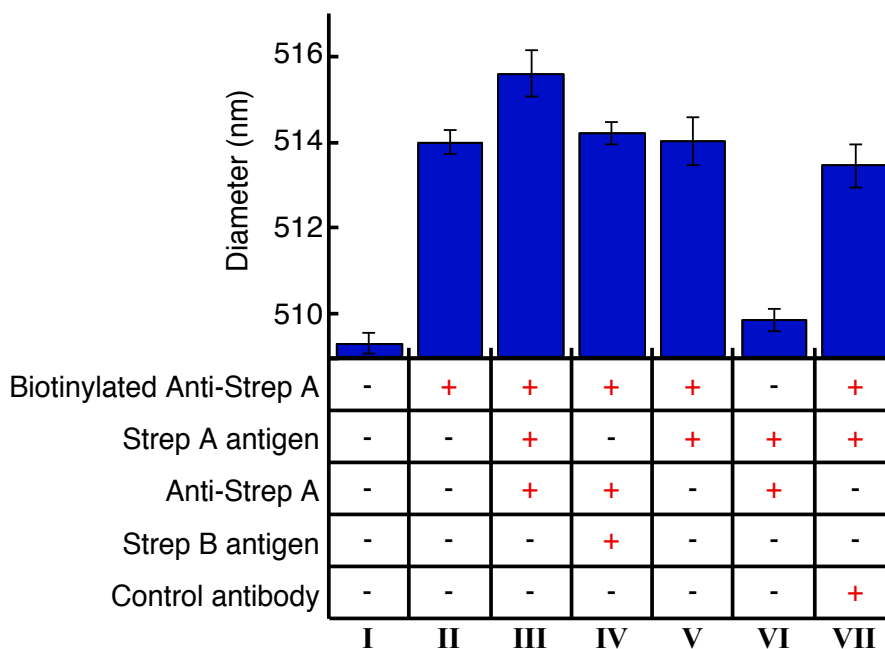


Figure 6.9: Summary of the mean colloid diameters measured when forming an antibody-antigen-antibody ‘sandwich’ on the colloid surface. Along with the colloids, each solution contains additional components as indicated by the ‘+’ in the column below the plotted bar. See the text for details.

bound by either antibody) in place of the Group A extract (column IV), or an irrelevant antibody in place of the specific secondary antibody (column VII). Furthermore, we measure no significant diameter increase when adding the specific antigen and secondary antibody to unconjugated colloids (column VI), indicating that non-specific adhesion of antigen-secondary antibody complexes are not the cause of the diameter increase seen in column III.

It is intriguing that the measured 5 nm increase after attachment of the biotinylated antibody is less than the maximum 9 nm increase seen when utilizing the antibody-antigen bond (Fig. 6.6 and 6.9) to attach antibody to the colloid. This surprising difference is most likely due to the differing conformations of the antibody in each case (the binding sites of the antibody face the colloid in one case, and the

solution in the other); however, further work is needed to clarify this. Nonetheless, despite the smaller size increase, the ability of the device to perform the sandwich assay is still clearly demonstrated.

6.5 Discussion

While we have used an antibody/antigen reaction to demonstrate the power of our technique, we emphasize that its true strength is its generality: it does not rely on any functional properties of the free ligand. Thus, it can be applied to any ligand/receptor pair, provided the free ligand is large enough to produce a discernible change in the size of the colloid.

Future work on the device will focus on optimizing its sensitivity in terms of both ligand size (mass) and concentration. The sensitivity is dependent on four factors: the amount of ligand bound to each colloid, the intrinsic dispersion in colloid size, the colloid geometry, and the colloid concentration. First, increasing the number of binding sites will lead to more ligands bound per colloid, and consequently a larger change in size. For the colloids used here, the parking area for each binding site is ~ 80 nm²; while this is close to the steric limit for antibody molecules, the use of a smaller ligand would permit more binding sites per colloid. Second, the intrinsic spread in the sizes of the streptavidin colloids is the largest source of error in our measurement. The device's sensitivity would be enhanced by using a more monodisperse population of colloids (one with a coefficient of variation in diameter of less than 2%), or even a solution of highly monodisperse nanocrystals[54]. Third, at constant binding density, the measured change in pulse height upon binding to free ligand is proportional to the surface-to-volume ratio of the colloid. Thus, we could increase the sensitivity and dynamic range of the assay by employing a smaller colloid. For example, we estimate that using a colloid 250 nm in diameter would increase the sensitivity of the assay by a factor of four in either ligand size or concentration. Thus, based on the data shown in Fig. 6.7, using a 250 nm colloid at the same particle concentration employed

in this paper would make the assay sensitive to either 38 kDa ligand molecules at concentrations of $0.5 \mu\text{g}/\text{mL}$, or antibody concentrations near $0.1 \mu\text{g}/\text{mL}$. We mention that an even more effective strategy to increase the surface-to-volume ratio would be to use a non-spherical or porous colloid (assuming the pore size is large enough to admit the free ligand) as the substrate for the immobilized receptor. Fourth, as previously mentioned, decreasing the concentration of colloids would further increase the sensitivity since it would decrease the minimum saturating concentration of free ligand. Overall, a combination of these four strategies should result in the increased sensitivity of our assay to ligand concentrations at or below $1 \text{ ng}/\text{mL}$.

6.6 Summary

In conclusion, we have demonstrated our ability to use a resistive pulse measurement to detect the binding of unlabeled antibodies to the surface of latex colloids. This ability is generally applicable to determining rapidly and precisely the thickness of a layer of any kind of biological macromolecule bound to a colloid. Here, we specifically showed that our technique can be employed to perform two widely used and important immunoassays— an inhibition assay and sandwich assay— in which either the antigen or antibody is immobilized on the colloid. In contrast to how these assays are performed today, ours requires no labeling of analytes, uses only sub-microliter volumes of sample and can be performed rapidly and inexpensively. Overall, our device can be used to detect many different kinds of analytes, since the colloids can be easily modified to have almost any specificity (through, for example, the biotin-streptavidin interaction used here). Furthermore, our technique can be extended to multi-analyte detection not only by utilizing several microparticles with different chemical sensitivities and different mean diameters but also by employing devices consisting of arrays of pores[55]; this will be discussed further in Chapter 8. Finally, in addition to a host of biosensing applications, this technique can be used as a diagnostic test of the surface chemistry of colloids.

Sensing Single DNA Molecules

7.1 Introduction

A recent major advance in resistive pulse sensing is the fabrication and use of nanoscale pores to detect the presence of single molecules. This was initially (and still most commonly) done by suspending ion-channel proteins in lipid bilayers[56, 12, 18, 16, 57, 17, 14, 13, 15, 58], but a variety of solid-state fabrication methods[59, 19, 21, 22, 20] have also been used, as reviewed in Chapter 1. However, further development of these strategies is impeded by several technological barriers: the instability of the lipid bilayer used with the protein pores leads to rapid device degradation, and the membrane used to separate the reservoirs in the solid-state methods is extraordinarily fragile and prone to cracking.

In this chapter I report on the application of our fabrication strategy (as described in Chapter 3) to create pores that can detect single lambda-phage DNA molecules. The principal advantage of our device is its robustness. The fragility of other solid-state resistive pulse sensors is due to the extraordinarily thin membrane that holds the pore; our device has no such membrane, relying instead on patterning lateral features on the surface of a substrate. With future improvements, our device should provide many opportunities for single-molecule detection applications.

7.2 Experimental details

Figure 7.1 shows a schematic of a typical embedded PDMS device containing a pore of length $3\ \mu\text{m}$ and diameter $200\ \text{nm}$ connecting two $5\ \mu\text{m}$ deep reservoirs. Devices are fabricated as described in Chapter 3; the main difference between the fabrication of these devices and the larger ones used in previous chapters is the use of electron-beam lithography to define the pore. Because PDMS is a soft material, it is unable to maintain features $\lesssim 150\ \text{nm}$ [43]; however, we have confirmed via atomic force microscopy that we are able to construct well-defined channels with diameters $\geq 200\ \text{nm}$ (see Fig. 7.2).

DNA molecules in the solution are driven through the pore electrophoretically. While it is possible to apply a pressure to one of the reservoirs to drive the molecules through (as was done with the latex colloids in previous chapters; see Fig. 3.5), we have found that less clogs form when using electrophoresis. This occurs because unwanted particles in the solution are generally not very highly charged; thus, they will only move (and clog the pore) when driven with fluid flow. Fluid flow could be used if filters were constructed in the reservoirs (as described in Chapter 6); however, the additional fabrication steps required to construct filters are superfluous because of the ease of utilizing electrophoresis on the highly-charged DNA molecules.

As with the other experiments described in this thesis, sensing is accomplished via a four-point measurement of the electric current through the pore. The current is low-pass filtered below $0.3\ \text{ms}$ in rise time, and is sampled at $1\ \text{kHz}$ using a voltmeter.

7.3 Results

To demonstrate the sensing capabilities of our nanopore, we have measured solutions of $2.5\ \mu\text{g}/\text{mL}$ lambda-phage DNA in a $0.1\ \text{M}$ KCl, $2\ \text{mM}$ Tris (pH 8.4) buffer. Typical traces of measured current are shown in Fig. 7.3. The striking downward peaks, of height $10\text{-}30\ \text{pA}$ and width $2\text{-}10\ \text{ms}$, correspond to individual molecules of DNA

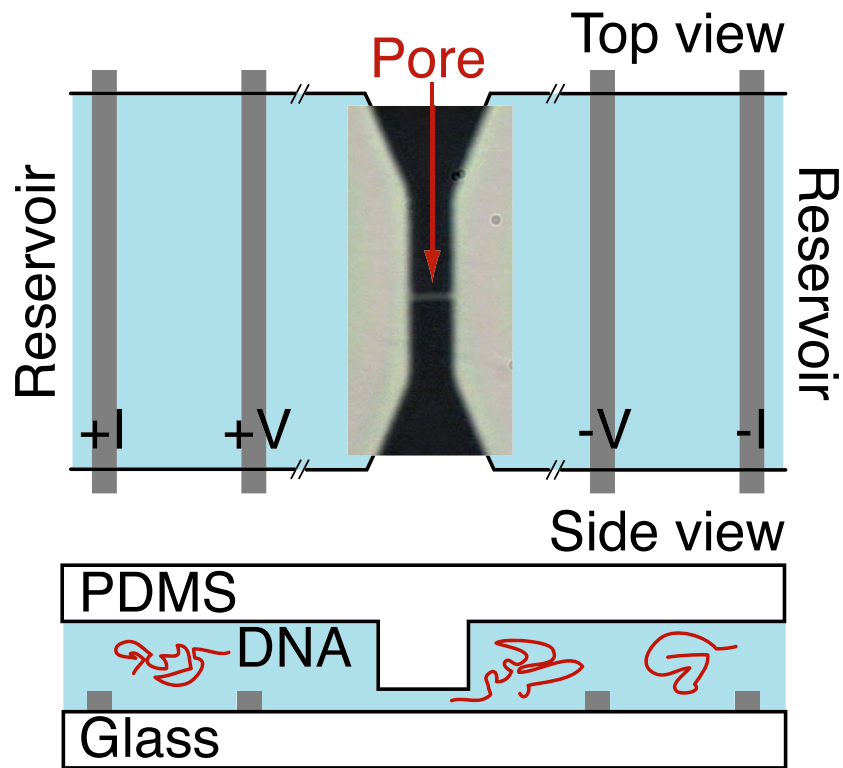


Figure 7.1: Schematic top and side views of our nanopore device which consists of two $5\ \mu\text{m}$ deep reservoirs connected by a lateral pore $3\ \mu\text{m}$ in length and $200\ \text{nm}$ in diameter; an optical image of an actual pore sealed to a glass coverslip is incorporated into the top view.

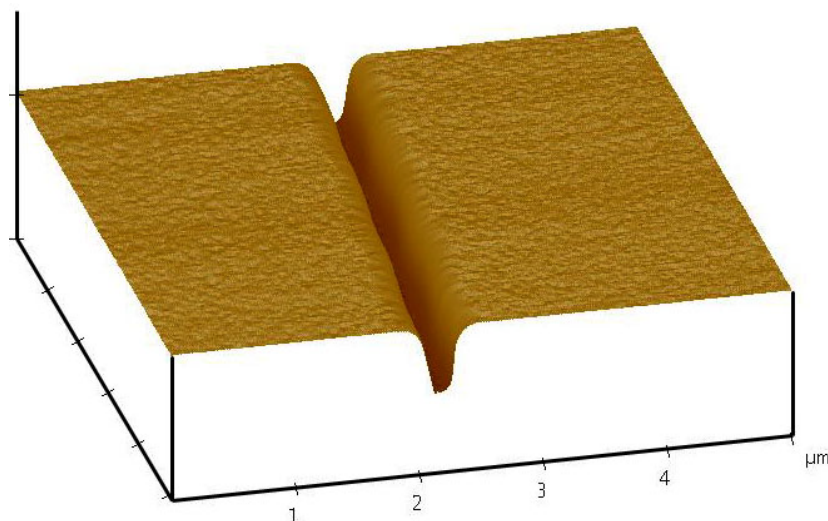


Figure 7.2: AFM image of a 200 nm pore embedded into PDMS.

passing through the pore. In contrast, such peaks are absent when measuring only buffer. We measure peaks only when using pores with diameters of 300 nm or less¹.

7.4 Discussion

Our previous work on colloids has shown that, for particles of diameter much smaller than that of the pore, the ratio of peak height to baseline current is approximately equal to the volume ratio of particle to pore: $\Delta I/I \sim V_{particle}/V_{pore}$. We can estimate the volume of a single lambda DNA molecule by approximating it as a cylinder with a 2 nm radius (which includes a 1 nm ionic, or Debye, layer²), and a height equal to the

¹As mentioned previously, pores cast from the same master will vary in size when sealed due to deformations of the PDMS. In this experiment, the pore cross-section A is estimated by measuring the electric resistance R and length L of the pore, along with the resistivity of the solution ρ through $A = \rho L/R$.

²The Debye length λ_D represents the screening length of electrostatic interactions in a solution. For a solution containing a monovalent salt, λ_D depends on the salt concentration η , the electronic charge e , the temperature T , and the solution's dielectric constant ϵ through $\lambda_D^2 = \epsilon k_B T / 2e^2 \eta$, where k_B is Boltzmann's constant.

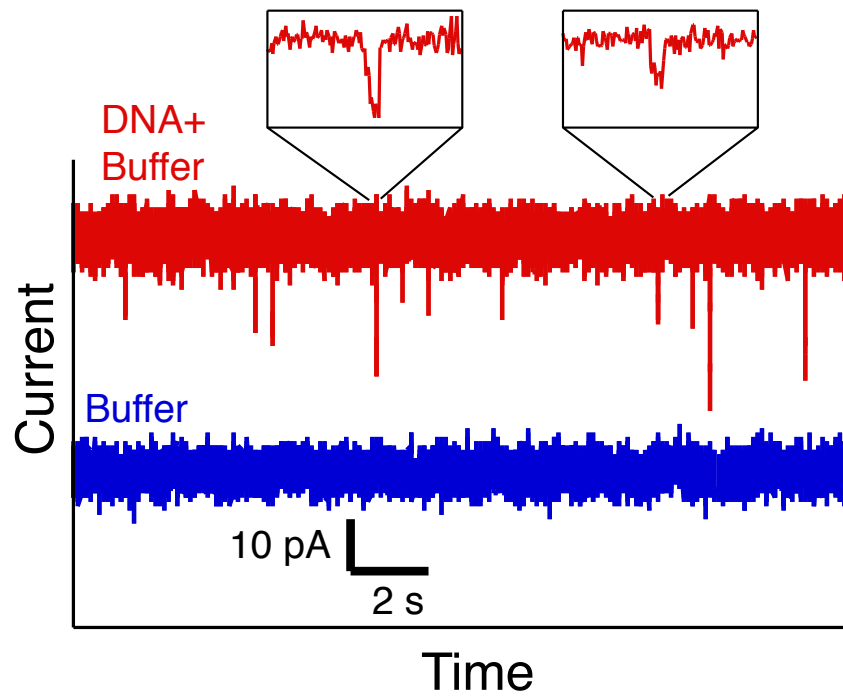


Figure 7.3: Typical traces of current vs. time for solutions of buffer (blue trace), and buffer with lambda phage DNA molecules (red trace), when 0.4 V is applied across the pore. The traces are offset for clarity; the total current in each case is ~ 15 nA. Each downward spike in the red trace represents a single DNA molecule passing through the pore. The spikes are typically 2-10 ms in duration, and are well resolved, as shown in the insets.

contour length of the molecule ($16 \mu\text{m}$). Given the known pore volume and a total current $I=15 \text{ nA}$, we can expect a decrease in current $\Delta I \sim 30 \text{ pA}$ when a lambda DNA molecule fully inhabits the pore. This estimate agrees well with the upper range of measured peak heights. Further corroboration for this model comes from the observation that no peaks are measured when using larger pores. When a molecule inhabits a pore with a diameter $> 300 \text{ nm}$, the expected response in current is less than 40 % of the expected response for a 200 nm diameter pore. This means that, at 15 nA total current, the maximum peak heights for a lambda DNA molecule will be less than 12 pA, and thus the peaks will not be well resolved above the noise. These results suggest that the measured variation in ΔI (from 10-30 pA) is most likely due to differences in molecular conformation: maximum peak heights arise when an entire molecule inhabits the pore, while smaller peak heights occur when only a portion of a molecule resides within the pore. Thus, through control of the conformation of the molecule, the peak height can be related to the DNA length.

We have attempted two different methods to control the DNA conformation. First, we fabricated a small array of posts onto the pore entrance (see Fig. 7.4). The array was designed with a pitch of $\sim 1 \mu\text{m}$, and a post width of $\sim 500 \text{ nm}$. The intention of the array was the following: large DNA molecules that approached the array in a random-coil configuration would be caught by the posts, and held until the DNA threaded through the array into the pore. Thus, the DNA molecules would be forced to pass through the pore in a linear manner [60, 61, 62, 63]. However, in practice, we found that the DNA molecules would become irrevocably tangled in the array, clogging the pore entrance and ending the measurement.

The second strategy to control DNA conformation was to condense the DNA from a fluctuating linear polymer into a compact, stable object. This well-known phenomenon [64, 65, 66, 67, 68, 69, 70] occurs when multivalent cations added to a solution of DNA screen the normal electrostatic repulsion of DNA segments, and cause both the collapse of single large molecules into small toroidal objects and the aggregation of different molecules (given time for the molecules to diffuse into each

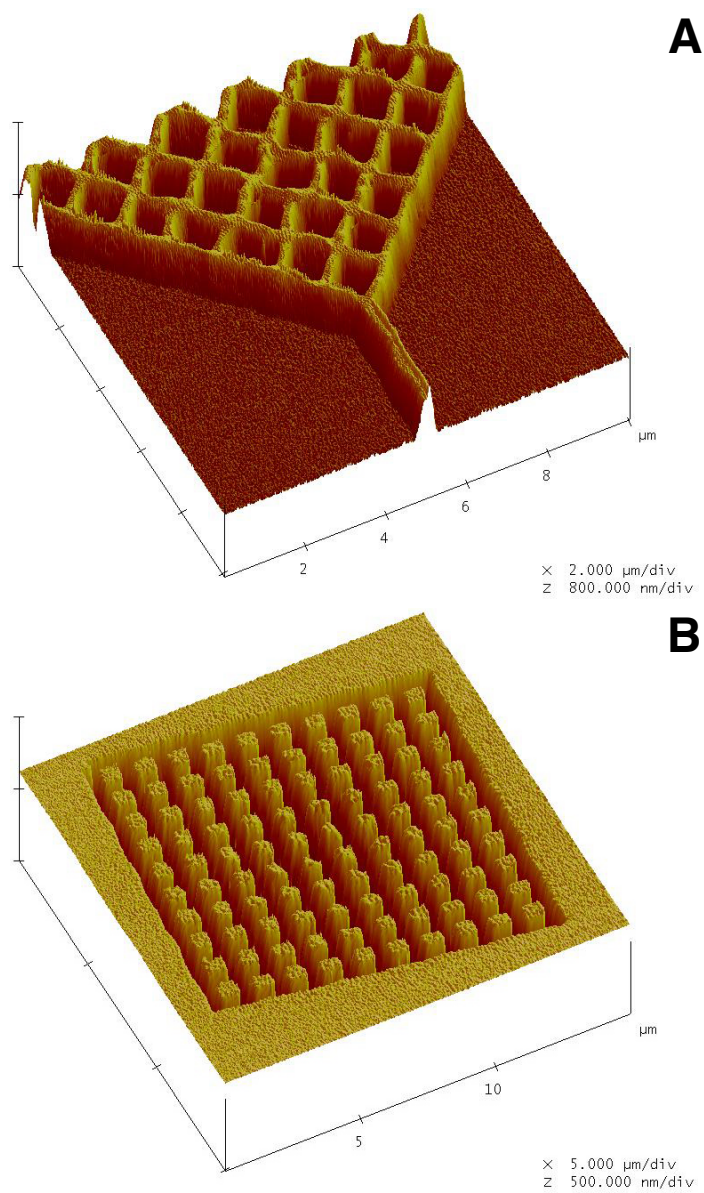


Figure 7.4: AFM images of **A** a master containing EBL-defined polystyrene lines forming an array of posts leading to the pore and **B** a PDMS slab into which an array of posts has been cast.

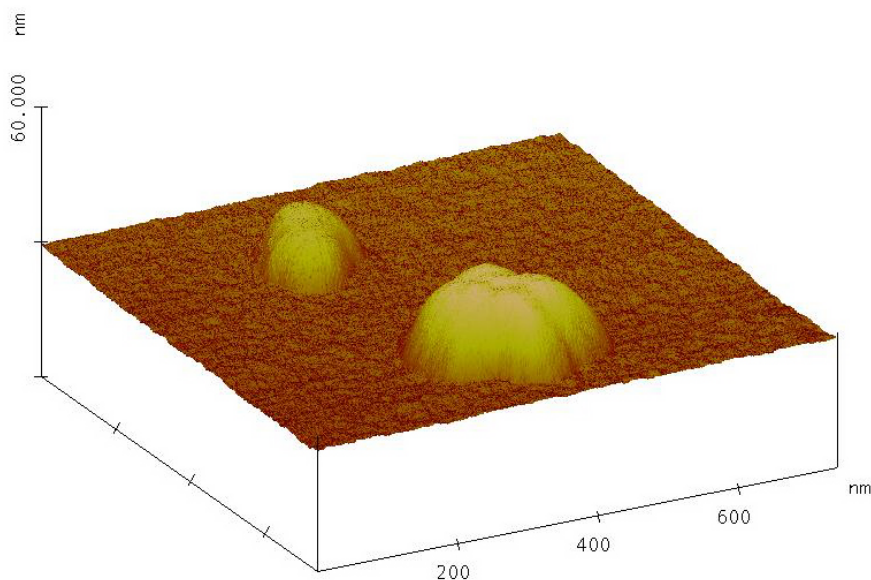


Figure 7.5: AFM image of compact lambda-phage DNA molecules condensed by mixing with 0.1 M Spermine⁴⁺. The solution was dried on a silicon substrate. No similar objects appeared in control measurements in which the solution lacked either the DNA or the Spermine.

other). The size of the compact toroid reflects that of the original DNA molecule, but does not have the conformational flexibility of the random coil that leads to the spread in peak sizes in our measurements (Fig. 7.3). Using atomic force microscopy, we confirmed the formation of compact structures of DNA in solutions containing various concentrations of either Spermine⁴⁺ or Spermidine³⁺, as shown in Fig. 7.5. However, our device's electrical measurements of lambda-phage DNA in the same solutions failed to show any peaks in the current trace when using either electrophoresis or fluid flow to drive particles through the pore. The reason for this failure is unclear; however, we hypothesize that the DNA molecules might have undergone a charge inversion[69] when collapsed, and that the resulting positively-charged collapsed objects stuck to the negatively charged glass and PDMS surfaces of the device.

7.5 Summary

The results described here represent a first step towards a host of single-molecule sensing applications. The measurements of DNA have been hampered by problems controlling the molecule's conformation, and with clogging of the pore by the DNA molecule itself³. However, by modestly decreasing the pore size, we will be sensitive to smaller molecules (such as proteins or viruses) that do not share the conformational flexibility of DNA, and thus should give more stable experimental results. The minimum achievable pore diameter for the type of PDMS used here is ~ 150 nm, but recent work has shown that other PDMS formulations can hold well-defined features down to 80 nm[43]. It is also possible to move to other materials; for example, pore diameters ≤ 50 nm are achievable when utilizing electron-beam lithography to define etched quartz or SiO₂ features. These materials might also help in alleviating the clogging problems seen with DNA.

Finally, this technique is currently only sensitive to geometrical attributes of the analyte; it would be of great interest to add chemical sensitivity to the measurement[16, 14, 15]. Chemically-specific detection can be added in two ways: first, by covalently attaching molecules of interest to the pore wall, we expect to see changes in the transit times of molecules in solution that interact with the immobilized molecules. Second, by employing ~ 200 nm pores, we can measure changes in the diameter of chemically-functionalized colloids or nanocrystals upon binding of molecules in the solution, as we have already done using micron-scale colloids and pores. The ease and reproducibility of micro-molding and the simplicity of our device greatly enhances the capabilities of artificial nanopores for molecular sensing.

³Through optical observation of fluorescently stained DNA molecules passing through a pore, we have found that single molecules will frequently become clogged in the pore. This occurs when the DNA strand penetrates and becomes tangled with the polymer matrix that constitutes the PDMS[44].

Conclusion and Future Directions

In this thesis, we have presented several important results in the field of resistive pulse sensing. We have demonstrated a novel platform for performing resistive pulse measurements. Our platform capitalizes on microfabrication techniques that allow us to construct devices rapidly and with great flexibility in design. We have demonstrated the construction of devices with pore sizes ranging from 150 nm to 1 μm , and containing other fluid handling elements. The devices are extremely compact, and consequently use sub-microliter amounts of fluid to perform each measurement.

We have used the device to measure single macromolecules of DNA, and to measure latex colloids with diameters between 100 nm and 600 nm. Using these results, we have achieved a complete understanding of the effects of spherical particles (of all sizes and radial positions) on the width (transit time) and height (electrical resistance change) of the measured pulses. We have then used this knowledge to implement an entirely new strategy for increasing the resolution of resistive pulse sensors by removing the effects of off-axis particles. This strategy allows us to resolve nanometer-scale changes in the diameter of particles, representing a precision of better than one part in five hundred. These off-axis effects are not specific to our device; thus all future applications of resistive pulse sensors should benefit from the strategy we have devised.

Finally, we have demonstrated that, through the application of the above results, our device can be used as a binding probe of unlabeled biological molecules. Precise

measurements of the diameter of protein-coated colloids show that they increase in size when they specifically bind to protein in the solution. We have shown that this technique can detect antibody concentrations as low as $0.5 \mu\text{g}/\text{mL}$, and with future improvements should be sensitive to concentrations of $1 \text{ ng}/\text{mL}$. Furthermore, our technique can be used to perform immunoassays in both inhibition and sandwich formats. These abilities, along with the other aforementioned advantages of our device (size, speed, small analyte consumption), should make our device an attractive candidate for future use as a biosensor in the laboratory or in the field.

Although we have accomplished a great deal in the experiments described in this thesis, there are several foreseeable extensions of the work. To that end, I wish to describe two of the more interesting future directions.

8.1 Multi-analyte Detection

Almost all biochemical binding assays (ELISA, surface plasmon resonance assays, etc.) are designed to measure only one analyte at a time. Assays that can simultaneously screen for the presence of multiple analytes are very useful since they save time and money, and do not require the possibly complex steps needed to separate different analytes from a single solution. A major future direction for our work is applying our binding assay (as described in Chapter 6) to multi-analyte detection. Our method has two major advantages in doing this: the ease of fabricating multiple pores on a single chip, and the use of colloids to add analyte specificity to the device.

All of the devices shown in this thesis consist of only a single pore. However, the microfabrication techniques we employ make it quite simple to create devices with multiple pores; the design of one such device is shown in Fig. 8.1. Different solutions would be pipetted into each of the outer reservoirs, thus permitting the screening of either several different solutions for the same analyte, or one solution for several different analytes. The measurement of current through each pore in this design is accomplished with a three point technique, and data from several pores can be

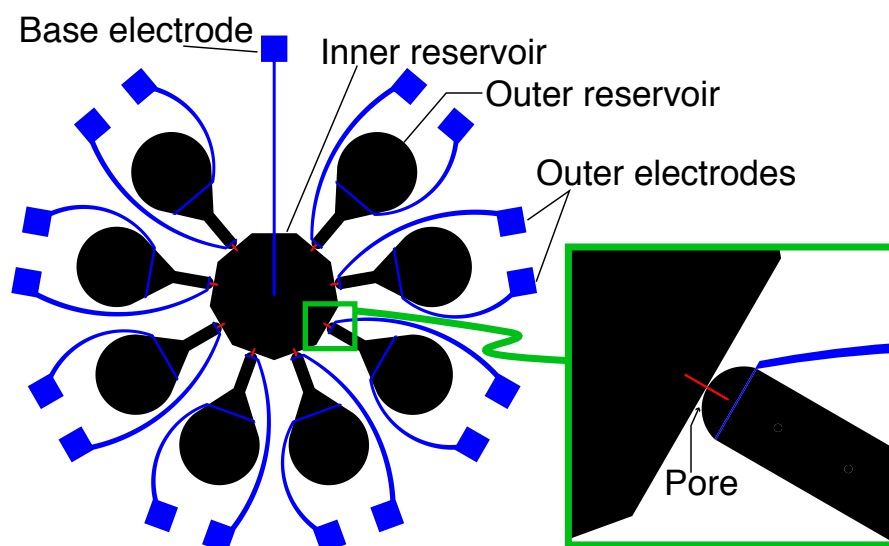


Figure 8.1: Schematic of a device containing eight pores. The black areas represent the eight outer reservoirs and the shared inner reservoir, the red lines represent the pores, and the blue areas represent the electrodes. In this design, different solutions can be added to each of the outer reservoirs for analysis while passing through the pores. The voltage across each pore is measured at constant current using a three point technique in which each all the current flows to ground through a common base electrode.

acquired simultaneously using a multichannel DAQ board in a computer.

A second strategy to add multi-analyte sensitivity is to utilize a single pore, but to mix the solution to be analyzed with different types of colloids. For example, imagine mixing an unknown solution with a colloid population of mean diameter 500 nm that binds to molecule **A**, and also with a second colloid population of mean diameter 530 nm that binds to molecule **B**. If molecule **A** is present in the solution, the 500 nm colloid increases in size to 510 nm; similarly, the presence of molecule **B** causes the 530 nm colloid to increase to 540 nm. By simultaneously mixing both types of colloids with the solution, then measuring the mixture with our resistive pulse sensor, we can determine the presence or absence of the molecules **A** and/or **B** by measuring the increased size of the two colloids.

Of great importance to this second strategy is the ability to determine which molecule is present through previous knowledge of the ‘bare’ diameter and chemical sensitivity of each colloid population. Essentially, the chemical sensitivity of each colloid population is ‘tagged’ by the bare colloid diameter, much as different colored fluorescent dyes can be used to tag antibodies that are sensitive to different analytes. A natural question to ask is this: how many different chemicals could be simultaneously screened when employing this method? In the above example, we are able to screen for two chemicals because the mean diameters of the two colloid populations were resolvable, both before and after either colloid binds to the analyte. Thus, the number of analytes that can be screened is determined by the minimum resolvable diameter difference of two populations, and the total range of colloid diameters that can be measured. Based on the data shown in Chapter 6, we estimate the minimum diameter difference to be 20 nm. We further estimate that, for a 1 μm diameter pore, the minimum usable colloid diameter is 400 nm and the maximum is 700 nm. While colloids smaller than 400 nm can be detected, the decrease in signal to noise for such small particles would probably render those measurements unusable. Furthermore, colloids larger than 700 nm have a substantial chance of clogging the pore. Thus, the total range is $700 - 400 = 300$ nm, and the total number of resolvable colloid

populations, and thus the total number of analytes that can be measured at once, is $300/20 = 15$.

Finally, we note that even larger number of analytes can be measured simultaneously by combining the two strategies (multiple pores and multiple colloid types). For example, a device containing 8 pores, with each pore able to distinguish 15 types of colloids, could sense $8 \times 15 = 120$ different analytes. Such a large number has only been achieved with micro-array devices.

8.2 A Time-dependent Binding Probe

As described so far, our binding probe is only capable of end-point analysis of biological reactions— that is, we can use it to discern the final state of a reaction (the fraction of bound and unbound molecules), but not the kinetic path the reaction followed to reach the final state. However, we believe that it is possible to add time-sensitivity to the probe, and thus extract kinetic information. To accomplish this, we will need to exploit the highly flexible nature of the microfabrication techniques we have used in order to add a fluid mixer onto the device.

In the experiments described in this thesis, the mixing of the colloids and the analytes was done off of the chip, and the mixed solution was then added to the device. The basic strategy for adding time-dependence is to add a mixer to the device, so that we can mix the two solutions on the chip, and then send the solution directly from the mixer to the pore for measurement. Time-sensitivity is achieved by varying the time between mixing and measurement (the incubation time); any changes with incubation time in the amount of ligand bound to the colloids could then be ascribed to the reaction kinetics. Variation of the incubation time could be achieved, for example, by utilizing several devices with different lengths of channel separating the mixer and pore, varying the flow rate through that same channel, or creating an incubation chamber where the mixed reactants are held with a valve for some period of time before being released to enter the pore.

An added advantage of performing mixing on the chip would be the decrease in the number of colloidal aggregates that could block the filter or pore. The decrease in aggregates would occur because of the nature of the aggregation process[9, 10, 11]: the binding time of antibody to the colloids is much faster than the crosslinking of colloids because the antibody diffuses much faster than the colloids. Thus, minimizing the incubation time will still allow the antibody to bind to the colloids, but not provide enough time for the colloids to diffuse into each other and form aggregates.

In order to perform accurate and useful measurements of the kinetics of a binding reaction, we must be able to control precisely the incubation time over a wide range. The design of the mixer is critical to the probe's ability to do this. Factors that must be considered include the homogeneity of the starting point of incubation (i.e. do all colloids, regardless of their position in the channel, become mixed at the same point?), and the differences in incubation time that occur if colloids travel at different speeds within the incubation channel due to the velocity profile of the fluid flow. Several microfabricated mixers have been proposed in the literature [71, 72, 73], each with varying degrees of complexity in fabrication and use. We note that the design of Knight et al. [73] is particularly simple, and thus would be relatively easy to add to our device.

8.3 Summary

In summary, I have described methods to extend the sensitivity of our device either to the time-dependence of binding reactions, or to multiple analytes. A device with these functions, along with those described throughout this thesis, would be a powerful new biochemical tool for the analysis of protein-protein interactions.

Recipes

In this Appendix, I list specific protocols and recipes for constructing the devices discussed in this thesis. All photolithography (PL) exposures refer to a mercury lamp illumination at 365 nm at a power of 10 mW/cm².

A.1 Solutions

The cleaning solutions are critical to lithography, sample preparation, and sample reuse. All three solutions listed are highly acidic or basic.

A.1.1 RCA SC1

The RCA SC1¹ procedure is effective for cleaning organic contaminants off of any silica surface (quartz, glass, silicon dioxide). I use it to clean substrates prior to both photolithography (PL) and electron-beam lithography (EBL), etched quartz devices, and electrode-carrying coverslips prior to sealing them with PDMS. When cleaning the latter two types of substrates, I use the dilute version of the solution to minimize the risk of the removal of any metal on the substrates or the etching of features on the device.

¹The name ‘RCA SC1’ stems from the company it was invented (the Recording Company of America); the second part stands for ‘Special Cleaning solution 1’. There is also an RCA SC2 procedure which is used to remove metal contaminants. Both procedures were invented for semiconductor processing.

Standard

1. Mix 5 parts deionized (DI) water with 1 part ammonium hydroxide and heat on a 200 °C hot plate while stirring.
2. Place substrates to be cleaned in a teflon holder in the solution.
3. When solution is nearly boiling, add 1 part hydrogen peroxide.
4. Let sit 5-10 minutes.
5. Remove substrates, rinse in DI water and blow dry.

Dilute

1. Mix 10 parts DI water with 1 part ammonium hydroxide and heat on a 150 °C hot plate while stirring.
2. Place substrates to be cleaned in a teflon holder in the solution.
3. When solution is warm, add 1 part hydrogen peroxide.
4. Let sit 5 minutes.
5. Remove substrates, rinse in DI water and blow dry.

A.1.2 Piranha Etch

The Piranha etch (named for its aggressiveness) is a very strong acidic solution that I use to remove significant amounts of organic scum when cleaning the etched quartz samples between uses, or to remove photoresist that hardened after a plasma etch. This cleaning solution can remove metal on substrates, but does not do so consistently. I will typically use this on a sample only after it has been cleaned using the RCA SC1 procedure, because the solution can become nearly explosive if excessive organics are present.

1. Mix 3 parts hydrogen peroxide with 7 parts sulfuric acid, and heat on a 80 °C hot plate.
2. Place substrates alone, or held in a clean teflon holder, into the solution.
3. Let sit 30 minutes.
4. Remove substrates and rinse with DI water. Take care to catch the rinsing water in a beaker, and dispose of it as an acidic solution.

A.1.3 Aqua Regia

Aqua Regia is solution able to dissolve noble metals, and I use it to remove damaged platinum electrodes from etched quartz devices prior to remaking new electrodes.

1. Mix 3 parts nitric acid with 1 part hydrochloric acid at room temperature.
2. Place substrates alone, or held in a clean teflon holder, into the solution.
3. Let sit until metal has dissolved.
4. Remove substrates and rinse with DI water.

A.2 Etched Quartz Devices

The etched quartz devices are fabricated in several stages: etching the pore, etching the reservoirs, depositing electrodes, and finally sealing the channels with a PDMS-coated coverslip. It is critical to clean the substrate well between the lithography stages, but also to be careful not to damage the device when doing so. Most notably, the RCA SC1 cleaning procedure will slowly etch silica surfaces, so it is only used in the dilute form so as not to change the diameter of the pore.

A.2.1 The Pore

Photolithography

1. Prepare the substrates by dicing a quartz wafer into ~ 2 cm square pieces, and then cleaning them with a standard RCA SC1 solution. Rinse the substrates in DI water, then isopropyl alcohol (IPA), then blow them dry.
2. Place a few drops of the primer hexamethyldisilazane (HMDS) on each substrate, and spin until dry.
3. Spin on the photoresist AZ5214E-IR at 4000 rpm for 30 s, creating a $1.4 \mu\text{m}$ thick layer.
4. Bake the substrate at 95°C for 45 s.
5. Using a mask with a solid $1 \mu\text{m}$ wide line, expose the substrate for 5 s. Be sure that the mask and substrate are in very close contact.
6. Bake the substrate at 115°C for 45 s.
7. Blanket expose the substrate for 2 m.
8. Develop for 2 minutes in the developer 422MIF; rinse in DI water and blow dry. At this point, resist should cover the entire substrate except for a $1 \mu\text{m}$ wide line where the substrate is bare.
9. Perform a 35 minute reactive ion etch (RIE) using CHF_3 ; this should etch a $\sim 1 \mu\text{m}$ depth into quartz. After the etch, perform a 10 minute oxygen plasma cleaning procedure to remove the excess photoresist.
10. Soak in acetone for 30 minutes, then sonicate (still in acetone) for 5 minutes. Rinse in IPA, blow dry, then view the substrate under a microscope. If there is still a residue of hardened photoresist at the edge of the etched line, the substrate must be cleaned with a Piranha etch.

11. The etched pore's dimensions can now be measured with an atomic force microscope (AFM), and the reservoirs can be added to the device.

Electron-beam Lithography

Using electron-beam lithography (EBL) to create the pores on etched quartz devices is a somewhat involved procedure that I have only used sparingly. Due to the complexity of performing EBL, I will not include the specific directions for exposing and developing the EBL resist.

1. Prepare the substrates by dicing a quartz wafer into 2 cm square pieces, then performing a standard RCA SC1 cleaning procedure, then rinsing the substrates in DI water and IPA, then blowing them dry.
2. Deposit 100 Å Ti using an electron-beam evaporator.
3. Spin on the EBL resist PMMA at 5000 rpm for 45 s.
4. Bake for 2 hours at 180 °C.
5. Perform the EBL exposure and development to create a ~ 100 nm wide developed line in the resist, along with some alignment marks. At this point, most of the sample is covered in PMMA and Ti, except for the 100 nm wide line (and the alignment marks) where it is only covered by Ti.
6. Perform a 8 minute plasma Ti etch using CF_4 . This procedure will result in removal of the 100 nm wide region of Ti (exposing the quartz underneath), and also some removal of the PMMA that covers the rest of the substrate.
7. Perform a 3 minute plasma quartz etch using CHF_3 ; this should etch ~ 50 nm into the 100 nm wide exposed quartz region.
8. Remove the remaining PMMA by soaking in acetone. Do not remove the excess Ti; it is needed to create optical contrast when aligning the reservoirs to the pore.

9. View the substrate with the AFM to measure the pore dimensions, and insure that all resist has been removed. If not, attempt to remove it by sonicating in acetone and/or using a Piranha etch. Once clean, the reservoirs can be added.

A.2.2 The Reservoirs

In this portion of the fabrication, photolithography is used to define the reservoirs and align them with the already-defined pore, then RIE is used to etch the reservoirs into the substrate.

1. Prepare the substrates by spinning on HMDS until dry. Note that the substrates should already be clean by the end of the procedure used to create the etched pores.
2. Spin on the photoresist SPR220-7 at 3500 rpm for 30 s, creating a 7 μm thick layer
3. Bake for 2 minutes at 115 $^{\circ}\text{C}$.
4. Align the mask containing the reservoir pattern to the pore. The larger photolithographically defined pores should be visible, while the EBL alignment marks are needed for the smaller pores. Expose for 4 minutes. In some cases, I have exposed for 7 minutes to create a slanted edge that is useful when making the electrodes.
5. Develop for 2 minutes in LDD-26W; agitate slightly during this time.
6. Etch the reservoirs ~ 3.5 μm into the quartz using a 3 hour CHF_3 RIE. The etch should be broken up into two 1.5 hour sessions separated by 0.5 hours so as not to overheat the substrate.
7. Remove the excess photoresist by soaking and sonicating in acetone. If residue remains, use an oxygen plasma clean and/or a Piranha etch. If using a EBL-defined pore, use a CF_4 plasma etch to remove the excess Ti. The substrate

now should contain the etched reservoirs and pores, and electrodes can now be added.

A.2.3 The Electrodes

The electrodes are added to the device by deposition of a patterned bilayer metal film. The difficulty in adding them occurs because they must lie in the reservoirs, and thus must continuously travel across the sharp corners and down the walls of the 3.5 μm deep etch. This problem is alleviated by either evaporating the metal at an angle, or by lessening the sharpness of the corners by slanting the walls of the etched channel (as described above).

1. Prepare the clean, etched substrates by spin-coating them with HMDS.
2. Spin on the photoresist 3318D at 4000 rpm for 30 s, creating a 1.8 μm thick layer.
3. Bake for 1 minute at 90 °C.
4. Expose for 4 minutes. This exposure, which is much longer than is normal for this photoresist, is needed to adequately expose the resist caught in the bottom corner of the etched reservoirs.
5. Develop for 2 minutes in 300 MIF, agitating slightly.
6. Using an electron beam evaporator, deposit 50 Å of Ti on the substrate with the substrate oriented 45° from the flux of metal. Deposit 50 Å more of Ti at a -45° orientation. Then twice deposit 250 Å of Pt, once at each orientation ($\pm 45^\circ$).
7. Lift off the excess metal and photoresist by soaking in acetone, then rinsing in IPA and blowing dry.

A.2.4 PDMS-coated Coverslips

Once the microfabrication steps have been completed, the open-topped channels must be covered. This is done by sealing a PDMS-coated glass coverslip over the device.

1. Clean #1 coverslips in a standard RCA SC1 solution, rinse them in DI water, then IPA, then blow dry.
2. Mix PDMS (Sylgard 184) at a standard 10:1 ratio, and degas it.
3. Place a coverslip on a spinner, and pour a small amount of PDMS on top of it. Allow the PDMS to spread out on the coverslip, either by using a second clean coverslip to spread it, or by spinning at a low speed.
4. Spin the coverslip at 6000 rpm for 1 minute.
5. Bake at least 24 hours at 80 °C; be sure that the coverslip is held horizontal during the bake to avoid an uneven final surface.
6. After curing, seal the coverslip PDMS side down onto a clean microscope slide.
7. Using a second slide as a straight edge, use a diamond scribe to mark and break off uneven portions of the PDMS coating (for example, there will typically be a thicker bead at the edge).
8. Pick up the remaining flat portion and rinse briefly in IPA to remove any shards from the cutting.
9. Oxidize the PDMS side in an air plasma for 10 s at 200 mT and 5 mA.
10. Place the now oxidized PDMS side onto the device, being sure to cover the pore and central electrodes. Tap the top of the cover slip to insure a complete, even seal. The device is now ready for wetting and measurement.

A.2.5 Reusing Devices

Etched quartz devices can be reused after each measurement. The exact procedure used to regenerate the device will depend on how degraded the device is.

1. After a measurement, soak the still-sealed device in Amtex CCR to begin to dissolve the PDMS coating. After a few hours of soaking, use a razor blade or tweezers to remove the coverslip from the etched quartz substrate. Replace the substrate into the Amtex CCR, and remove when all the PDMS has dissolved. Rinse the substrate in DI water.
2. Sonicate the substrate for 3 minutes in toluene to dissolve remnant latex colloids. Rinse in methanol, and blow dry.
3. Perform a dilute RCA SC1 clean to remove any remaining scum. Be careful to not leave the substrate in the solution for too long. Rinse in DI water and blow dry. At this point, if the sample is clean enough and the electrodes are not damaged, the substrate can be re-sealed with a fresh PDMS-coated coverslip, and re-measured.
4. If the sample is still dirty, clean with a Piranha etch. In some cases this will damage the electrodes. If not, then the sample is ready to be re-used.
5. If the electrodes are damaged, either in the measurement or during the Piranha etch, strip them completely off the substrate using Aqua Regia. Remake the electrodes as described above.

A.3 Embedded PDMS Devices

The main advantage in using embedded PDMS devices is in the speed of setting up devices for measurements. On average, constructing a master takes a similar or slightly less amount of time than etching the pore and reservoirs for an etched

quartz device. However, the master can be recast time and time again, while the etched quartz devices have typical lifetimes of 5-6 measurements, including remaking electrodes. Embedded PDMS devices consist of three parts: masters, the PDMS slabs cast from the masters, and the electrodes. A sealed device cannot be reused after a measurement.

A.3.1 The Master: Etched Pores

The raised line on the master that will be cast into PDMS as the embedded pore can be fabricated in two ways: by etching the substrate to create a raised SiO_2 line, or by using a very tough resist that itself acts as the raised line. This section describes the construction of the former, the next describes the construction of the latter. Both methods can be used to create either EBL or PL defined pores.

Electron-beam Lithography

1. Prepare substrates by dicing a SiO_2/Si wafer into squares 1.5 cm on a side. Clean the substrate with a standard RCA SC1 procedure.
2. Deposit 25 Å Ti on the substrates in an electron-beam evaporator. This layer is needed to create optical contrast for later alignment with the reservoir, although it also helps to keep charging effects from affecting the lithography.
3. Spin-coat each substrate with the negative EBL resist ma-N2403 at 4000 rpm for 30 s; this creates a 200 nm thick layer.
4. Perform the lithography and development to define a raised ~ 200 nm wide line in the resist, along with alignment marks. At this point, the substrate will mostly be covered with only Ti, except for the line and alignment marks, where it is covered in both Ti and the resist.
5. Perform a 3 minute plasma etch using CF_4 to remove the exposed Ti.

6. Perform a 10 minute plasma etch using CHF_3 to remove ~ 300 nm of SiO_2 .
7. Clean the remaining resist using a short 1 minute oxygen plasma clean and/or soaking in acetone. At this point, the substrate should hold a raised line and alignment marks, both consisting of SiO_2 , and both topped with a layer of Ti. The substrate is ready for the addition of the (negative) reservoirs.

Photolithography

The procedure for creating a raised, etched $1\ \mu\text{m}$ wide line using PL is exactly the same as that listed above (Section A.2.1) for creating a $1\ \mu\text{m}$ wide and deep channel for an etched quartz device, except a mask with with a clear $1\ \mu\text{m}$ wide line is used instead of one with a solid line.

A.3.2 The Master: Pores Made of Resist

Electron-beam Lithography

1. Prepare the polystyrene solution to be used as the negative EBL resist by dissolving polystyrene of molecular weight 100 kDa at 5% in toluene.
2. Prepare substrates by dicing a SiO_2/Si wafer into squares 2 cm on a side, and cleaning them in a standard RCA SC1 solution.
3. Deposit $30\ \text{\AA}$ Ti on each substrate in an electron-beam evaporator. As before, this is helpful both for creating optical contrast used in aligning the reservoirs, and for dissipating charge build-up during the exposure.
4. Spin-coat each substrate with the polystyrene solution at 1500 rpm for 60 s.
5. Bake for 30 minutes at $120\ ^\circ\text{C}$.
6. Perform the EBL exposure and development to create a raised line 200 nm wide, along with alignment marks, in the polystyrene.

7. Perform a 3 minute CF_4 plasma etch to remove the exposed Ti. At this point, the substrate consists mostly of bare SiO_2 , except for the patterned line and alignment marks, where the substrate is covered by a layer of Ti underneath a layer of polystyrene.

Photolithography

1. Prepare substrates by dicing a SiO_2/Si wafer into squares 2 cm on a side, and cleaning them in a standard RCA SC1 solution.
2. Place the substrates into a sputterer, and use an air plasma to clean the surface for 30 s at 50 mT and 5 mA. Then sputter $\sim 100 \text{ \AA}$ Au/Pd onto the substrates (30 mA, 50 mT, 60 s). This layer is needed to create optical contrast for later alignment with the reservoirs.
3. Spin-coat the substrates with the photoresist SU8-2002 at 3000 rpm for 30 s.
4. Bake each substrate for 1 minute at 65°C , immediately followed by a second bake for 2 minute at 95°C .
5. Expose the substrate for 2 s. Note that a longer exposure will result in a wider, thicker line.
6. Bake each substrate for 1 minute at 65°C , immediately followed by a second bake for 1 minute at 95°C .
7. Develop in SU-8 developer for 1 minute, then rinse briefly in fresh developer, then rinse in IPA and blow dry.
8. Hard bake the substrates for 15 minutes at 200°C to strengthen the adhesion of the resist to the substrate.
9. Dunk each substrate into TFA gold etchant solution for 10 s to remove the exposed Au/Pd layer, then rinse in DI water. At this point, the substrate will

mostly be bare SiO₂, except for the 1 μm wide region where it is covered by the Au/Pd underneath the hard-baked SU8-2002.

A.3.3 The Master: Reservoirs

10. Spin-coat the substrates (already clean and holding the raised line that will become the pore) in the photoresist SU8-2007 at 4000 rpm for 30 s, creating a 7 μm thick layer.
11. Bake each substrate at 65 °C for 1 minute, then immediately for 2 minutes at 95 °C.
12. Align the mask holding the reservoir pattern to the pore on each substrate, and expose the substrate for 5 s.
13. Bake each substrate at 65 °C for 1 minute, then immediately for 4 minutes at 95 °C.
14. Develop in SU-8 developer for 1 minute, then rinse briefly in fresh developer, then rinse in IPA and blow dry.
15. Hard bake the substrates for 15 minutes at 200 °C to remove any cracks in the resist and to strengthen the adhesion of the resist to the substrate. The masters are now complete and ready to be cast.

A.3.4 Casting the Master

1. Mix PDMS (Sylgard 184) at the recommended 10:1 ratio.
2. Rinse the masters in IPA, and blow dry.
3. Place a drop of HMDS on top of each master, then either blow it dry, or spin it dry.

4. Place each master into a 2 inch diameter plastic petri dish, and pour ~ 7 g of the mixed PDMS into each dish, creating a ~ 3 mm thick layer.
5. Place each dish into a vacuum chamber and degas the PDMS.
6. After degassing, insure that the masters have not lifted off the bottom of the dish. Then place each dish into a $80\text{ }^\circ\text{C}$ oven and bake for at least 24 hours.

A.3.5 The Electrodes

1. Clean #2 coverslips using a standard RCA SC1 procedure, rinse in IPA, and blow dry.
2. Treat each coverslip with HMDS and spin dry
3. Spin-coat each coverslip with the photoresist 3318D at 4000 rpm for 30 s, creating a $1.8\text{ }\mu\text{m}$ thick layer.
4. Bake each coverslip at $90\text{ }^\circ\text{C}$ for 1 minute.
5. Expose each coverlip for 30 s. This exposure, which is particularly long for this type of resist, creates an undercut in the resist after developing that makes lift-off much easier.
6. Develop in 300 MIF for 30 s, rinse in DI water, and blow dry.
7. In an electron-beam evaporator, deposit $50\text{ }\text{\AA}$ Ti followed by $250\text{ }\text{\AA}$ Pt on the coverslips.
8. Lift-off the excess metal and resist by soaking in acetone for 0.5 hours. Sonicate in acetone for 1 minute, the rinse in IPA and blow dry.

A.3.6 Glass-PDMS bonding

The final step in preparing the embedded PDMS devices is to bond the PDMS slab (containing the pore and reservoirs) to the electrode-carrying coverslip. This is done in a permanent manner using the following method to insure that no leaks will occur even at fairly high pressures, and that the pore/electrode alignment cannot be shifted.

1. Clean the electrode-carrying coverslips in a dilute RCA SC1 procedure.
2. Cut a PDMS slab containing the pore and reservoirs from each master. Remove excess PDMS from the dish holding the master, and set aside for later recasting.
3. Seal the slab, feature side down, to a clean microscope slide. Using a sharp flat-ended needle, core holes into the slab that connect to the reservoirs. These holes are used later to add solution, and to seal to the tubing that connects to the fluid pump.
4. Rinse the feature side of the PDMS slab sequentially in acetone, IPA, methanol and DI water, and blow dry.
5. Place the PDMS slab and coverslip, both feature side up, onto a clean microscope slide. Insure that a small amount of water exists between the coverslip and slide so that the coverslip is held in place. Place the slide into a sputterer, and oxidize both objects in an air plasma at 200 mT and 5 mA for 10 s.
6. Place a 10 μL drop of 2:1 Methanol:DI water solution onto the coverslip. Place the PDMS slab, feature side down, onto this drop, and tap the slab to insure that it can freely slide on the coverslip, and to remove bubbles.
7. View the PDMS/coverslip assembly under a microscope, and align the pore and reservoirs to the electrodes. If, before alignment is achieved, the slab stops freely sliding due to evaporation of the methanol/water solution, add a further small amount of that solution to the assembly.

8. Once aligned, let the assembly sit untouched for 4 minutes so that the slab will not slide and become unaligned.
9. Place the assembly onto a hot plate at 60 °C for 5 minutes. This serves to drive off all the remaining solution.
10. Ramp the hot plate to 150 °C over 10 minutes. This serves to strengthen the bond between the PDMS and the coverslip. The ramped bake cannot be started immediately after alignment because, once the bake becomes hot enough, any remaining solution can boil and knock the slab off of the coverslip. After this bake, the device is complete, and ready to be wet with solution and measured.

Bibliography

- [1] W. H. Coulter, U. S. Patent No. 2656508: Means for counting particles suspended in fluid, 1953.
- [2] H. E. Kubitschek, *Nature* **182**, 234 (1958).
- [3] E. C. Gregg and K. D. Steidley, *Biophysical Journal* **5**, 393 (1965).
- [4] R. W. Deblois and C. P. Bean, *Review of Scientific Instruments* **41**, 909 (1970).
- [5] R. W. Deblois, *Biophysical Journal* **21**, A149 (1978).
- [6] R. W. Deblois, C. P. Bean, and R. K. A. Wesley, *Journal of Colloid and Interface Science* **61**, 323 (1977).
- [7] R. W. Deblois, E. E. Uzgiris, D. H. Cluxton, and H. M. Mazzone, *Analytical Biochemistry* **90**, 273 (1978).
- [8] B. I. Feuer *et al.*, *Virology* **90**, 156 (1978).
- [9] G. K. von Schulthess, R. W. Deblois, and G. B. Benedek, *Biophysical Journal* **21**, A115 (1978).
- [10] G. K. von Schulthess, G. B. Benedek, and R. W. Deblois, *Macromolecules* **13**, 939 (1980).
- [11] G. K. von Schulthess, G. B. Benedek, and R. W. Deblois, *Macromolecules* **16**, 434 (1983).

- [12] S. M. Bezrukov, I. Vodyanoy, and V. A. Parsegian, *Nature* **370**, 279 (1994).
- [13] S. M. Bezrukov, *Journal of Membrane Biology* **174**, 1 (2000).
- [14] H. Bayley and C. R. Martin, *Chem Rev* **100**, 2575 (2000).
- [15] H. Bayley and P. S. Cremer, *Nature* **413**, 226 (2001).
- [16] O. Braha *et al.*, *Chem Biol* **4**, 497 (1997).
- [17] M. Akeson *et al.*, *Biophysical Journal* **77**, 3227 (1999).
- [18] J. J. Kasianowicz, E. Brandin, D. Branton, and D. W. Deamer, *Proceedings of the National Academy of Sciences of the United States of America* **93**, 13770 (1996).
- [19] L. Sun and R. M. Crooks, *Langmuir* **15**, 738 (1999).
- [20] S. B. Lee *et al.*, *Science* **296**, 2198 (2002).
- [21] L. Sun and R. M. Crooks, *Journal of the American Chemical Society* **122**, 12340 (2000).
- [22] J. Li *et al.*, *Nature* **412**, 166 (2001).
- [23] J. C. Maxwell, *A Treatise on Electricity and Magnetism*, 3rd ed. (Clarendon, Oxford, 1904), Vol. 1.
- [24] L. Rayleigh, *Phil. Mag.* **34**, 481 (1892).
- [25] J. L. Anderson and J. A. Quinn, *Review of Scientific Instruments* **42**, 1257 (1971).
- [26] W. R. Smythe, *Physics of Fluids* **4**, 756 (1961).
- [27] W. R. Smythe, *Physics of Fluids* **7**, 633 (1964).
- [28] W. R. Smythe, *Review of Scientific Instruments* **43**, 817 (1972).

- [29] L. I. Berge, T. Jossang, and J. Feder, *Measurement Science and Technology* **1**, 471 (1990).
- [30] D. J. Tritton, *Physical Fluid Dynamics* (Clarendon Press, Oxford, 1988).
- [31] T. Bohlin, *Trans. Roy. Inst. Technol. (Stockholm)* (1960).
- [32] J. Happel and H. Brenner, *Low Reynolds Number Hydrodynamics with Special Applications to Particulate Media* (Prentice-Hall, Englewood Cliffs, New Jersey, 1965).
- [33] P. L. Paine and P. Scherr, *Biophysical Journal* **15**, 1087 (1975).
- [34] J. J. L. Higdon and G. P. Muldowney, *J. Fluid Mech.* **298**, 193 (1995).
- [35] L. I. Berge, *Journal of Colloid and Interface Science* **135**, 283 (1990).
- [36] H. L. Goldsmith and S. G. Mason, *Journal of Colloid Science* **17**, 448 (1962).
- [37] D. W. Fakes, M. C. Davies, A. Brown, and J. M. Newton, *Surface and Interface Analysis* **13**, 233 (1988).
- [38] M. K. Chaudhury and G. M. Whitesides, *Langmuir* **7**, 1013 (1991).
- [39] E. Delamarche *et al.*, *Advanced Materials* **13**, 1164 (2001).
- [40] N. Bowden, W. T. S. Huck, K. E. Paul, and G. M. Whitesides, *Applied Physics Letters* **75**, 2557 (1999).
- [41] S. Bengtsson, *Journal of Electronic Materials* **21**, 841 (1992).
- [42] Y. N. Xia and G. M. Whitesides, *Angewandte Chemie-International Edition* **37**, 551 (1998).
- [43] H. Schmid and B. Michel, *Macromolecules* **33**, 3042 (2000).
- [44] G. Facer, Personal communication, 2001.

- [45] P. Horowitz and W. Hill, *The Art of Electronics*, 2nd ed. (Cambridge University Press, Cambridge, 1989).
- [46] P. B. Lippa, L. J. Sokoll, and D. W. Chan, *Clin Chim Acta* **314**, 1 (2001).
- [47] T. Vo-Dinh and B. Cullum, *Fresenius J Anal Chem* **366**, 540 (2000).
- [48] A. P. Turner, *Science* **290**, 1315 (2000).
- [49] R. I. Stefan, J. F. van Staden, and H. Y. Aboul-Enein, *Fresenius J Anal Chem* **366**, 659 (2000).
- [50] T. T. Ngo, *Methods* **22**, 1 (2000).
- [51] Y. K. Sykulev, D. A. Sherman, R. J. Cohen, and H. N. Eisen, *Proc Natl Acad Sci U S A* **89**, 4703 (1992).
- [52] W. M. Mullett, E. P. Lai, and J. M. Yeung, *Methods* **22**, 77 (2000).
- [53] M. M. Bradford, *Anal Biochem* **72**, 248 (1976).
- [54] J. Bruchez, M. *et al.*, *Science* **281**, 2013 (1998).
- [55] O. A. Saleh, L. Dunkelberger, and L. L. Sohn, In preparation (2002).
- [56] S. M. Bezrukov and J. J. Kasianowicz, *Physical Review Letters* **70**, 2352 (1993).
- [57] T. K. Rostovtseva and S. M. Bezrukov, *Biophysical Journal* **74**, 2365 (1998).
- [58] L. Q. Gu, S. Cheley, and H. Bayley, *Science* **291**, 636 (2001).
- [59] Y. Kobayashi and C. R. Martin, *Journal of Electroanalytical Chemistry* **431**, 29 (1997).
- [60] T. A. J. Duke, R. H. Austin, E. C. Cox, and S. S. Chan, *Electrophoresis* **17**, 1075 (1996).

- [61] J. Han and H. G. Craighead, *Science* **288**, 1026 (2000).
- [62] O. Bakajin *et al.*, *Analytical Chemistry* **73**, 6053 (2001).
- [63] J. Y. Han and H. G. Craighead, *Analytical Chemistry* **74**, 394 (2002).
- [64] V. A. Bloomfield, *Biopolymers* **31**, 1471 (1991).
- [65] V. A. Bloomfield, *Curr Opin Struct Biol* **6**, 334 (1996).
- [66] N. A. Kasyanenko *et al.*, *Macromolecular Symposia* **136**, 25 (1998).
- [67] R. Golestanian, M. Kardar, and T. B. Liverpool, *Physical Review Letters* **82**, 4456 (1999).
- [68] N. A. Kasyanenko, A. V. Zanina, O. V. Nazarova, and E. F. Panarin, *Langmuir* **15**, 7912 (1999).
- [69] T. T. Nguyen, I. Rouzina, and B. I. Shklovskii, *Journal of Chemical Physics* **112**, 2562 (2000).
- [70] A. Y. Grosberg, T. T. Nguyen, and B. I. Shklovskii, *Reviews of Modern Physics* **74**, 329 (2002).
- [71] A. D. Stroock *et al.*, *Science* **295**, 647 (2002).
- [72] R. H. Liu *et al.*, *Journal of Microelectromechanical Systems* **9**, 190 (2000).
- [73] J. B. Knight, A. Vishwanath, J. P. Brody, and R. H. Austin, *Physical Review Letters* **80**, 3863 (1998).